

A MICROBOLOMETER DETECTOR
BASED ON A SOL-GEL TECHNOLOGY

A THESIS SUBMITTED TO
THE GRADUATE SCHOOL OF NATURAL AND APPLIED SCIENCES
OF
MIDDLE EAST TECHNICAL UNIVERSITY

BY

ÖZGECAN DERVİŞOĞLU

IN PARTIAL FULFILLMENT OF THE REQUIREMENT
FOR
THE DEGREE OF DOCTOR OF PHILOSOPHY
IN
MICRO AND NANOTECHNOLOGY

SEPTEMBER 2013

Approval of the thesis:

A MICROBOLOMETER DETECTOR BASED ON A SOL-GEL TECHNOLOGY

submitted by **ÖZGECAN DERVİŞOĞLU** in partial fulfillment of the requirements for the degree of **Doctor of Philosophy in Micro and Nanotechnology Graduate Program, Middle East Technical University** by,

Prof. Dr. Canan Özgen
Dean, Graduate School of **Natural and Applied Sciences**

Prof. Dr. Tayfun Akın
Head of Department, **Micro and Nanotechnology**

Prof. Dr. Tayfun Akın
Supervisor, **Electrical and Electronics Engineering Dept., METU**

Assoc. Prof. Dr. Caner Durucan,
Co-Supervisor, **Metallurgical and Materials Eng. Dept., METU**

Examining Committee Members:

Prof. Dr. Macit Özenbaş
Metallurgical and Materials Engineering Department, METU

Prof. Dr. Tayfun Akın
Electrical and Electronics Engineering Department, METU

Prof. Dr. Ömer Dağ
Chemistry Department, Bilkent University

Prof. Dr. Cengiz Beşikçi
Electrical and Electronics Engineering Department, METU

Assoc. Prof. Dr. Haluk Külâh
Electrical and Electronics Engineering Department, METU

Date: 03.09.2013

I hereby declare that all information in this document has been obtained and presented in accordance with academic rules and ethical conduct. I also declare that, as required by these rules and conduct, I have fully cited and referenced all material and results that are not original to this work.

Name, Last name : Özgecan Dervişođlu

Signature :

ABSTRACT

A MICROBOLOMETER DETECTOR BASED ON A SOL-GEL TECHNOLOGY

Dervişoğlu, Özgecan

Ph.D., Micro and Nanotechnology Graduate Program

Supervisor : Prof. Dr. Tayfun Akın

Co-Supervisor : Assoc. Prof. Dr. Caner Durucan

September 2013, 113 pages

The objective of this study is to develop a high performance bolometric material for microbolometers. The bolometric material to be developed was chosen as vanadium oxide due to its high temperature coefficient of resistance (TCR), low 1/f noise performance, and read out integrated circuit (ROIC) compatible resistivity. Among various deposition techniques, sol-gel method was decided to be implemented because of its various advantages such as simpler instrumentation, attainability of good chemical homogeneity, high deposition rate, etc. The route of dissolving metallic vanadium powder in hydrogen peroxide was determined as the sol-gel route to be followed.

Having conducted various experimental runs, the sol formation and VO_x thin film deposition steps were optimized and successful coatings on Si/SiN_x substrates could be obtained. The sheet resistance, thickness, resistivity, morphology, and phase of VO_x thin films heat treated at different temperatures upto 400°C were characterized and then, successful microresistor structures could be fabricated by utilizing vanadium pentoxide gel (V₂O₅.nH₂O with n≤1.8) among the VO_x phases as the bolometric material due its low enough resistivity (i.e. below 20 Ω.cm). This is the first time in literature that V₂O₅.nH₂O phase was used as an IR active material for microbolometers. The resistance values could be maintained below 100 kΩ for microresistors that can be fit into a 35 μm pixel pitch. The TCR of V₂O₅.nH₂O thin films was measured to be ranging between -1.7 and -2.4 %/°C. The lowest 1/f noise parameter ($C_{1/f}$) that could be achieved is 1.6×10^{-11} .

After microresistor fabrication, suspended single pixels having 35 μm pitch were fabricated successfully by implementing the developed sol-gel deposited V₂O₅.nH₂O thin film as the bolometric material. The responsivity, thermal conductance, thermal time constant, and absorptance of a single pixel were measured to be 50,569 V/W, 3.37×10^{-8} W/K, 20.9 ms, and 87 %, respectively. These performance values encourage to implement the sol-gel deposited V₂O₅.nH₂O thin film into the large format microbolometer arrays, thus, a 384x288

microbolometer array on a ROIC in which the developed sol-gel deposited $V_2O_5 \cdot nH_2O$ was used as the IR active material was fabricated successfully.

Key words: microbolometer, bolometric material, vanadium oxide, sol-gel deposition.

ÖZ

SOL-JEL TEKNOLOJİSİNE DAYALI MİKROBOLOMETRE DEDEKTÖRÜ

Dervişoğlu, Özgecan

Doktora, Mikro ve Nanoteknoloji Lisansüstü Programı

Tez Danışmanı : Prof. Dr. Tayfun Akın

Ortak Tez Danışmanı : Doç. Dr. Caner Durucan

Eylül 2013, 113 sayfa

Bu çalışmanın amacı mikrobolometre için yüksek performanslı bolometrik malzeme geliştirilmesidir. Vanadyum oksit, yüksek direncin sıcaklıkla değişim katsayısına (TCR), düşük 1/f gürültü performansına ve tümleşik okuma devresi (ROIC) ile uyumlu öz dirence sahip olması sebebiyle geliştirilmesi planlanan bolometrik malzeme olarak seçilmiştir. Çeşitli üretim teknikleri arasından sol-jel yöntemi, kullanılan ekipmanın basitliği, yüksek biriktirme hızı, iyi kimyasal homojenlik elde edilebiliyor olması gibi yararlarından dolayı kullanılacak yöntem olarak seçilmiştir. Vanadyum metal tozunu hidrojen peroksit içerisinde çözdürme işlemi, takip edilecek sol-jel yöntemidir.

Çeşitli deneylerden sonra, sol oluşturma ve VO_x ince film kaplama basamakları optimize edilmiş ve Si/SiN_x tabanları üzerine başarılı kaplamalar elde edilmiştir. VO_x ince filmlerin yüzey direnci, kalınlığı, öz direnci, morfolojisi ve fazı, karakterize edildikten sonra, düşük öz direnci olması nedeniyle vanadyum pentoksit jel ($V_2O_5.nH_2O$, $n \leq 1,8$) fazı kullanarak mikrodirenç yapıları başarıyla üretilmiştir. Bu çalışma $V_2O_5.nH_2O$ fazının mikrobolometrede IR aktif malzemesi olarak kullanılması bakımından literatürde bir ilktir. Direnç değerleri, 35 μm 'lik piksele sığabilecek boyuttaki mikrodirençler için 100 k Ω 'un altında olacak şekilde elde edilebilmiştir. $V_2O_5.nH_2O$ ince filmlerin ölçülen TCR değerleri -1,7 ile -2,4 %/°C arasında değişmektedir. Elde edilen en düşük 1/f gürültü parametre ($C_{1/f}$) değeri $1,6 \times 10^{-11}$ 'dir.

Mikrodirenç üretiminden sonra, geliştirilen sol-jel yöntemiyle biriktirilmiş VO_x ince filmi, bolometrik malzeme olarak kullanarak 35 μm askıda tekli pikseller üretilmiştir. Tekli pikselin tepkiselliği, ısıl iletkenliği, ısıl zaman sabiti ve emilimi, sırasıyla 50.569 V/W, $3,37 \times 10^{-8}$ W/K, 20,9 ms ve % 87 olarak ölçülmüştür. Bu performans değerleri, sol-jel yöntemiyle biriktirilen $V_2O_5.nH_2O$ ince filmin, okuma devresi üzerine üretilen mikrobolometre matrislerindeki kullanımını teşvik etmektedir. Dolayısıyla, okuma devresi

üzerine, $V_2O_5 \cdot nH_2O$ ince filmin IR aktif malzeme olarak kullanıldığı 384x288 formatında mikrobolometre matrisi başarıyla üretilmiştir.

Anahtar kelimeler: mikrobolometre, bolometrik malzeme, vanadyum oksit, sol-jel yöntemi.

*To
my dearest family*

ACKNOWLEDGEMENTS

First and foremost, I would like to express my deepest appreciation and thanks to my thesis advisor Prof. Dr. Tayfun Akin for his supervision, invaluable guidance, and providing me exceptional research opportunities as well as enthusiasm throughout my thesis study. It was a great chance and experience for me to meet and work with him.

I am also grateful to my co-advisor Assoc. Prof. Dr. Caner Durucan who provided me the opportunity to work in his laboratory, encouraging advice and optimism concerning this work.

I would like to thank Prof. Dr. Macit Özenbaş and Prof. Dr. Ömer Dağ for their valuable comments and suggestions during the progress of my thesis.

I am truly thankful to Dr. Yusuf Tanrikulu at first for sharing his immense knowledge as well as comments with me, and then, for his help whenever I needed. I am grateful to Orhan Akar for his invaluable advice and guidance in the cleanroom.

I wish to thank Başak Kebapçı for her sincere friendship, positive attitude and her always being ready for help. I would like to thank Selçuk Keskin for his great support, valuable friendship, and witty conversations. I am indebted Numan Eroğlu for his friendship, sharing his experience and knowledge regarding his own study. I would like to thank Eren Çanga for his guidance and help during my cleanroom processes. My special thanks go to Şeniz Esra Küçük for her friendship and helping me in various stages of my thesis study. I am grateful to Ozan Ertürk for his invaluable friendship and endless efforts for my thesis study.

I am particularly grateful to Burak Eminoğlu who helped me greatly for noise measurements. It would not have been possible to perform the tests without his endless efforts.

I would like to extend my thanks to Mert Torunbalcı for his invaluable fellowship, encouragement and endless support when necessary. I wish also thank to Serdar Tez and Akin Aydemir for their friendship and motivative talks regarding my thesis study.

I would like to express my special thanks to Gülçin Çiçek for her priceless fellowship. It was a great pleasure to have such a friend on the occasion of this thesis study. I am also grateful to my friends Betül Akköprü, Hakan Yavaş, Tümerkan Kesim, Onur Rauf Bingöl, Özlem Yıldırım, and other friends from METU METE Materials Chemistry Laboratory who made the environment gladsome and peaceful during my study there.

I owe my gratitude to all former and current members of METU MEMS and METU BIO-MEMS group members whose names are not listed here, for creating a very pleasant and friendly working environment. I am also very thankful to the staff of METU MEMS

Research and Applications Center for creating the best working atmosphere and their friendship.

Last but not the least, I am deeply grateful to my parents, my brother, and family for their endless love, encouragement, support, and sacrifices during this thesis study and my entire life.

TABLE OF CONTENTS

ABSTRACT.....	v
ÖZ	vii
ACKNOWLEDGEMENTS	xi
TABLE OF CONTENTS.....	xiii
LIST OF TABLES	xv
LIST OF FIGURES	xvii
CHAPTERS	1
1. INTRODUCTION	1
1.1. Infrared Radiation	2
1.2. Infrared Detectors	5
1.3. Microbolometers	6
1.4. Figures of Merit for Microbolometers	10
1.4.1. Temperature Coefficient of Resistance (TCR)	10
1.4.2. Thermal Conductance (G_{th}).....	11
1.4.3. Thermal Time Constant (τ)	11
1.4.4. Responsivity (R_V or R_I)	12
1.4.5. Noise Equivalent Power (NEP).....	13
1.4.6. Noise Equivalent Temperature Difference (NETD)	15
1.4.7. Detectivity (D^*)	15
1.5. Infrared Radiation Sensitive Bolometric Materials.....	15
1.6. Vanadium Oxide System	21
1.7. Sol-Gel Deposition of Vanadium Oxide.....	25
1.8. Research Objectives and Thesis Organization.....	27
2. OPTIMIZATION OF SOL PREPARATION, THIN FILM DEPOSITION AND MATERIAL CHARACTERIZATION.....	29
2.1. The Optimization of Sol Preparation and Its Characterization	29
2.2. The Deposition of VO_x Thin Films	35
2.3. The Characterization of VO_x Thin Films	37
2.4. Conclusions.....	42
3. MICRORESISTOR FABRICATION AND PERFORMANCE TEST RESULTS	45
3.1. The Description of TCR and Noise Measurements	45
3.2. The Fabrication of Microresistors and Their Performance Test Results	49
3.2.1. The VO_x Lift-Off Process Trials	64
3.2.2. The Optimization of VO_x RIE.....	68
3.3. Conclusions.....	71
4. SUSPENDED SINGLE PIXEL FABRICATION AND PERFORMANCE TEST RESULTS	73
4.1. The Description of Thermal Conductance, Responsivity, and IR Absorptance Measurements	73
4.2. The Fabrication of Suspended Single Pixels and Performance Test Results	75

4.3. Conclusions.....	84
5. FABRICATION OF 384x288 MICROBOLOMETER FOCAL PLANE ARRAY AND PERFORMANCE MEASUREMENTS	85
5.1. The Fabrication of Test Resistors of 384x288 Microbolometer Array	85
5.2. The Fabrication of 384x288 Microbolometer Array on a 6” ROIC Wafer.....	89
5.4. Conclusions.....	99
6. CONCLUSIONS AND FUTURE WORK	101
REFERENCES	103
APPENDICES	109
A. DETAILS OF SUSPENDED SINGLE PIXEL FABRICATION STEPS	109
B. DETAILS OF 384x288 MICROBOLOMETER ARRAY FABRICATION STEPS .	111
CURRICULUM VITAE.....	113

LIST OF TABLES

TABLES

Table 1.1. The commercial and state-of-the-art R&D microbolometer arrays [11,17].	9
Table 1.2. Comparison of bolometric materials in terms of process temperature, resistivity, TCR and 1/f noise performance.	19
Table 1.3. MIT temperatures of vanadium oxide phases [53,54].	21
Table 1.4. The effect of doping ions on the transition temperature [57].	23
Table 2.1. The summary of experimental runs of different dissolution processes.	31
Table 2.2. The sheet resistance of VO _x thin films spin coated at different rpm's and annealed at different temperatures.	37
Table 2.3. The thickness measurement results of VO _x thin films spin coated at 2000 rpm and calculated resistivity values.	40
Table 3.1. The sol-gel VO _x deposition details of second microresistor fabrication run.	51
Table 3.2. The noise measurement results of metal and different VO _x resistor pairs under different bias current.	54
Table 3.3. The noise measurement results of metal and VO _x resistor pairs after an improvement in the noise measurement set-up was made.	56
Table 3.4. The sol-gel VO _x deposition details of third microresistor fabrication run.	57
Table 3.5. The process parameters used as the starting point for VO _x dry etching with a gas mixture CF ₄ and O ₂ .	58
Table 3.6. The measured resistance values of VO _x resistors whose VO _x layer was deposited thicker and dry etched by using CF ₄ in the RIE equipment.	59
Table 3.7. The sol-gel VO _x deposition details of fourth microresistor fabrication run which was on a 4" glass wafer.	61
Table 3.8. The noise measurement results of metal and VO _x resistor pairs. The VO _x resistors were fabricated on a glass wafer and the VO _x layer was etched with CF ₄ in the RIE equipment. The biasing current was 20 μA in all of the measurements.	62
Table 3.9. The comparison of C _{1/f} values of different bolometric materials reported in literature with this work.	64

Table 3.10. The progress in terms of resistance, TCR, and noise performance upto this point in this thesis study.....	64
Table 3.11. The sol-gel VO _x deposition details of first microresistor fabrication by VO _x lift-off.....	65
Table 3.12. The noise test results of VO _x resistors processed by lift-off and annealed at different temperatures.	68
Table 3.13. The silicon nitride etching rate (nm/min) according to the power and flow rate of CF ₄ with 4% O ₂ [73]......	68
Table 3.14. The noise measurement results of metal and VO _x resistor pairs. The VO _x layer was etched by RIE with 20-W power. The biasing current was 20 μA in all of them.....	70
Table 3.15. The noise measurement results of both metal and VO _x resistor pairs. The VO _x resistors were fabricated on a 6” Si/SiN _x wafer and its VO _x layer was etched by RIE with 20-W power. The biasing current was 20 μA in all of them.....	71
Table 4.1. The sol-gel VO _x deposition details of suspended single pixel fabrication.....	79
Table 4.2. The noise measurement results of metal and VO _x resistor pairs. The VO _x resistors are the test resistors of 35 μm pitch pixels.....	84

LIST OF FIGURES

FIGURES

Figure 1.1. The infrared spectrum with its sub-regions in the entire spectrum [3].	3
Figure 1.2. The IR light transmission of atmosphere and absorbing molecules [4].	3
Figure 1.3. Spectral radiance with respect to wavelength at different temperatures [5].	4
Figure 1.4. The classification of infrared detectors.	5
Figure 1.5. A simplified view of a microbolometer [6].	6
Figure 1.6. The SEM image of diode type microbolometer pixels fabricated at METU [6].	7
Figure 1.7. (a) The SEM image of 640x480 array fabricated by Mitsubishi and (b) the image taken with this array [9].	7
Figure 1.8. The SEM images of state of the art microbolometers fabricated by (a) Raytheon [12], (b) NEC [13], (c) BAE [2].	8
Figure 1.9. The SEM images of multilevel detectors fabricated by (a) NEC [14], (b) DRS [15], (c) Raytheon [16].	9
Figure 1.10. An image obtained by 35 μm pixel 384x288 microbolometer FPA fabricated at METU MEMS Center [18].	10
Figure 1.11. The representation of a microbolometer thermal circuit analogous to an electrical circuit.	12
Figure 1.12. The NETD performance of VO_x microbolometer fabricated by BAE Systems [2].	16
Figure 1.13. (a) The top view of a planar type resistor, (b) the cross sectional view of a sandwich type resistor.	17
Figure 1.14. Oxide phases of vanadium [53].	21
Figure 1.15. The MIT curves of VO_2 thin film [54].	22
Figure 1.16. The resistivity change of single crystal and polycrystalline VO_2 thin film during transition [57].	23
Figure 1.17. The structure of (a) $\text{V}_2\text{O}_5 \cdot n\text{H}_2\text{O}$ ($n=1$) [60], (b) V_2O_5 consisting of VO_5 square pyramid layers [61].	24
Figure 1.18. The process steps of sol-gel technique [63].	25

Figure 1.19. Representation of sol-gel coating techniques [57].....	26
Figure 2.1. The assembled experimental set-up and process steps of sol-gel route for preparing the coating liquid of VO _x thin film deposition.	30
Figure 2.2. The photograph of (a) solid material obtained by drying the sol formed in Run 4 in Table 2.1 in a high density polyethylene container at 80°C for 22 hours and (b) its powdered form in an agate mortar.	32
Figure 2.3. The XRD pattern of powder obtained after drying the sol formed in Run 4 in Table 2.1.	32
Figure 2.4. The DTA/TGA curve of powder sample in air atmosphere at a heating rate of 5°C/min.	33
Figure 2.5. The DTA/TGA curve of powder sample in N ₂ atmosphere at a heating rate of 5°C/min.	34
Figure 2.6. The EDX result of hydrated vanadium pentoxide powder.	35
Figure 2.7. The photograph of ultrasonic probe used for homogenizing the coating liquid for VO _x thin deposition.....	36
Figure 2.8. The photograph of 3.5x3.5-cm ² Si/SiN _x square substrates spin coated with ultrasonically homogenized sol at 2000 rpm for 1 min.....	37
Figure 2.9. The Sheet resistance vs Temperature plots for VO _x thin films annealed below 400°C.	38
Figure 2.10. The XRD characterization result of VO _x thin films spin coated at 2000 rpm and annealed at 120°C, 200°C, 300°C, and 400°C.....	39
Figure 2.11. The cross sectional SEM picture of sample spin coated at 2000 rpm and annealed at 120°C for thickness measurement.	39
Figure 2.12. The SEM pictures of VO _x thin films spin coated at 2000 rpm and annealed at different temperatures.	41
Figure 3.1. (a) The photograph of alumina substrate used in the TCR measurements. The schematic of circuit used for (b) temperature measurement and (c) resistance measurement.	45
Figure 3.2. The photograph of TCR measurement set-up.....	46
Figure 3.3. The circuit schematic of the noise measurement set-up.	46
Figure 3.4. The photograph of noise measurement set-up.	47
Figure 3.5. The noise power spectral density of a 75 kΩ metal resistor pair obtained under 20 μA bias current and its fitted curve.....	48
Figure 3.6. The (a) top and (b) perspective view of standard type planar electrodes.	49

Figure 3.7. The (a) top and (b) perspective view of finger type planar electrodes.	49
Figure 3.8. The representative cross sectional views of resistor formation steps.	50
Figure 3.9. The photographs of VO _x resistors after photolithography. 0.2 μm SiN _x layer was deposited on VO _x by PECVD in order to protect it from the photolithography chemicals. ..	51
Figure 3.10. The representation of one 4” wafer showing the location of dies including the microresistor structures by numbering.	52
Figure 3.11. The (a) Resistance and (b) TCR vs Temperature graph of a 55 kΩ finger type VO _x resistor under 10 μA bias current. The TCR at 25°C is -1.8 %/°C.	53
Figure 3.12. The (a) Resistance and (b) TCR vs Temperature graph of a 180 kΩ standard type VO _x resistor under 10 μA bias current. The TCR at 25°C is -1.7 %/°C.	53
Figure 3.13. The I-V curve of one finger type VO _x resistor.	55
Figure 3.14. The I-V curve of one standard type VO _x resistor.	55
Figure 3.15. The EDX spectrum of the Au pads of a VO _x resistor of which VO _x layer was etched by using H ₂ O ₂ (aq). The etchant was a mixture of DI water and 30 wt % H ₂ O ₂ in a volume ratio of 20:1 (H ₂ O:H ₂ O ₂) and etching duration was 10-30 sec.	56
Figure 3.16. The photographs of VO _x resistors after dry etching the VO _x layer with a gas mixture of Cl ₂ and Ar in MRIE equipment for (a) 50 sec and (b) 1.5 min.	58
Figure 3.17. The photographs of VO _x resistors (a) before and (b) after VO _x dry etching with CF ₄ and O ₂ gas mixture in the RIE equipment for 2 min.	59
Figure 3.18. The representation of a VO _x resistor of which wire bonding is performed in order to make 1/f noise test.	59
Figure 3.19. The (a) Resistance and (b) TCR vs Temperature plot of a 6 kΩ standard type VO _x resistor whose VO _x layer was deposited thicker and dry etched by using CF ₄ in the RIE equipment. The bias current was 10 μA. The TCR at 25°C is -1.7 %/°C.	60
Figure 3.20. The I-V curve of a standard type VO _x resistor whose VO _x layer was deposited thicker and dry etched by using CF ₄ in the RIE equipment.	60
Figure 3.21. The EDX spectrum of Au pads of a VO _x resistor of which VO _x layer was dry etched by using CF ₄ in the RIE equipment.	61
Figure 3.22. The (a) Resistance and (b) TCR vs Temperature plot of a 33 kΩ standard type VO _x resistor fabricated on a glass wafer and whose VO _x layer was etched with CF ₄ in the RIE equipment. The bias current was 20 μA. The TCR at 25°C is -2.4 %/°C.	63
Figure 3.23. The representative cross sectional views of VO _x lift-off process.	65
Figure 3.24. The photographs of some resistors after VO _x lift-off of the first fabrication run.	66

Figure 3.25. The photographs of some resistors after VO _x lift-off of the second fabrication run in which a thicker negative photoresist was used.	66
Figure 3.26. The (a) Resistance and (b) TCR vs Temperature graphs of a 90 kΩ standard type VO _x resistor fabricated by lift-off process. The bias current was 10 μA. The TCR at 25°C is -2.4 %/°C.....	67
Figure 3.27. The photograph of Si/Au/VO _x wafer piece pasted onto a 6” wafer (a) before and (b) after 30 sec VO _x RIE with 20-W power.....	69
Figure 3.28. The photographs of some resistors from the 6” Si/SiN _x wafer after the VO _x RIE had been performed at 20-W power for 45 sec.....	70
Figure 4.1. The photograph of SÜSS MicroTec PAV 200 equipment utilized in the thermal conductance, responsivity, and absorptance measurements.	74
Figure 4.2. The 3-D view of process steps for the fabrication of suspended single pixels [6].	75
Figure 4.3. The representation of one pixel having 35 μm pitch into which the developed sol-gel deposited VO _x material is going to be implemented during its fabrication.	78
Figure 4.4. The SEM photograph of one pixel after the VO _x layer was patterned and the photoresist was removed.....	79
Figure 4.5. The photographs of some pixels both under optical microscope and in the SEM after releasing by etching the polyimide in O ₂ plasma.....	80
Figure 4.6. The (a) Resistance and (b) TCR vs Temperature graphs of a 90 kΩ VO _x single pixel. The bias current was 2 μA. The TCR at 25°C is -2.4 %/°C.....	81
Figure 4.7. The SEM photograph of anchor of one suspended single pixel. There is some kind of residue all over the SiN _x field and on the gold metal lines.....	82
Figure 4.8. The responsivity measurement of pixel having the type shown in Figure 4.5a and resistance of 84 kΩ under 0.1 μA bias current at different modulation frequencies.	83
Figure 4.9. The photographs of VO _x test resistors of 35 μm pitch single pixels after the deposition and patterning of the VO _x layer.....	83

CHAPTER 1

INTRODUCTION

Uncooled thermal detectors for infrared (IR) imaging have been the subject of research and development for many decades and the technology has shown dramatic improvements in recent years. Although their sensitivity is not as high as that of cryogenically cooled detectors, their low cost (below \$10,000) compared to that of cooled detectors (typically \$50,000-\$150,000 when the whole camera system is considered) and also portability make them ideal for various infrared imaging applications such as drivers aid, industrial process monitoring, firefighting, portable mine detection, border surveillance, search and rescue, etc., requiring moderate performance.

Microbolometers are one type of uncooled thermal imagers which absorb electromagnetic radiation resulting in temperature increase, thus, changing resistance. A microbridge structure is generally fabricated on a read out circuit which also provides thermal isolation from the substrate. The thermometer part, which is the sensitive part to the IR radiation, resides in the middle of structure and electrical connection from the thermometer to the read out circuit is provided via metal legs. The associated relation which describes the resistance change of material with respect to temperature due to IR absorption is called temperature coefficient of resistance (TCR) and it is given by $TCR = (1/R)(dR/dT)$, where R is resistance, and T is temperature.

Various system parameters have been developed in order to describe the performance of infrared bolometer such as Responsivity, Noise Equivalent Power (NEP), Detectivity (D^*), and Noise Equivalent Temperature Difference (NETD). The NETD is one of the most important performance parameters for infrared imaging systems and it is defined as the temperature change in the target that generates a signal at the output of the detector which is equal to the total rms noise coming from four different noise sources: thermal (Johnson) noise, flicker noise (1/f noise), temperature fluctuation noise, and background fluctuation noise. Microbolometers having NETD below 100 mK have been demonstrated by several countries and the goal is to reach NETD values lower than 20 mK.

The NETD performance of microbolometers is mainly limited by two parameters which are TCR and 1/f noise [1,2]. Both TCR and 1/f noise are material properties. Therefore, bolometric materials having low 1/f noise and high TCR should be introduced for a high-performance detector. The material should also have low enough resistivity to be compatible with the read out circuit.

The most commonly used bolometric materials are vanadium oxide (VO_x) and amorphous silicon (a-Si). There are also efforts to implement resistive microbolometers by using

alternative bolometric materials such as poly-SiGe, Ge-Si-O, V-W-O, YBaCuO, and manganites. Among of all, doped or undoped VO_x seems to be the most appropriate one due to its low 1/f noise, high TCR and also, low resistivity relative to the others.

The resistivity change and optical properties of VO_x films strongly depend on the fabrication conditions and the resulting stoichiometry. That is, the crystallinity and content of vanadium oxidation phases play important role in the performance of thin film.

The utilized fabrication methods of VO_x thin films can be summarized as sputtering, physical vapor deposition, pulsed laser deposition, chemical vapor deposition, and sol-gel method. Among these techniques, sol-gel method attracts the attention due to its several advantages over others. First, it does not require a high vacuum chamber and the instrumentation is much simpler which decrease the cost of the technique. Large substrates can easily be coated. The deposition rate is higher. The distribution of dopants can be maintained uniformly in multicomponent oxide films. Because the starting materials are mixed on a molecular level, a very good chemical homogeneity can be obtained.

As a result, the objective of this study was determined as developing a sol-gel route for the fabrication of high performance vanadium oxide thin films and then, implementing it in the microbolometer fabrication technology. The rest of this chapter will give more detailed information about the IR spectrum, microbolometers, vanadium oxide system and sol-gel deposition of VO_x thin films.

Section 1.1 describes the infrared region of the entire electromagnetic spectrum. Section 1.2 briefly overviews the infrared detectors whereas Section 1.3 mentions microbolometers in more detail as one of the IR detectors. After introducing figures of merit for microbolometers in Section 1.4, literature survey conducted on various IR sensitive bolometric materials is presented in Section 1.5. Section 1.6 gives information about the vanadium oxide system chosen to be developed in this thesis among the IR sensitive bolometric materials. Finally, Section 1.5 gives the sol-gel deposition of VO_x thin films.

1.1. Infrared Radiation

Infrared light is an electromagnetic radiation whose wavelength is in the range of 0.75-1000 μm of electromagnetic spectrum. Figure 1.1 shows the IR part of the entire electromagnetic spectrum with its sub-regions [3].

Although IR radiation has a broad range, the most common windows that the IR detectors are designed for are 3-5 μm and 8-12 μm due to high IR light transmission of atmosphere in these wavelength regions as shown in Figure 1.2 [4]. As it is seen from the figure, transmittance is almost zero in some sub-regions making IR detection unattainable and high in some sub-regions making IR information available for the detector.

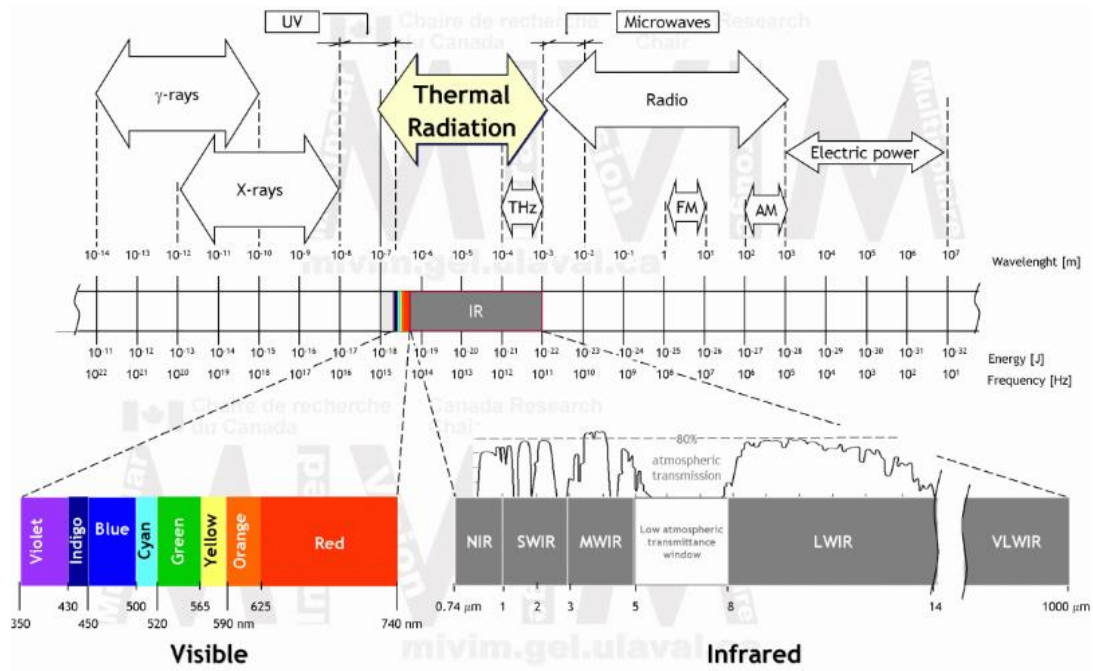


Figure 1.1. The infrared spectrum with its sub-regions in the entire spectrum [3].

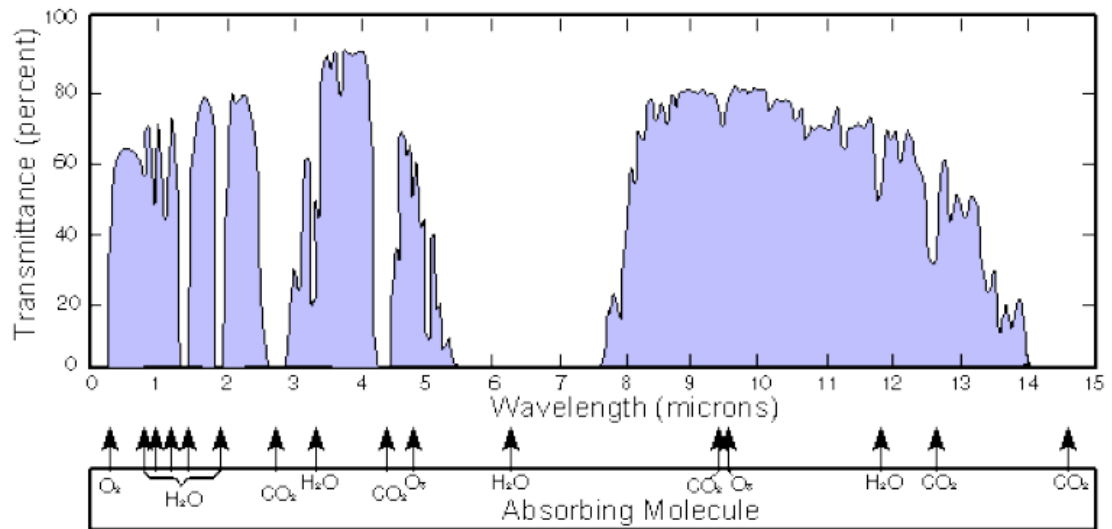


Figure 1.2. The IR light transmission of atmosphere and absorbing molecules [4].

The temperature range of target is another important aspect for the choice of spectral region to be detected by the IR detector. Spectral radiance at all wavelengths from a blackbody at a certain temperature is expressed by Planck's law:

$$M(\lambda, T) = \frac{2\pi hc^2}{\lambda^5 (e^{\frac{hc}{\lambda kT}} - 1)} \quad (1.1)$$

where $M(\lambda, T)$ is spectral radiance, h is Planck's constant, c is speed of light, λ is wavelength, k is Boltzmann constant, and T is object temperature.

The wavelength that the maximum radiance occurs (λ_{max}) can be found by taking the derivative of Eqn (1.1) and setting it to zero. The resulting relation is known as Wien's displacement law and given by

$$\lambda_{max} = \frac{2898}{T} \quad (1.2)$$

The spectral exitance with respect to wavelength for different temperatures is given in Figure 1.3 [5]. As it is seen, the maximum exitance occurs at smaller wavelengths as temperature increases. The wavelength of maximum exitance is around 10 μm for the objects at 300 K. Thus, the IR detectors used to detect the objects at room temperature are designed to sense 8-12 μm wavelength range. For hotter objects such as airplanes or missiles, the detectors are designed for the wavelength range of 3-5 μm since the maximum exitance occurs in that region.

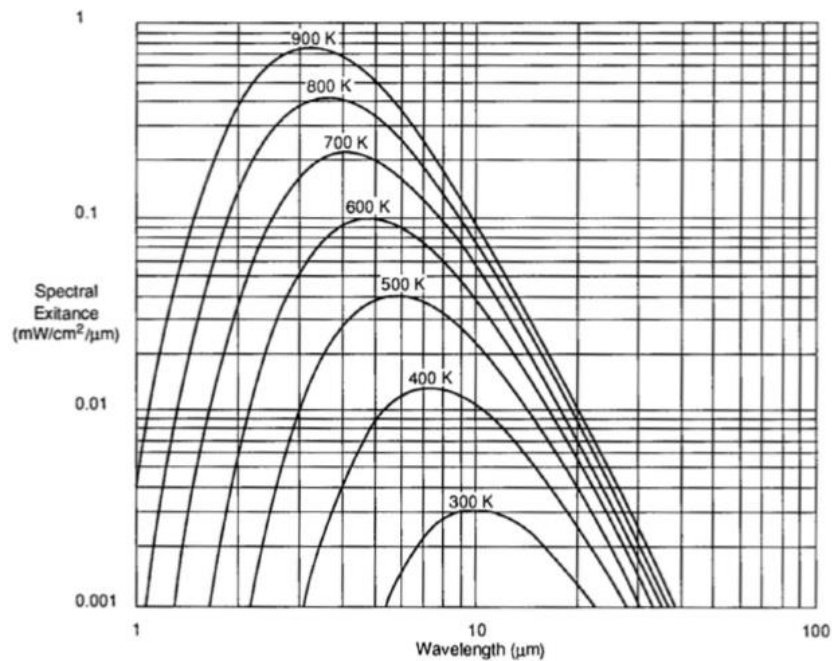


Figure 1.3. Spectral radiance with respect to wavelength at different temperatures [5].

1.2. Infrared Detectors

Infrared detectors can mainly be divided into two: photon detectors (cooled) and thermal (uncooled) detectors. In photon detectors, radiation is absorbed by the interaction of photons with the electrons of detector material. In thermal detectors, the absorption of incident radiation changes the temperature of detector material, thus, some physical property of the detector material which generates an electrical output. Both photon and thermal detectors are also divided into four main groups as shown in Figure 1.4.

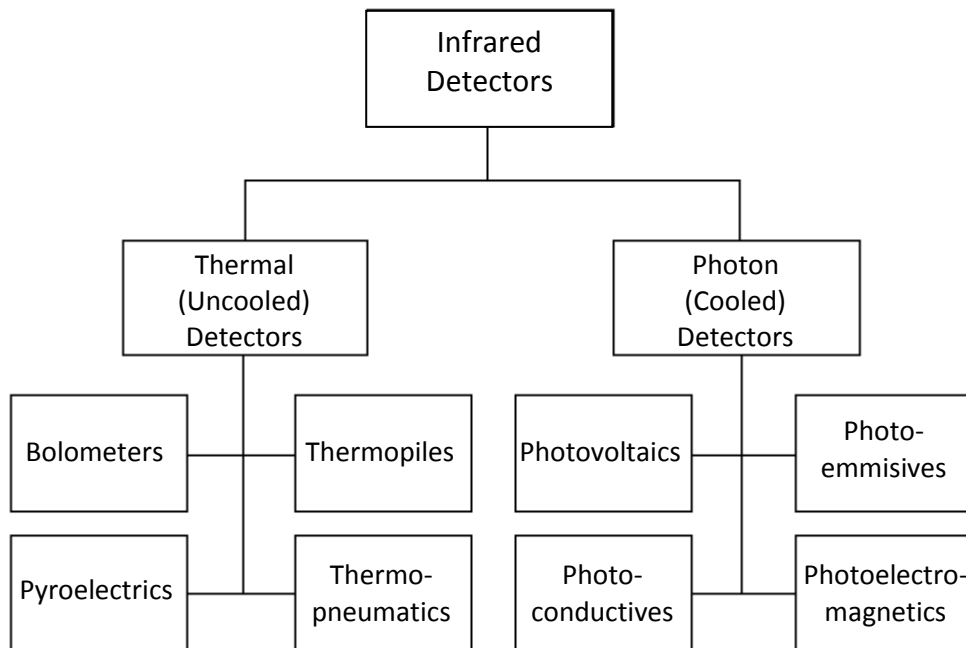


Figure 1.4. The classification of infrared detectors.

Photon detectors have very high signal-to-noise ratio and very fast response. They also have good wavelength selectivity enabling the production of multiband detectors. However, the main drawback is that they should be cryogenically cooled in order to maintain these properties, which increases the cost and weight of the system and prevents the extensive use of photon detectors. Therefore, they are mainly used in military, astronomy, and special medical instruments where the performance is more important than the cost [6].

The thermal detectors do not possess as high performance and fast response time as the photon detectors, however, their advantage is that they do not require cryogenic cooling which gives them the name of “uncooled detectors”. This fact allows the implementation of small, light, low-cost, and low power infrared camera systems which find usage in various civil and military application areas such as drivers aid, industrial process monitoring, firefighting, portable mine detection, border surveillance, search and rescue, etc. requiring

moderate performance [6]. As given in Figure 1.4, bolometers, which is the main concern of this thesis study, belongs to the group of thermal detectors and it will be mentioned in detail in the next section.

1.3. Microbolometers

“Bolometers are sensors that measure the amount of the incident infrared radiation like the other thermal detectors. The first bolometer was introduced in 1880s by Langley, who was able to detect a cow from a quarter mile distance. His first bolometer consisted of two platinum strips covered with lampblack. One of the strips was exposed to infrared radiation, while the other was shielded. The strips formed a Wheatstone bridge, and the infrared radiation was measured. Although there had been an effort to improve this bolometer structure, the size of the detectors was 1 mm or larger making the fabrication of large arrays impossible. In 1980s, Johnson and Higashi fabricated 100 μm sensors having a micromachined silicon nitride bridge structure of 1 μm thickness. In 1983, R. A. Wood demonstrated the first small arrays consisting of micromachined microbolometers. After that, a very fast progress was achieved in the array fabrication of microbolometers and large format arrays were demonstrated [6].”

Figure 1.5 shows a simplified view of one pixel from a microbolometer array [6]. A microbridge structure is generally fabricated on a read out integrated circuit (ROIC) which provides thermal isolation from the substrate. The IR active material resides in the middle and is electrically connected to the underlying ROIC via metal legs. When IR light coming from a target is incident on the pixel, it is absorbed by the absorber layer causing an increase in the temperature of IR active material and thus, a change in its electrical property. By this way, an electrical signal is induced and then, read by the ROIC.

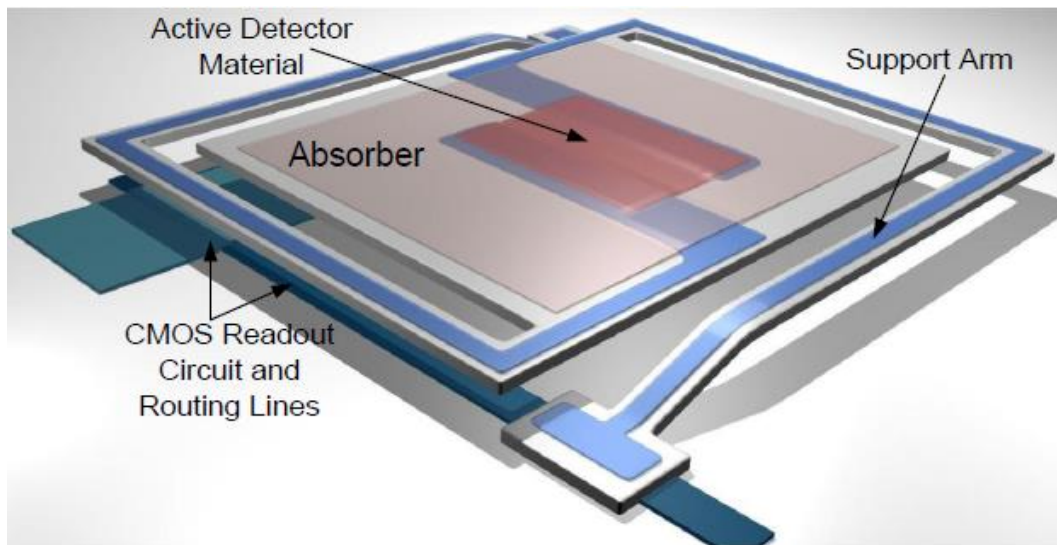


Figure 1.5. A simplified view of a microbolometer [6].

Microbolometers can be mainly divided into two types which are diode type microbolometers and resistive type microbolometers. In the former structure, the sensitive element is a diode and the varying parameter is current due to changing temperature. METU has developed such 64x64 and 128x128 microbolometer arrays [7,8]. Figure 1.6 shows an SEM image of those successfully fabricated arrays [6].

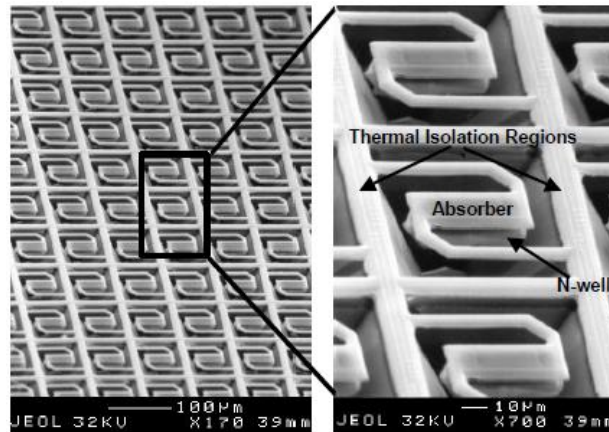


Figure 1.6. The SEM image of diode type microbolometer pixels fabricated at METU [6].

Mitsubishi Electric Corporation fabricated another type of detector using SOI-CMOS diodes. These detectors have a special infrared absorbing structure on the top of pixel letting the production of big focal plane arrays (FPA) in 320x240 and 640x480 formats. Figure 1.7 shows a SEM picture of a fabricated 640x480 array and a thermal image taken with this array [9].

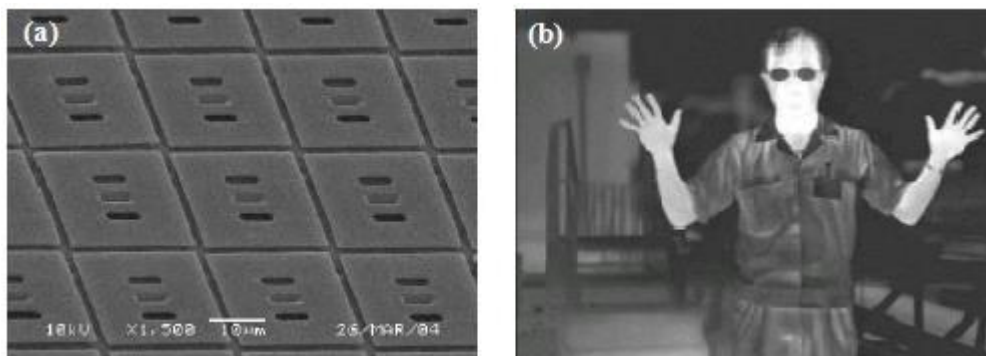


Figure 1.7. (a) The SEM image of 640x480 array fabricated by Mitsubishi and (b) the image taken with this array [9].

In resistive type microbolometers, the resistivity change of material with respect to temperature due to the IR absorption is utilized for imaging applications. There are a number of resistive type microbolometers on the market with pixel sizes of $25\ \mu\text{m} \times 25\ \mu\text{m}$ and array formats of 640×480 having Noise Equivalent Temperature Difference (NETD) better than 50 mK. At research level, there are uncooled detector FPAs with pixel sizes as small as $17\ \mu\text{m} \times 17\ \mu\text{m}$ allowing very large format FPAs such as 1024×768 to be implemented. The goal is to reach NETD values lower than 20 mK for these large-format FPAs [10,11].

Today, the dominating suppliers of high-performance uncooled infrared bolometer arrays are FLIR Systems, L-3, BAE Systems, DRS in USA, and ULIS in France. Other suppliers include Raytheon in USA, Mitsubishi and NEC in Japan, as well as SCD in Israel. Commercially available bolometer arrays are either made from vanadium oxide (VO_x), amorphous silicon (a-Si) or silicon diodes, with VO_x being the dominating technology. Figure 1.8 shows the SEM pictures of some state of the art microbolometers fabricated by different companies [2,12,13].

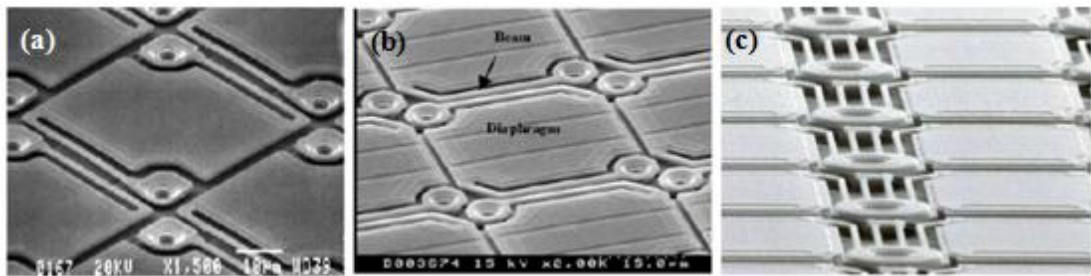


Figure 1.8. The SEM images of state of the art microbolometers fabricated by (a) Raytheon [12], (b) NEC [13], (c) BAE [2].

From the geometrical structure point of view, the pixel fill factor plays an important role in the performance of microbolometers. The bolometer pixel fill factor is defined as the pixel area that is used to absorb the incident IR radiation. The bolometer arms, the space between the adjacent bolometer membranes, and the vias that connect the bolometer and ROIC wafer consume the remaining area of the pixel. Conventional single-level IR bolometer arrays typically have a fill factor between 60 % and 70 %. To increase the bolometer pixel fill factor, two-layer bolometer designs (umbrella designs) have been reported that reach fill factors of up to 90 %. The bolometer legs, and in some cases the temperature sensing material are placed underneath the absorbing bolometer membrane. Such umbrella designs have been implemented in bolometer FPAs with very small pixel sizes. Figure 1.9 shows the SEM images of umbrella type bolometer arrays developed by different companies [14-16].

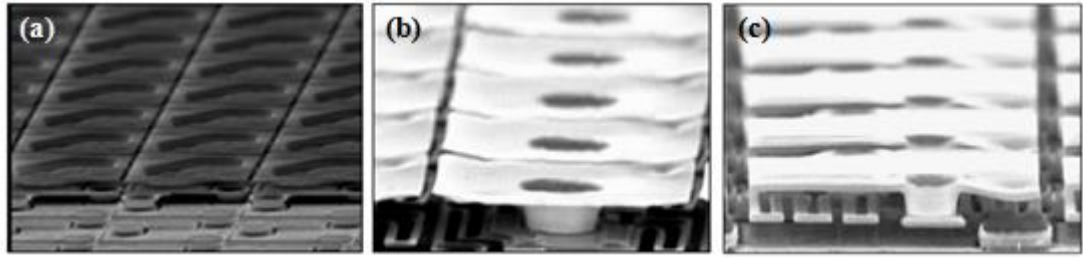


Figure 1.9. The SEM images of multilevel detectors fabricated by (a) NEC [14], (b) DRS [15], (c) Raytheon [16].

Most commercially available bolometer FPAs make use of standard single-level bolometer designs. However, as it is mentioned above, two-layer (umbrella-type) FPAs with very small bolometer pixels are in the R&D stage. Table 1.1 shows an overview of the main suppliers, bolometer technology and specifications for existing products and for bolometer arrays that are in the R&D stage [11,17].

Table 1.1. The commercial and state-of-the-art R&D microbolometer arrays [11,17].

Company	Bolometer Type	Array format (pixels)	Pixel pitch (μm)	NETD (mK) (F=1,20-60 Hz)
FLIR, USA	VO_x	160x120,640x480	25	35
L-3, USA	VO_x	320x240	37.5	50
	a-Si	160x120-640x480	30	50
	a-Si,a-SiGe	320x240,1024x768	17	30-50
BAE, USA	VO_x	320x240,640x480	28	30-50
	VO_x (standard type)	160x120,640x480	17	50
	VO_x (standard type)	1024x768	17	
DRS, USA	VO_x (standard type)	320x240	25	35
	VO_x (umbrella type)	320x240	17	50
	VO_x (umbrella type)	640x480,1024x768	17	
Raytheon, USA	VO_x	320x240,640x480	25	30-40
	VO_x (umbrella type)	320x240,640x480	17	50
	VO_x (umbrella type)	1024x768,2048x1536	17	
ULIS, France	a-Si	160x120,640x480	25-50	< 60
	a-Si	640x480,1024x768	17	< 60
Mitsubishi, Japan	Si diode	320x240,640x480	25	50
NEC, Japan	VO_x	320x240, 640x480	23.5	< 75
SCD, Israel	VO_x	384x288	17	35
	VO_x	640x480	25	50

METU has also developed 50 μm pixel 320x240 [6] and 35 μm pixel 384x288 [18] resistive type microbolometer FPAs. Figure 1.10 shows an image obtained by 35 μm pixel 384x288 microbolometer FPA fabricated at METU MEMS Center.



Figure 1.10. An image obtained by 35 μm pixel 384x288 microbolometer FPA fabricated at METU MEMS Center [18].

1.4. Figures of Merit for Microbolometers

The most important performance parameters for microbolometers will be presented in this section.

1.4.1. Temperature Coefficient of Resistance (TCR)

In resistive type microbolometers, the resistance of detector changes as temperature varies. The associated relation which is used to quantify the temperature dependence of detector's resistance is called temperature coefficient of resistance (TCR) and given by

$$\alpha = \frac{1}{R} \frac{dR}{dT} \quad (1.3)$$

where α is TCR in %/K, R is detector resistance at the temperature of interest, and T is temperature. TCR is a property of IR active material of detector and can be positive or

negative. Generally metals have positive TCR and semiconductors have negative TCR values [19].

1.4.2. Thermal Conductance (G_{th})

As mentioned previously, the pixels of a microbolometer are fabricated in the form of a microbridge structure in order to provide thermal isolation from the substrate and by this way, to increase the detector performance. The level of isolation is determined with the value of thermal conductance and the lower the thermal conductance is, the better the isolation is.

The thermal conductance of support arms, gas environment surrounding the detector, and radiative thermal conductance constitute three main components of total thermal conductance. Among these components, the second one can be neglected when a bolometer operating in a vacuum level of 0.01 mbar is considered.

The thermal conductance of support arms (G_{arm}) has an analogy with the electrical conductance and is expressed by

$$G_{arm} = \sigma \frac{A}{L} \quad (1.4)$$

where σ is the thermal conductivity of material used in the support arm, A is the cross sectional area of support arm, and L is the length of support arm.

Radiative thermal conductance (G_{rad}) is the loss of heat due to the radiation and is given by [20]

$$G_{rad} = 4A_D\eta\sigma T^3 \quad (1.5)$$

where A_D is active detector area, η is detector absorptance (equivalently emissivity), σ is Stefan's constant, and T is detector and surrounding temperature. In most of the cases, the radiative thermal conductance is much smaller than the thermal conductance of support arms. Therefore, it is neglected like the thermal conductance of gas environment surrounding the detector. As a result, the total thermal conductance becomes equal to the thermal conductance of support arms only.

1.4.3. Thermal Time Constant (τ)

Thermal time constant is a parameter showing how fast a detector heats up (or cools down) and given by

$$\tau = \frac{C_{th}}{G_{th}} \quad (1.6)$$

where C_{th} and G_{th} are thermal capacitance and thermal conductance of the detector, respectively. To achieve good detector performance at high frame rates, thermal time constant should be low enough. Although the characteristic of τ mainly depends on the application, it is commonly admitted that it should not exceed one-third of the reciprocal of the frame rate [21]:

$$\tau \leq \frac{1}{3x(\text{frame rate})} \quad (1.7)$$

In other words, for a microbolometer operating at 30-Hz frame rate, a time constant less than or equal to 10 ms would be appropriate for good performance.

1.4.4. Responsivity (R_V or R_I)

Responsivity is defined as the output signal of the detector per infrared radiation power incident on the detector. The output signal can be either voltage or current, therefore, responsivity has the unit of V/W or A/W, depending on how the detector is biased. If R_V is voltage responsivity and R_I is current responsivity, then,

$$R_V = \frac{\text{output voltage signal}}{\text{infrared radiation power}} = \frac{\Delta V}{P_0} \quad (1.8)$$

$$R_I = \frac{\text{output current signal}}{\text{infrared radiation power}} = \frac{\Delta I}{P_0} \quad (1.9)$$

where I is current, V is voltage, and P_0 is incident infrared radiation power.

Using the thermal parameters described in the previous sections, the thermal circuit of a microbolometer analogous to an electrical circuit can be represented as given in Figure 1.11. Thus, the infrared radiation power becomes equivalent to a modulated current source with a modulation frequency of ω . To find out the absorbed infrared radiation power, $P_0(\omega)$ is multiplied by the absorptance of detector which is η .

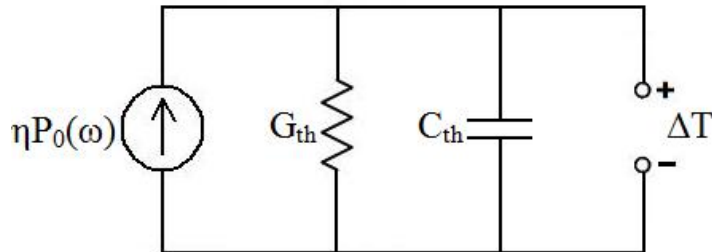


Figure 1.11. The representation of a microbolometer thermal circuit analogous to an electrical circuit.

From the circuit, the temperature change (ΔT) on the microbolometer can be written as

$$\Delta T = \frac{\eta P_0}{G_{th}\sqrt{1 + (\omega\tau)^2}} \quad (1.10)$$

where η is absorptance of the detector, P_0 is incident infrared power, G_{th} is thermal conductance of the detector, ω is modulation frequency of the infrared power, and τ is thermal time constant of the detector.

If the detector is biased with current, the change in the output voltage (ΔV) is given as

$$\Delta V = I_d \Delta R = I_d \alpha R_d \Delta T \quad (1.11)$$

where I_d is bias current of the detector, α is TCR of the detector's IR active material, R_d is detector resistance, and ΔT is temperature change. By substituting Eqn (1.10) into Eqn (1.11) and then, the resulting equation into Eqn (1.8), the voltage responsivity, R_V , can be obtained as

$$R_V = \frac{\eta I_d \alpha R_d}{G_{th}\sqrt{1 + (\omega\tau)^2}} \quad (1.12)$$

On the other hand, if the detector is biased with voltage, the change in the output current (ΔI) is expressed by

$$\Delta I = \frac{V_d}{R_d} - \frac{V_d}{R_d - \alpha R_d \Delta T} \approx -\frac{V_d}{R_d} \alpha \Delta T \quad (1.13)$$

where V_d is bias voltage of the detector, α is TCR of the detector's IR active material, R_d is detector resistance, and ΔT is temperature change. Again by substituting Eqn (1.10) into Eqn (1.13) and then, the resulting equation into Eqn (1.9), the current responsivity, R_I , can be obtained as

$$R_I = \frac{\eta V_d \alpha}{R_d G_{th} \sqrt{1 + (\omega\tau)^2}} \quad (1.14)$$

1.4.5. Noise Equivalent Power (NEP)

The noise equivalent power (NEP) is the amount of power incident on the detector that generates an output signal equal to the total root-mean-square (rms) noise of the detector. It has the unit of W and is given by

$$NEP = \frac{I_n}{R_I} \quad (1.15)$$

where I_n is total rms noise voltage, and R_l is current responsivity of the detector.

For resistive type microbolometers, there are four noise sources which are thermal (Johnson) noise, flicker noise (1/f noise), temperature fluctuation noise, and background fluctuation noise. Among these, temperature fluctuation noise, which originates from the random fluctuations in the detector temperature, and background fluctuation noise, which is due to the random fluctuations in the radiation power incident on the detector from the environment and the fluctuations in the radiation emitted by the detector itself, can usually be neglected when compared to thermal and flicker noise. Therefore, only thermal noise and flicker noise are generally taken into account during the performance calculations of microbolometers.

Thermal (Johnson) noise is generated by the thermal agitation of charge carriers inside an electrical conductor. This noise source exists regardless of any applied bias and has flat characteristics (white noise) over the entire band. The rms thermal noise current ($I_{n,th}$) are expressed as

$$I_{n,th} = \sqrt{\frac{4kT\Delta f}{R_d}} \quad (1.16)$$

where k is Boltzmann constant, T is temperature in K, R_d is detector resistance, and Δf is electrical bandwidth of the system.

Flicker noise is another type of electronic noise due to the conductance fluctuations with a 1/f spectrum which means that the spectrum is increasing with decreasing frequency, even sometimes extending to the frequencies as low as 10^{-4} Hz. It is therefore also referred to as 1/f noise. The physical origin of this noise has not yet been understood but, it is assumed to be due to a variety of effects, such as impurities in a conductive channel, generation and recombination noise in a transistor due to base current, imperfect contacts, and so on. It is always related to a direct current. That is, it is zero under no-bias conditions. Moreover, it is more dominant whenever electric currents are due to a very small number of charge carriers [22]. The rms flicker noise current ($I_{n,1/f}$) is given by

$$I_{n,1/f} = \sqrt{\int_{f_1}^{f_2} C_{1/f} \frac{I_d^2}{f^\beta} df} \quad (1.17)$$

where I_d is detector current, f is frequency, β is the exponent which is often equal to 1.0 ± 0.1 over six or more decades of frequency, f_1 and f_2 are lower and upper frequency limits of the electrical bandwidth, respectively, and $C_{1/f}$ is 1/f noise parameter. There is no analytical expression for $C_{1/f}$, however, it is known that it strongly depends on the deposition techniques and dimensions of detector material, electrical contacts, etc.

Taking the dominant noise sources into account only, the total rms noise current ($I_{n,total}$) is expressed by

$$I_{n,total} = \sqrt{I_{n,th}^2 + I_{n,1/f}^2} \quad (1.18)$$

1.4.6. Noise Equivalent Temperature Difference (NETD)

Noise equivalent temperature difference is the change in the target blackbody temperature that generates a signal at the detector output equal to the total rms noise. It has the unit of K and is expressed as [19]

$$NETD = \frac{(4F^2+1)I_n}{R_I \tau_0 A_D (\Delta P / \Delta T)_{\lambda_1-\lambda_2}} \quad (1.19)$$

where F is focal ratio of optics, I_n is total rms noise voltage, R_I is current responsivity of detector, τ_0 is transmittance of optics, A_D is active detector area, and $(\Delta P / \Delta T)_{\lambda_1-\lambda_2}$ is change of power per unit area radiated by a blackbody at temperature T and measured within the spectral band of $\lambda_1 - \lambda_2$.

NETD is one of the most useful performance parameter that enables evaluation of performance of all detection mechanisms. A low NETD value indicates that the detector is capable of sensing small temperature differences in the target.

1.4.7. Detectivity (D^*)

In order to compare the performance of different types of detectors having varying pixel sizes and different scanning rates, a parameter called Detectivity having the unit of $cm\sqrt{Hz}/W$ is defined as

$$D^* = \frac{R_I \sqrt{A_D B}}{I_n} = \frac{\sqrt{A_D B}}{NEP} \quad (1.20)$$

where R_I is current responsivity of detector, A_D is active detector area, B is electrical bandwidth of the system, I_n is total rms noise voltage, NEP is noise equivalent power of the detector.

1.5. Infrared Radiation Sensitive Bolometric Materials

The selection of bolometric material is the most crucial issue because, it directly determines or affects most of the performance parameters of a microbolometer. The main decisive factors that should be considered while selecting the appropriate material can be listed as its TCR value, noise performance, resistivity, and process compatibility.

The effect of TCR can easily be extracted from the expressions of Responsivity and NETD given in Eqn's (1.12) and (1.19), respectively. A high TCR means higher Responsivity and thus, lower NETD.

Flicker noise performance of the material is another important parameter. In order to minimize NEP and thus, NETD, the material's flicker noise should be as low as possible. Figure 1.12 shows the performance of a state-of-the-art IR imaging system based on a VO_x bolometer array fabricated by BAE Systems via measuring NETD [2]. This figure indicates that the performance is limited mainly by the $1/f$ noise of material and thus, points to the importance of $1/f$ noise performance of IR active material.

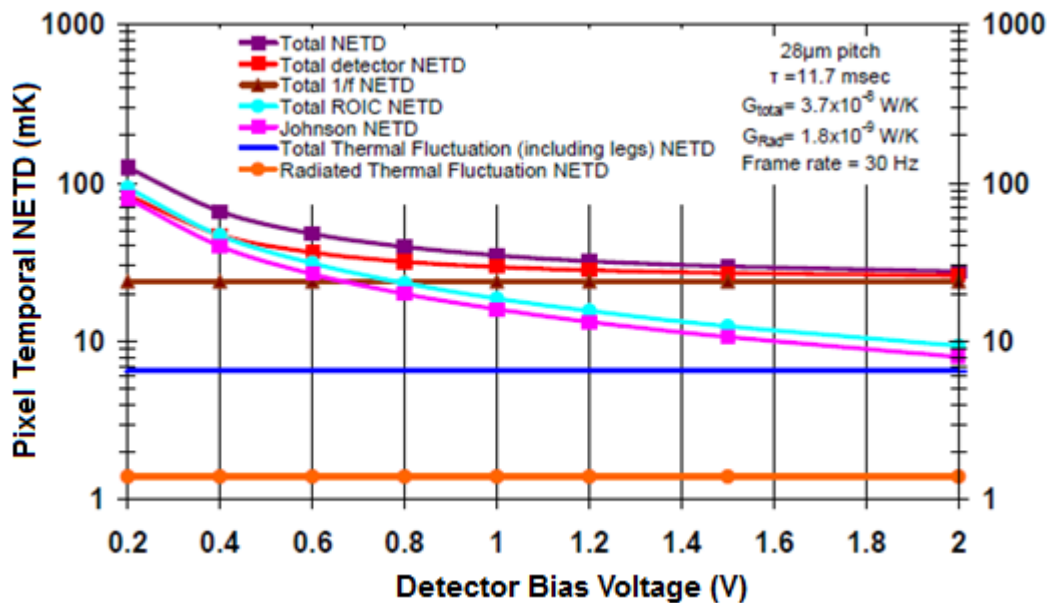


Figure 1.12. The NETD performance of VO_x microbolometer fabricated by BAE Systems [2].

The readout circuit planned to be integrated with the detectors for which the bolometric material is developed in this thesis study deals with the current noise of resistors. Therefore, by looking at Eqn (1.14) it is seen that it would theoretically be better to decrease resistance as low as possible in order to increase Responsivity, thus, decrease NEP and NETD. However, in practice this is not the case due to a problem named as “*self heating effect*” which is heating of the detector as a result of the applied electrical bias power. Assuming constant voltage bias, self heating effect increases as the resistance value of detector decreases. “*Reference detectors*”, which have the same electrical properties with the normal detector but are infrared blind, are used to distinguish self-heating from the effect of infrared power and reduce it to some extent, however, it cannot still be totally cancelled in practice. Thus, bias current should also be decreased for smaller resistance values which results in a higher NETD. Consequently, an optimum resistance which will give the minimum NETD

should be found which can be achieved through simulations. This analysis was performed in the context of previous thesis studies conducted at METU and it was found that the optimum resistance value lies between roughly 40 k Ω and 100 k Ω [6,18,23].

As it is well known from Ohm's law, besides the material's resistivity, the size of resistor also determines its resistance value. The maximum employable resistor size in a microbolometer pixel is of course not limitless but it is restricted with the pixel pitch (e.g. 50, 25, and 17 μm). Keeping this in mind, it is possible to construct different resistor structures which can mainly be divided into two groups, planar type and sandwich type resistors, whose representations are given in Figure 1.13. In planar type resistors, the active material resides in the planar gap between the metal electrodes and therefore, must have resistivity roughly below 100 $\Omega\cdot\text{cm}$ in order to maintain the resistance between 40 and 100 k Ω . On the other hand, in sandwich type resistors, the active material is placed between the top and bottom metallic film electrodes which permit to use semiconductor films having resistivity much higher than 100 $\Omega\cdot\text{cm}$. In this thesis study, it is planned to develop a bolometric material which will allow the use of planar type resistors inside a defined pixel pitch for two reasons: i) the fabrication of resistor will require less masking steps, ii) it is known that 1/f noise is lower in planar type resistors [6, 23-26].

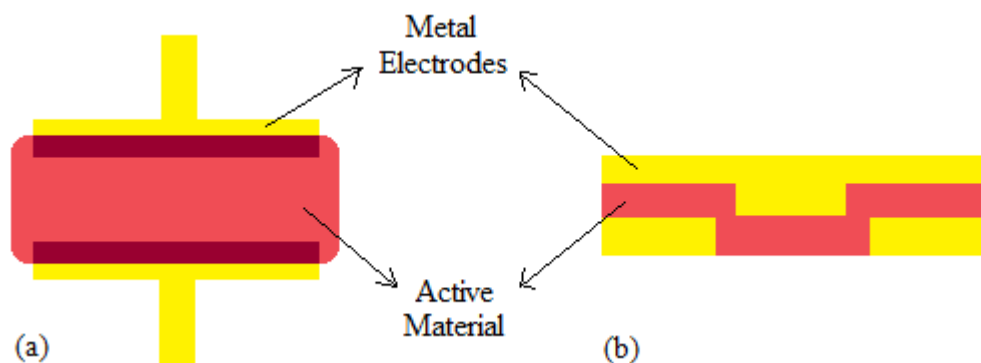


Figure 1.13. (a) The top view of a planar type resistor, (b) the cross sectional view of a sandwich type resistor.

Process compatibility is another concern while selecting a bolometric material. Above of all, the processing temperature of material should not exceed 450°C because, the temperatures above this value will damage the CMOS substrate on which the detector is fabricated and thus, do not allow the monolithic integration of detector with the CMOS substrate. In addition, the deposition technique of material should be reproducible and also compatible with other parts of detector.

As mentioned previously, commercially available resistive microbolometers are either made from vanadium oxide (VO_x) or amorphous silicon (a-Si), with VO_x being the dominating

technology. Besides these most commonly used bolometric materials, there are also efforts from various institutions and universities to implement resistive microbolometers by using alternative bolometric materials such as Si-Ge, Si-Ge-O, SiC, V-W-O, YBaCuO, and manganites. Manganites are in the structure of $\text{Ln}_{1-x}\text{A}_x\text{MnO}_3$ where Ln is a rare earth metal (La, Pr or Nd) and A is a divalent alkali earth metal (Ca, Ba or Sr). Some metals like Ti and Pt have also been investigated as a candidate bolometric material [27-29], however, the main drawback is that they have very low TCR value (i.e. smaller by an order of magnitude than that of their semiconductor counterparts) which precludes obtaining high performance from the microbolometer array.

The commercial companies do not give much detail about the characteristics and the fabrication process of material they use but, it is possible to find more detail in the published studies of institutions and universities. Table 1.2 compares the bolometric materials investigated in these studies in terms of deposition technique, process temperature, resistivity, TCR, and 1/f noise performance.

As mentioned earlier, the exact origin of 1/f noise has not been identified yet, but Hooge's law, which is a semi-empirical model given below, is used to compare the 1/f noise performance of different materials.

$$S_{I,\text{flicker}}(f) = C_{1/f} \frac{I_d^2}{f^\beta} = \frac{K I_d^2}{v f^\beta} \quad (1.21)$$

where $S_{I,\text{flicker}}(f)$ is flicker noise power spectral density having the unit of A^2/Hz , K is Hooge's constant, in other words, empirically obtained 1/f noise parameter, v is sample volume, I_d is detector's bias voltage, f is frequency, and β is equal to 1 for pink noise (1/f noise) characterized by constant power per octave. $C_{1/f}$ or K is a material property and it can vary several orders of magnitude for different resistive materials. Even small variations of the material composition can dramatically change $C_{1/f}$ or K . It is independent of the measuring conditions, such as current or voltage, thus, enables to directly make an evaluation of 1/f noise performance of different materials [30]. For most materials, $C_{1/f}$ parameter or K is not well documented in literature, however, it is still possible to find few data and compare the candidate bolometric materials' K (m^3) or $C_{1/f}$ (unitless) values as given in Table 1.2. As it is seen from Table 1.2, vanadium oxide seems to be the most appropriate material due to its low enough resistivity, 1/f noise parameter, process temperature, and high enough TCR. Manganites which also have low enough resistivity seem to be superior to VO_x in terms of 1/f noise performance, however, the main drawback is their very high deposition temperature which makes monolithic fabrication impossible. As a result, after surveying various bolometric materials which could be candidate for obtaining a high performance microbolometer, vanadium oxide has been chosen as the bolometric material to be developed in the context of this thesis study. The next section will give more detail about vanadium oxide system.

Table 1.2. Comparison of bolometric materials in terms of process temperature, resistivity, TCR and 1/f noise performance.

Material	Deposition Technique	Process Temperature (°C)	Resistivity (Ω .cm)	TCR (%/K)	1/f noise performance ($C_{1/f}$ or K value)	Ref.
V-W-O	Sputtering + Annealing	300	< 5	-3.0	$C_{1/f} = 6 \times 10^{-12}$	[31,32]
VO _x	Sputtering	< 450	< 5	-3.3	$K = 10^{-29} \text{ m}^3$	[33]
VO _x	Sputtering	< 450	0.16	-2.0	$K = 10^{-28} \text{ m}^3$	[34]
VO _x	Sputtering	< 300	0.1 to 100	-1.1 to -2.4	Nonspecified	[35]
VO _x	Sputtering + Annealing	300	0.02 to 0.1	-2.5	Nonspecified	[36]
VO _x	Sol-Gel	350	1	-2.0	Nonspecified	[37]
VO _x	Sputtering	450	< 1	-2.9	$C_{1/f} = 4 \times 10^{-11}$	[38]
a-Si:H	CVD	< 400	100 to 2000	-2.0	$K = 10^{-28} \text{ m}^3$	[39]
a-Si:H	CVD	150	435	-3.8	Nonspecified	[40]
poly-Si	Nonspecified	600	1 to 1000	-0.7 to -3.7	$K = 10^{-26} \text{ m}^3$	[34]
YBCO	Sputtering	25	< 33	-2.7 to -3.4	Nonspecified	[41]

Table 1.2 (cont'd). Comparison of bolometric materials in terms of process temperature, resistivity, TCR and 1/f noise performance.

Material	Deposition Technique	Process Temperature (°C)	Resistivity ($\Omega\cdot\text{cm}$)	TCR (%/K)	1/f noise performance ($C_{1/f}$ or K value)	Ref.
$\text{Ge}_x\text{Si}_{1-x}\text{O}_y$	Sputtering	25	4×10^3 to 12×10^3	-3 to -5	$C_{1/f} = 2.9 \times 10^{-11}$	[26,42]
$\text{Si}_x\text{Ge}_{1-x}\text{O}_y:\text{H}$	Sputtering + Annealing	250	$\sim 10^5$	-4 to -5	$C_{1/f} = 2.2 \times 10^{-10}$	[43,44]
a-SiGe:H	Chemical Vapor Deposition (CVD)	300	1.7×10^4	-4.3	Nonspecified	[45]
poly-SiGe (B doped)	CVD + Ion Implantation	550 to 1050	< 15	-1.8	Nonspecified	[46]
poly-SiGe	CVD	< 650	10	-2.5	$K = 10^{-26} \text{ m}^3$	[47]
SiC:H (B doped)	CVD	250	8.1×10^4	2.3	$C_{1/f} = 1.5 \times 10^{-10}$	[48]
SiC:H (B doped)	CVD	250	10^6 to 10^{10}	4.5 to 6.6	Nonspecified	[49]
$\text{La}_x\text{Sr}_{1-x}\text{MnO}_3$	Pulsed Laser Deposition (PLD)	780	< 0.01	1.7	$K = 9 \times 10^{-31} \text{ m}^3$	[50]
$\text{La}_x\text{Sr}_{1-x}\text{MnO}_3$	PLD + Annealing	800	< 0.1	2.5	$K = 2.2 \times 10^{-32} \text{ m}^3$	[51]
$\text{La}_x(\text{Sr,Ca})_{1-x}\text{MnO}_3$	PLD	750	< 0.01	4.4	$K = 1.6 \times 10^{-26} \text{ m}^3$	[52]

1.6. Vanadium Oxide System

Several transition metal oxides or sulfides are known to undergo a sudden metal-to-nonmetal transition over a certain temperature range. Their optical, electrical, and magnetic properties change considerably at these critical temperatures. Some of the vanadium oxide phases are among this group of materials exhibiting a transition behavior at critical temperatures.

The common oxidation states of vanadium are V^{2+} in VO, V^{3+} in V_2O_3 , V^{4+} in VO_2 , and V^{5+} in V_2O_5 . Additionally, several intermediate phases also exist in between. Figure 1.14 summarizes these oxide phases of vanadium [53].

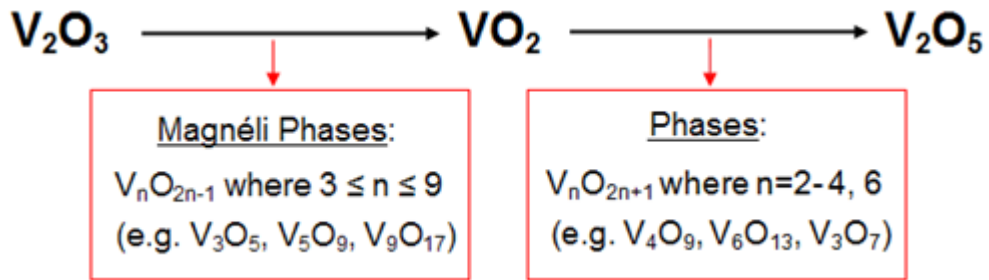


Figure 1.14. Oxide phases of vanadium [53].

All of the vanadium oxide phases except for VO, V_3O_7 , and V_7O_{13} exhibit a metal-insulator transition (MIT) of which temperature values are given in Table 1.3 [53,54].

Table 1.3. MIT temperatures of vanadium oxide phases [53,54].

Oxide Phase		Transition Temperature (K)
V_2O_3		155
Magnéli Phases	V_3O_5	430
	V_4O_7	238
	V_5O_9	135
	V_6O_{11}	170
	V_7O_{13}	---
	V_8O_{15}	68
	V_9O_{17}	79
VO_2		340
V_6O_{13}		150
V_2O_5		530

Among the phases in Table 1.3, vanadium dioxide (VO_2) attracts the attention because its MIT temperature is the most easily attainable one due to its closeness to room temperature and also, its optical properties appreciably change in the visible and near-IR region of the spectrum. It was first reported by Morin in 1959 [55] and since then has it been subjected to extensive research with the thought of utilizing VO_2 in a wide range of applications including thermochromic materials, electrical switches, optical storage, thermal sensors, etc. When considered from the microbolometer point of view, again VO_2 seems to be the most suitable oxidation phase due to its high enough TCR and low resistivity. The resistivity of V_2O_3 is also low enough to be implemented in microbolometers, however, its TCR is low because, it is in metallic state at room temperature. The TCR value of V_2O_5 is high, nevertheless, its resistivity is also high which makes it ROIC incompatible. Therefore, if vanadium oxide is to be used as the bolometric material, the thin film should be rich in VO_2 phase [56].

Vanadium dioxide undergoes a first-order semiconductor to metal transition at about $T_{tr} = 67^\circ\text{C}$. Below T_{tr} , it is a semiconductor whereas it becomes metallic at temperatures above T_{tr} . The resistivity and optical properties change abruptly at T_{tr} as it is seen in Figure 1.15 [54].

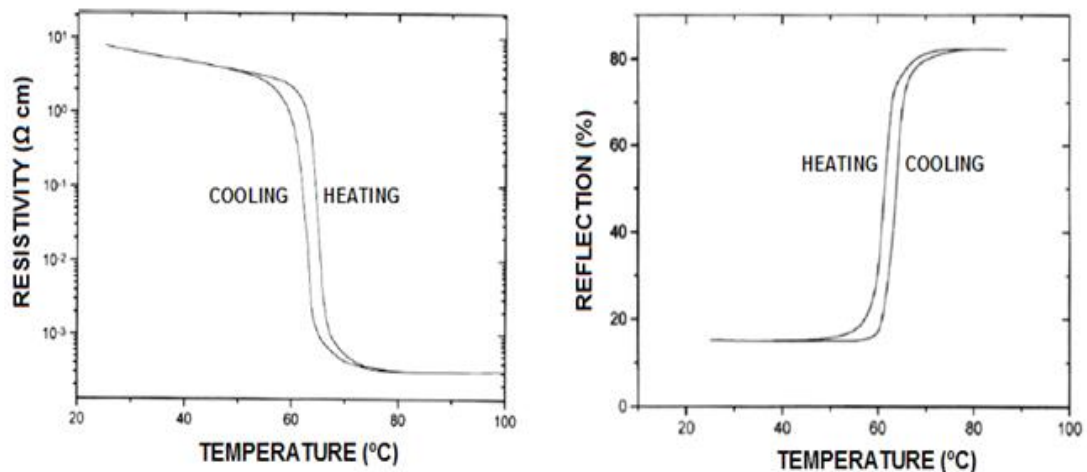


Figure 1.15. The MIT curves of VO_2 thin film [54].

The resistivity change of single crystal VO_2 is much more than that of polycrystalline VO_2 thin films during transition. Figure 1.16 compares the resistivity change of single and polycrystalline VO_2 [57]. The width of the hysteresis is as small as 1°C for single crystals whereas it ranges between 5 and 15°C for high quality thin films. Single crystals cannot withstand the stress during transition and they break after a few cycles. On the other hand, thin films survive during large number of cycles. It has been reported sol-gel derived VO_2 thin films could be cycled more than 10^8 without degradation [58].

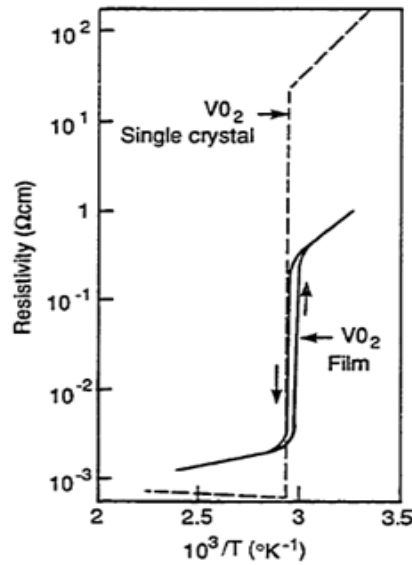


Figure 1.16. The resistivity change of single crystal and polycrystalline VO₂ thin film during transition [57].

Although transition temperature of VO₂ around 67°C is near to room temperature, it may still be too high for many practical applications. Therefore, doping of VO₂ has been tried extensively for a long time in order to manipulate T_{tr} and it is seen that large changes in transition temperature can be maintained with low doping levels (i.e. less than 1% in moles) keeping the MIT characteristics uncompromised [54]. Table 1.4 summarizes the doping effect of several ions [57].

Table 1.4. The effect of doping ions on the transition temperature [57].

Doping ion	ΔT_{tr} per atomic percent added (°C)	Structure at 300 K
Cr ³⁺	+3	Orthorhombic
Fe ³⁺	+3	Orthorhombic
Ga ³⁺	+6.5	Orthorhombic
Al ³⁺	+9	Orthorhombic
Ge ⁴⁺	+5	-
Ti ⁴⁺	-5.0 to -0.7	Orthorhombic
Re ⁴⁺	-4	Rutile
Ir ⁴⁺	-4	Rutile
Os ⁴⁺	-7	Rutile
Ru ⁴⁺	-10	Rutile
Nb ⁵⁺	-7.8	Rutile
Ta ⁵⁺	-5 to -10	Rutile
Mo ⁶⁺	-5 to -10	Rutile
W ⁶⁺	-28	Rutile

As it is seen in Table 1.4 the ions having smaller valance than V^{4+} raise T_{tr} whereas the ones with larger valance reduce it. As it is seen from the table, tungsten has the largest effect per atomic percent added. For instance, 1.0 atomic percent addition of tungsten reduces the semiconductor-to-metal transition by 22-28°C [59].

Another phase of vanadium oxide that is worth to mention due to its semiconducting properties is $V_2O_5 \cdot nH_2O$ gels which are actually composite materials made of solvent molecules (i.e. H_2O) trapped inside the network of V_2O_5 . As an illustration, the structure of $V_2O_5 \cdot nH_2O$ with $n=1$ is shown in Figure 1.17a [60]. The assembly consists of bilayer of single V_2O_5 layers made of square pyramidal VO_5 units between which water molecules are residing. Upon heat treatment, water molecules are removed and hydrated vanadium pentoxide turns into orthorhombic V_2O_5 of which crystal structure is shown in Figure 1.17b [61].

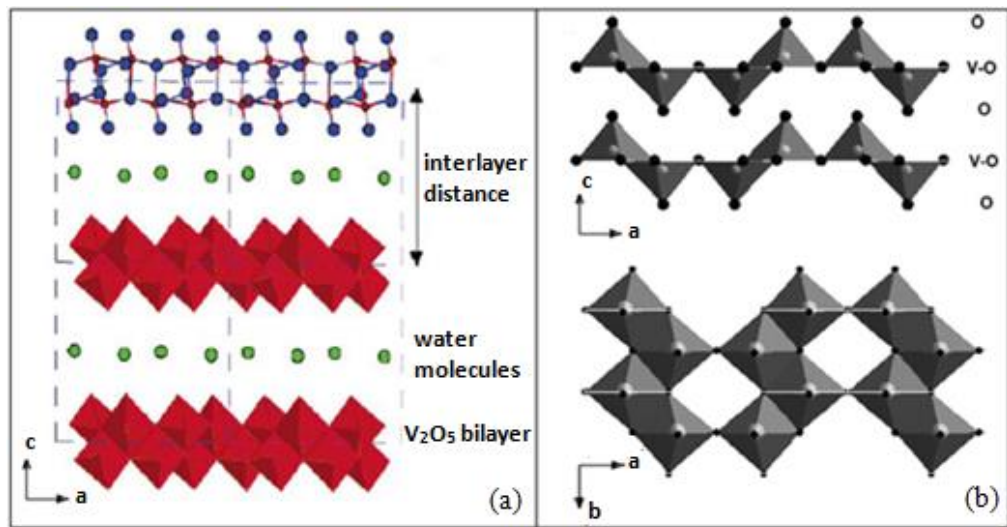


Figure 1.17. The structure of (a) $V_2O_5 \cdot nH_2O$ ($n=1$) [60], (b) V_2O_5 consisting of VO_5 square pyramid layers [61].

The studies show that the conductivity of $V_2O_5 \cdot nH_2O$ gels is much higher than the amorphous and even single crystalline V_2O_5 reaching to a value almost $1 \Omega^{-1} \cdot cm^{-1}$. Both electrical and ionic conductivity have contribution in the overall conductivity of V_2O_5 gels. V_2O_5 gels also contains small amount of V^{4+} ions (i.e. less than 1%), therefore, electrical conductivity arises from electron hopping between V^{4+} and V^{5+} ions, thus, it mainly depends on the amount of reduced V^{4+} ions. On the other hand, ionic conductivity arises from proton diffusion in the aqueous phase, therefore, it mainly depends on the hydration state n in $V_2O_5 \cdot nH_2O$ [62].

There are various deposition techniques to prepare thin films of vanadium oxide. These techniques include reactive magnetron and ion beam sputtering, reactive thermal and e-beam evaporation, pulsed laser deposition (PLD), chemical vapor deposition (CVD), atomic layer deposition (ALD) and sol-gel method. Among the listed fabrication techniques, sol-gel method attracts the attention due to its various advantages. First of all, it does not require a high vacuum chamber, thus, the instrumentation is much simpler and has low cost. Large substrates can easily be coated and the deposition rate is higher. More importantly, because the starting materials are mixed on a molecular level, the distribution of dopants can be maintained finely dispersed in the final product if a multicomponent oxide film is to be made so that chemically homogeneous coatings can be achieved.

For all of these reasons, it is decided to focus on sol-gel deposition of VO_x in this thesis study. A detailed literature survey about the sol-gel fabrication routes for vanadium oxide thin film fabrication was conducted and it will be given in the next section.

1.7. Sol-Gel Deposition of Vanadium Oxide

The sol-gel process, also known as chemical solution deposition, can be mainly divided into three steps, condensation, gelation, and heat treatment, as illustrated in Figure 1.18 [63].

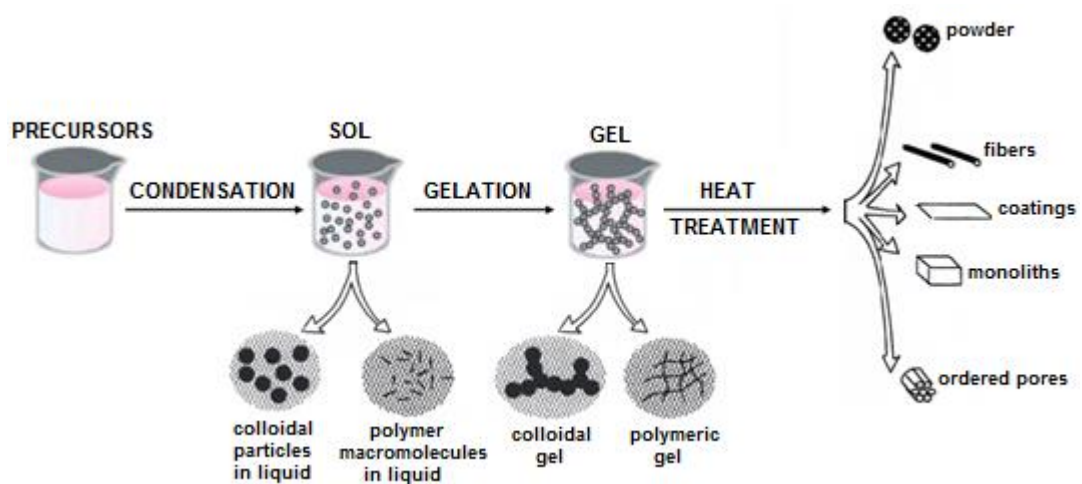


Figure 1.18. The process steps of sol-gel technique [63].

The first step starts with the mixing of precursors of desired materials. The reaction between the precursors leads to the formation of a sol which is suspension of colloidal or polymeric solid particles within a liquid. Then, these solid particles connect with each other resulting in a 3-dimensional solid network which expands in a stable fashion throughout a liquid medium. After this point, it is possible to produce different types of products by applying heat

throughout different procedures. For obtaining coatings (i.e. thin films), the sol or gel is deposited on the substrate by using one of the techniques among dipping, lowering, spinning, and spraying, represented in Figure 1.19 [57] and then, the thin film is heat treated.

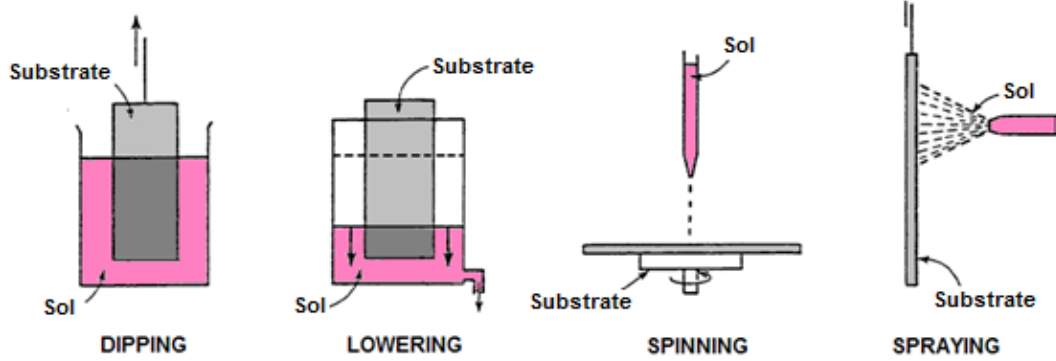
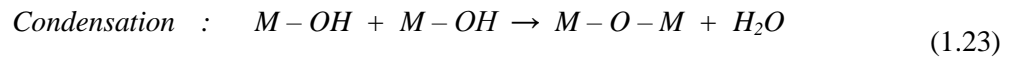
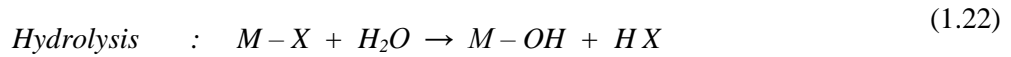
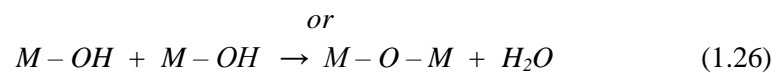
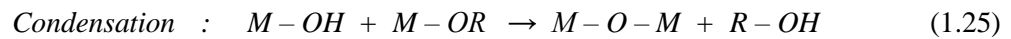
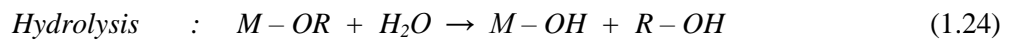


Figure 1.19. Representation of sol-gel coating techniques [57].

In sol-gel process, all types of precursors can be used provided that they are miscible. However, two main precursor groups are distinguished which are metallic salts (M_xN_y) and alkoxides ($M(OR)_n$) where M is a metal, N is an anionic group, and R is an alkoxy group. The solvent is selected according to the precursor. It can be either water or organic liquid. If the precursor is a metallic salt, then the reactions taking place are mainly as follows:



If the precursor is an alkoxide, then the reactions are



The sol-gel method has been widely employed for fabricating vanadium oxide thin films because of its various advantages mentioned in the previous section. The sol-gel route to be followed depends on the choice of precursor. The precursors used in the deposition of VO_x can be mainly grouped into three: i) V^{3+} precursors, ii) V^{4+} precursors, and iii) V^{5+} precursors. V^{3+} precursors lead to formation of V_2O_3 films and V^{4+} precursors lead to VO_2 films. Heat treatment of them in O_2 atmosphere will produce higher oxidation states. In order to crystallize these films in the form of V_2O_3 or VO_2 , the heat treatment atmosphere should be

inert. Using V^{5+} precursors results in formation of V_2O_5 and then, it can be reduced to lower oxidation states by heating the thin film again under inert or reducing atmosphere which includes gases such as CO or H_2 .

Having surveyed literature in detail, the possible routes of sol preparation for VO_x thin film fabrication can be summarized as follows:

- 1) Dissolving a vanadium alkoxide in the form of $VO(OR)_3$ in an alcohol
- 2) Dissolving a vanadium alkoxide in the form of $V(OR)_4$ in an alcohol
- 3) Dissolving molten V_2O_5 powder in distilled water
- 4) Dissolving V_2O_5 powder in aqueous H_2O_2
- 5) Dissolving metallic vanadium powder in aqueous H_2O_2

Alkoxides have been one of the mostly employed precursors in literature, however, one disadvantage is that they are sensitive to humid air leading to difficulty in keeping them stable. Their cost may also be expensive relative to the others. Moreover, dissolving the alkoxide in an alcohol may result in undesired carbon content in the final product. In the third route above, molten V_2O_5 powder means increasing the temperature to at least $690^\circ C$ which is the melting point of it.

As a result, among the sol preparation routes listed above, the fifth route, which is dissolving metallic vanadium powder in aqueous H_2O_2 , is chosen to be implemented in the fabrication of VO_x thin film in this thesis study due to precursors' being easy to handle as well as the simplicity of the route.

1.8. Research Objectives and Thesis Organization

This thesis study aims to develop a high performance bolometric material for microbolometers. Vanadium oxide is the bolometric material to be developed and the sol-gel deposition technique is the method to be utilized. For this purpose, the following research objectives are aimed:

1. *Optimization of sol preparation, thin film deposition, and material characterization.* The sol-gel route should be optimized in order to obtain a homogeneous coating liquid for the deposition of uniform VO_x thin films. The characteristics of products of coating liquid (i.e. thin film and powder) should also be investigated. After the optimum coating liquid is achieved, uniform VO_x thin films should be prepared in order to characterize its phase, morphology, thickness, and resistivity.
2. *Microresistor fabrication for testing the bolometric performance of sol-gel deposited VO_x .* Surface micromachined MEMS technology will be utilized for the fabrication of VO_x microresistors. The deposition of VO_x thin film and the other fabrication steps should be compatible with each other. That is, neither VO_x deposition should give harm to other layers nor should other fabrication steps degrade the VO_x thin film. Moreover, the VO_x thin film should possess physical and chemical uniformity, stability, good

coverage, good adhesion, and reproducibility. The etching of VO_x layer will be a new concern; therefore, its etching method should be determined and optimized. After the VO_x microresistors are fabricated successfully, their resistance, TCR, and 1/f noise should be investigated.

3. *Fabrication of microbolometers using the sol-gel deposited VO_x thin film and conducting performance tests.* The fabrication of suspended single pixels is aimed firstly in order to implement the sol-gel deposited VO_x into the microbolometer technology. If this fabrication is achieved, the performance tests which are TCR, 1/f noise, thermal conductance, responsivity, thermal time constant, and IR absorptance measurements will be conducted. Then, the fabrication of a microbolometer focal plane array (FPA) on a ROIC wafer utilizing the developed sol-gel deposited VO_x is aimed. If the fabrication is succeeded, the performance of arrays will be tested and thermal images will be obtained.

The organization and content of the chapters are summarized below:

Chapter 2 mentions the optimization trials of sol-gel route and characterization of powder obtained as a product of the route. Deposition and characterization results of sol-gel deposited VO_x thin films are given in the same chapter.

Chapter 3 gives the fabrication of microresistors with sol-gel deposited VO_x thin films. The resistance, TCR, and 1/f noise measurement results are also given in this chapter.

Chapter 4 presents the fabrication of 35 μm suspended single pixels as a first step for the implementation of sol-gel deposited VO_x material into microbolometer technology. The chapter also gives the performance test results of the pixels such as responsivity, thermal conductance, etc.

Chapter 5 summarizes the studies conducted in order to fabricate 384x288 microbolometer array on a ROIC wafer in which the sol-gel deposited VO_x is planned to be used as the bolometric material.

Finally, Chapter 6 summarizes the results and achievements obtained in the scope of this thesis and gives the suggestions on the possible future work.

CHAPTER 2

OPTIMIZATION OF SOL PREPARATION, THIN FILM DEPOSITION AND MATERIAL CHARACTERIZATION

In order to develop a sol-gel route for the fabrication of high performance VO_x thin films and then implement it in the microbolometer fabrication technology, first, the preparation of coating liquid for obtaining VO_x thin films was optimized. Second, the powder obtained by drying the optimized coating liquid was characterized. Section 2.1 gives the details of these mentioned studies. Section 2.2 presents the preparation of VO_x thin film samples and Section 2.3 gives the characterization results of prepared VO_x thin films. Finally, Section 2.4 summarizes the obtained results and concludes the chapter.

2.1. The Optimization of Sol Preparation and Its Characterization

Among various sol preparation routes present in literature, the route of dissolving metallic vanadium powder in aqueous H_2O_2 [64] has been chosen to be implemented in the fabrication of VO_x thin film in this thesis study due to the precursors' being easy to handle as well as simplicity of the route.

The route can be described as follows: Given amount of metallic V powder is dissolved in H_2O_2 (aq) stirring in an ice-cooled water bath due to the exothermic nature of dissolution reaction. After several hours, the color turns into reddish brown and an acidic solution of polyvanadate is formed. Then, ice-cooling is stopped, the solution is immediately vacuum filtered for the removal of undissolved impurities, and then, brought to room temperature while stirring gently. During this step, excess H_2O_2 decomposes giving off O_2 and a brown hydrosol forms. Finally, the coating liquid is prepared in two different ways: i) letting the brown hydrosol stand at room temperature for some time and using it directly as the coating liquid, ii) drying the brown hydrosol to obtain a solid material and then mixing this solid material with pure water [64].

The experimental set-up assembled in order to realize the above mentioned sol preparation route and followed process steps are shown in Figure 2.1. As it is seen, a double vesseled Erlenmeyer flask which is connected to a water bath and ice-cooled by continuously circulating cold water through its vessels was used for the dissolution reaction to take place.

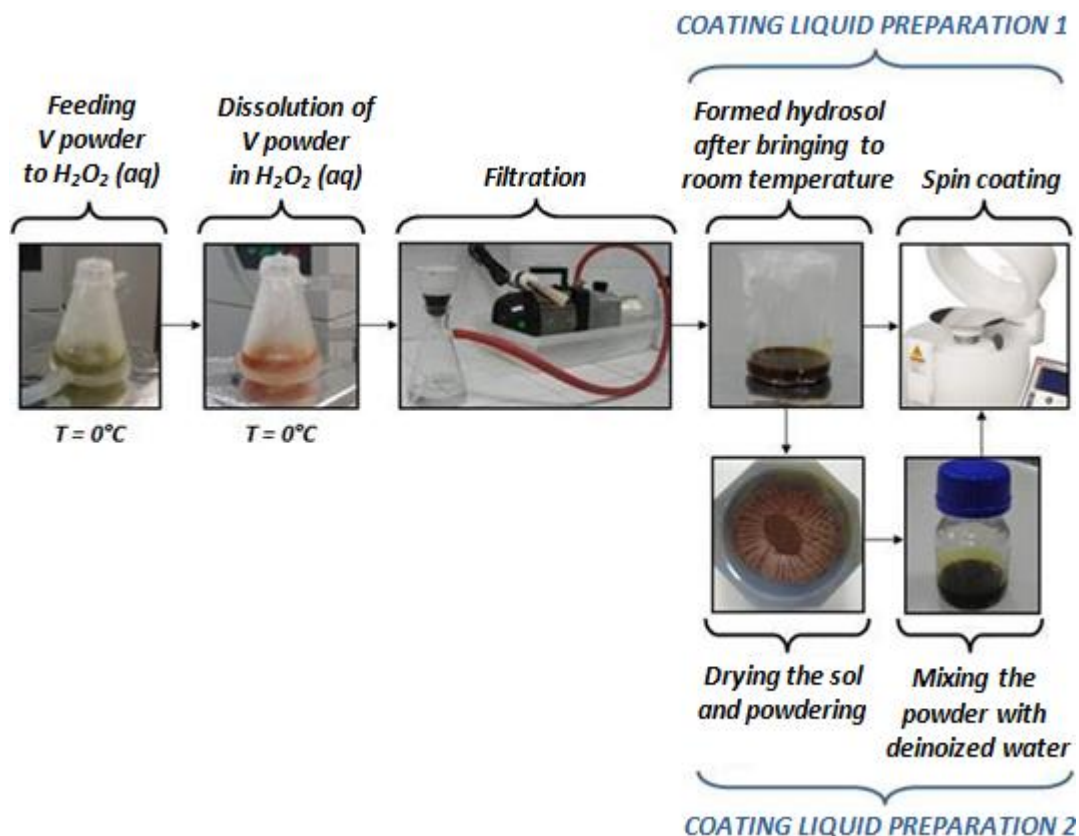


Figure 2.1. The assembled experimental set-up and process steps of sol-gel route for preparing the coating liquid of VO_x thin film deposition.

Several experimental runs were performed in order to optimize the dissolution step. The details of these experimental runs and what kind of observations was made are summarized in Table 2.1.

As a result, Run 4 was chosen to be the optimum dissolution procedure due to the fact that V powder seemed to be dissolved completely and also, the decomposition of excess H_2O_2 was more controllable. The amounts were always scaled up keeping the molar ratio of H_2O_2 to vanadium constant at a value of 45.

Before preparing VO_x thin films, a glassy solid material shown in Figure 2.2a was obtained by drying the sol formed in Run 4 at $80^\circ C$ for 22 hours. The sol was kept in a high density polyethylene container during drying. Then, this solid material was powdered in an agate mortar as given in Figure 2.2b for its characterization.

Table 2.1. The summary of experimental runs of different dissolution processes.

EXPERIMENTAL RUN	OBSERVATIONS
<p><u>RUN 1</u></p> <p>Dissolving V powder in 30 wt % H₂O₂ (aq) for 2-3 h at 0°C</p> <p>H₂O₂ to V molar ratio = 45</p>	<p>There remains small amount of undissolved V powder after 2-3 h.</p> <p>When the solution is brought to room temperature after dissolving process, H₂O₂ decomposes very fast and violently, bubbling (O₂ evolving) stops in 15 minutes, the liquid spills over, a viscous dark brown liquid is formed immediately.</p> <p>When dried and powdered, brown material is formed.</p>
<p><u>RUN 2</u></p> <p>Dissolving V powder in 15 wt % H₂O₂ (aq) for 2-3 h at 0°C</p> <p>H₂O₂ to V molar ratio = 22.5</p>	<p>There remains small amount of undissolved V powder.</p> <p>When the solution is brought to room temperature after dissolving process, H₂O₂ decomposes slowly, bubbling (O₂ evolving) stops in 45 minutes, the liquid does not spill over, dark brown flocculates in an orange mother liquid are formed.</p> <p>When dried and powdered, brown material is formed.</p>
<p><u>RUN 3</u></p> <p>Dissolving V powder in 10 wt % H₂O₂ (aq) at room temperature</p> <p>H₂O₂ to V molar ratio = 15</p>	<p>The reaction is completed in 15 minutes. That is, bubbling stops in 15 minutes. Dark brown flocculates precipitating at the bottom are formed in yellow mother liquid.</p> <p>When dried and powdered, a black material is formed.</p>
<p><u>RUN 4</u></p> <p>Dissolving V powder in 30 wt % H₂O₂ (aq) for 5-6 h at 2°C</p> <p>H₂O₂ to V molar ratio = 45</p>	<p>All V powder seemed to be completely dissolved after 6 hours.</p> <p>When the solution is brought to room temperature after dissolving process, O₂ evolving starts slowly and then, progressively gathers speed. The liquid tends to rise as if it is going to boil over, however, it does not spill over. Bubbling stops immediately after that and then, a red brown viscous liquid is formed.</p> <p>When dried and powdered, red brown material is formed.</p>

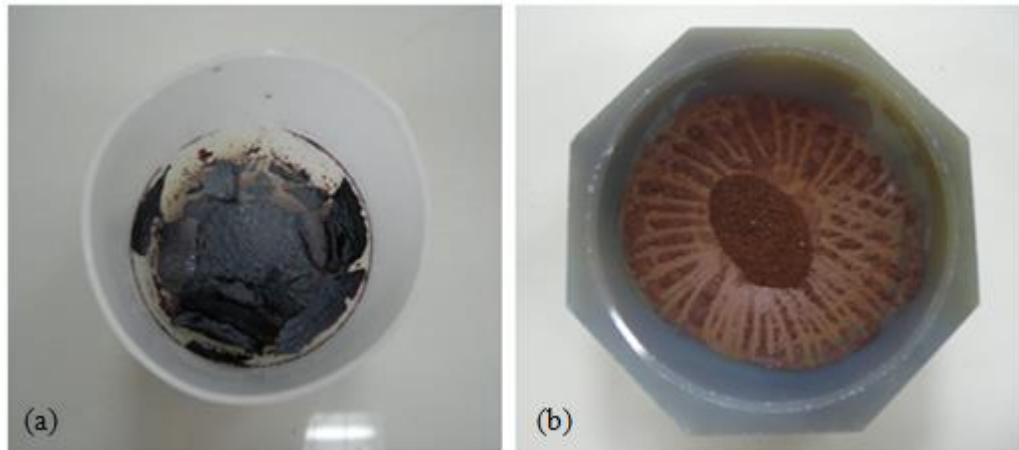


Figure 2.2. The photograph of (a) solid material obtained by drying the sol formed in Run 4 in Table 2.1 in a high density polyethylene container at 80°C for 22 hours and (b) its powdered form in an agate mortar.

First, the X-Ray Diffraction (XRD) pattern of this powder was taken by using Rigaku X-ray Diffractometer D/Max-2000 PC found in METU Metallurgical and Materials Engineering Department. The sample was scanned by Ni-filtered CuK α radiation (40 kV) with a rate of 2°/min between 2 θ angle of 5° and 80°. Figure 2.3 shows the taken XRD pattern.

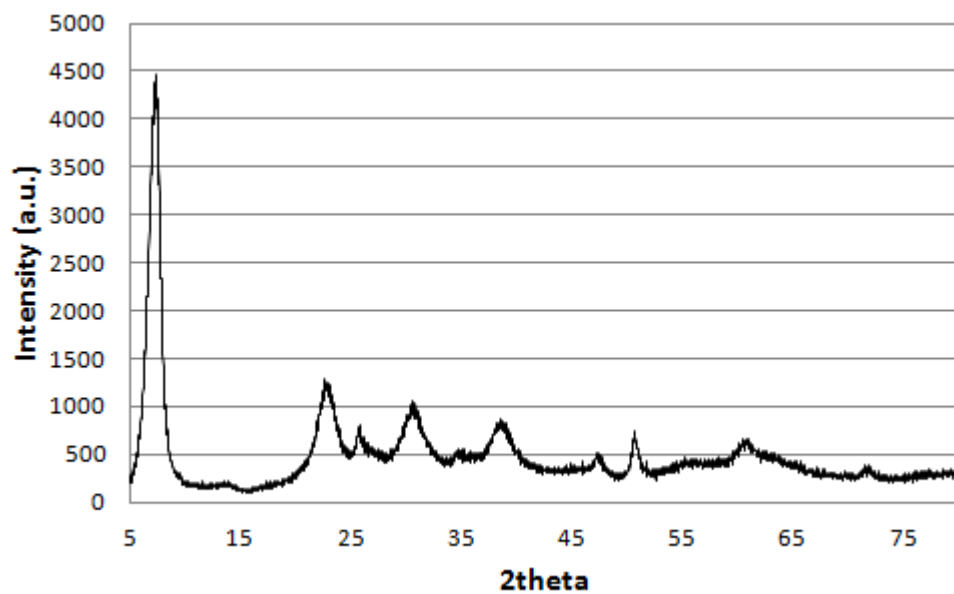


Figure 2.3. The XRD pattern of powder obtained after drying the sol formed in Run 4 in Table 2.1.

The pattern in Figure 2.3 indicates hydrated vanadium pentoxide ($V_2O_5 \cdot nH_2O$ with $n \leq 1.8$) which has a structure intermediate between the amorphous and crystalline state as proposed by Hibino et al. [65]. As an illustration, the structure of $V_2O_5 \cdot nH_2O$ with $n=1$ is shown in Figure 1.17 in Section 1.6. Upon heat treatment, water molecules are removed and hydrated vanadium pentoxide turns into orthorhombic V_2O_5 as mentioned earlier.

For observing the thermal properties of powder sample, simultaneous Differential Thermal Analysis and Thermogravimetric Analysis (DTA/TGA) were performed at METU Central Laboratory. The analysis was made in two different atmospheres, air and N_2 . Samples were heated from room temperature to $500^\circ C$ in air atmosphere and to $600^\circ C$ in N_2 atmosphere with a rate of $5^\circ C/min$. The result of air DTA/TGA is given in Figure 2.4.

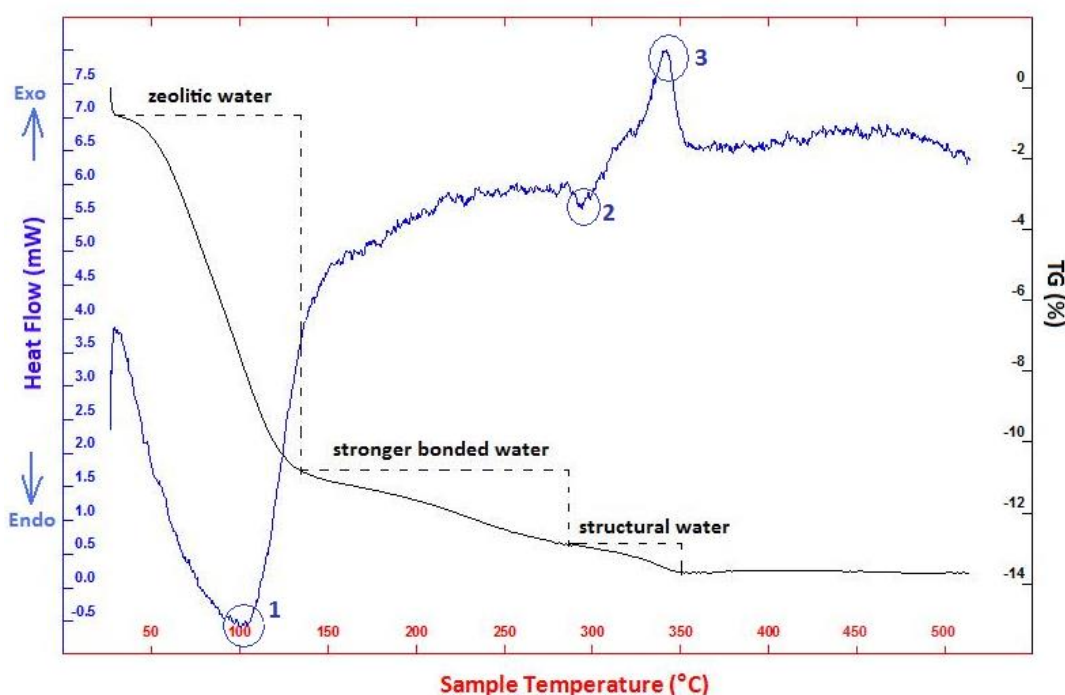


Figure 2.4. The DTA/TGA curve of powder sample in air atmosphere at a heating rate of $5^\circ C/min$.

When the TGA curve in Figure 2.4 is analyzed, it can be deduced that zeolitic (weakly bonded) water removal occurred between $25-135^\circ C$, stronger bonded water is removed between $135-290^\circ C$, structural water is removed between $290-350^\circ C$ [66].

In DTA curve, the peaks upwards indicate exothermic reactions and the peaks downwards indicate endothermic reactions. Phase transitions, dehydration, reduction and some

decomposition reactions have endothermic nature, whereas crystallization, oxidation, and some decomposition reactions have exothermic nature.

When the DTA curve in Figure 2.4 is analyzed, it is seen that the endothermic peaks at 100°C and 295°C (designated as 1 and 2 in the figure, respectively) are due to dehydration and the exothermic peak at 340°C (designated as 3 in the figure) is due to crystallization. The XRD patterns of heat treated thin films which will be given in Section 3.2 also support Peak 3 at 340°C.

The DTA/TGA curve of powder sample heated in N₂ atmosphere between room temperature and 600°C is given in Figure 2.5. It very resembles the curve obtained in air atmosphere. However, different than Figure 2.4, it seems there exists an endothermic peak at around 550°C (circled region in the figure) which may indicate some kind of reduction process of V₂O₅ to lower oxides. Nevertheless, it is necessary to see the continuation of the curve at temperatures higher than 600°C and make additional other kind of characterization to speak definite.

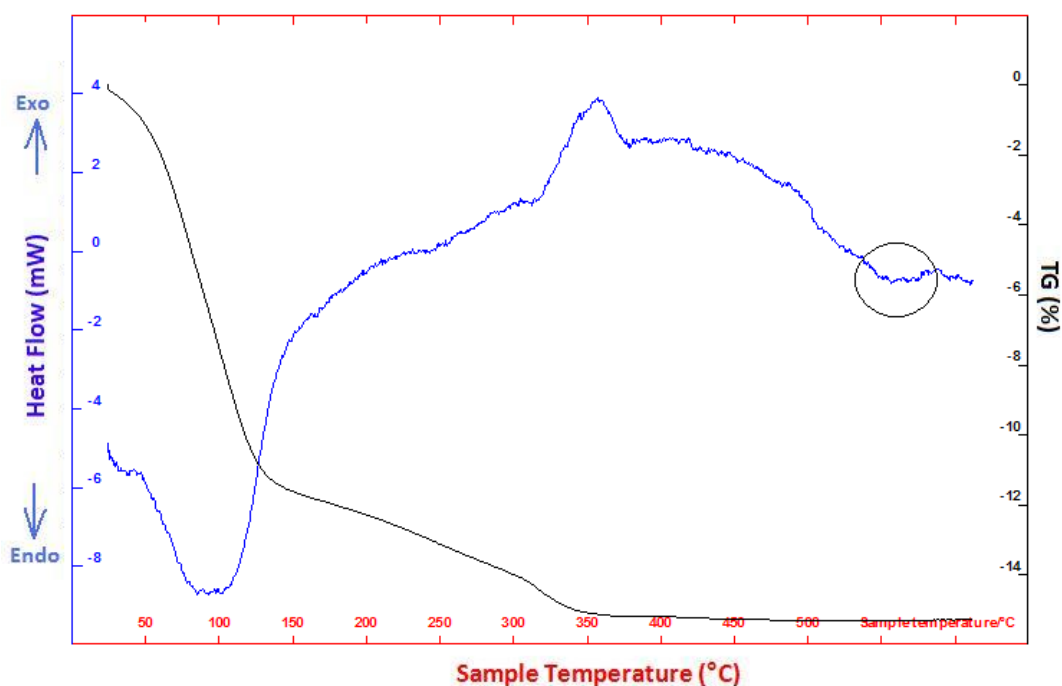


Figure 2.5. The DTA/TGA curve of powder sample in N₂ atmosphere at a heating rate of 5°C/min.

Finally, Energy Dispersive X-ray Spectroscopy (EDX) analysis of hydrated V₂O₅ powder was performed by utilizing Fei Nova Nano SEM 430 Field Emission Scanning Electron Microscope (FESEM) found in METU Metallurgical and Materials Engineering Department

and no peak belonging to any element other than vanadium and oxygen was detected in the sensitivity limits of EDX technique as it is shown in Figure 2.6.

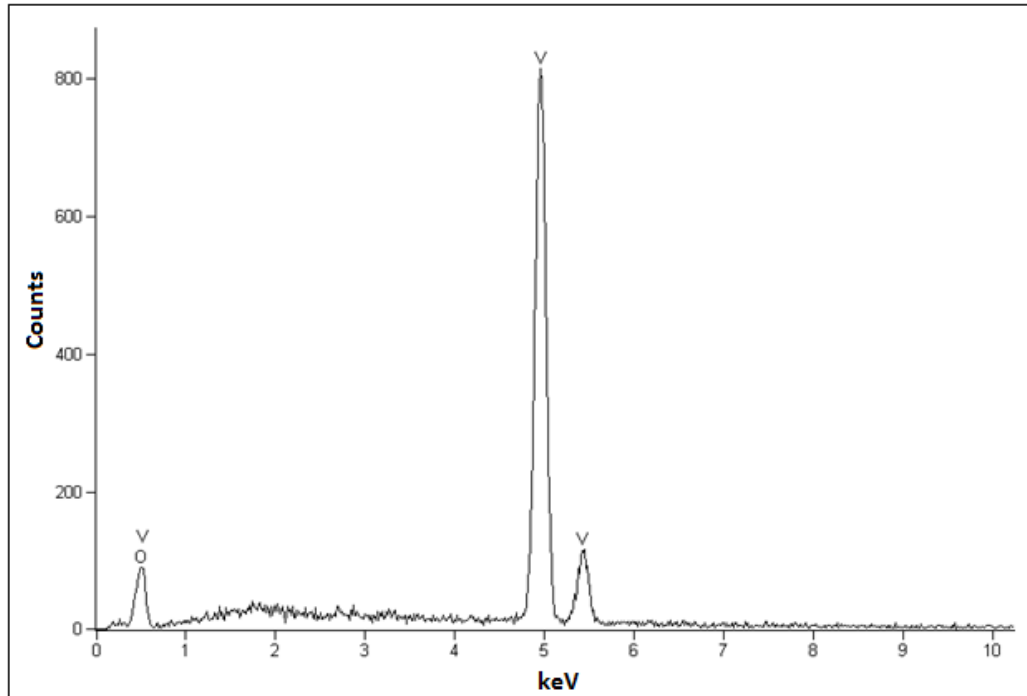


Figure 2.6. The EDX result of hydrated vanadium pentoxide powder.

After the optimization of sol preparation route and material characterization, VO_x thin films were deposited and characterization of them was performed. The details will be given in the following section.

2.2. The Deposition of VO_x Thin Films

In order to prepare VO_x thin film samples, $4''$ Si/SiN_x substrates were cut into $3.5 \times 3.5\text{-cm}^2$ square pieces and cleaned by keeping in acetone, ethanol, and rinsing with deionized (DI) water, respectively. Then, these substrates were deposited with VO_x by utilizing the method of spin coating.

When the brown hydrosol (see Figure 2.1) was directly used as the coating liquid, highly non-uniform thin films were obtained because, the hydrosol formed after dissolution of V powder is heterogeneous and too viscous. Therefore, the second method shown in Figure 2.1 was followed in order to obtain a coating liquid. That is, the hydrosol was dried at 80°C in an oven until a glassy solid material was obtained and then, coating liquid was prepared by

mixing this obtained solid material with given amount of DI water (i.e. 0.1 g of $V_2O_5 \cdot nH_2O$ per 3-6 mL water). However, the problem of forming a homogeneous sol still continued. The sol contained particulates even after magnetically stirring at high rpm values (i.e. 1200-1500 rpm) for long durations. In order to solve that problem, the sol was first kept in a water bath at $80^\circ C$ for 2.5 h [67]. The particulates seemed to get smaller, however, did not completely disappear. Increasing the time would probably help. Nevertheless, instead of heating the sol for longer durations, ultrasonic mixing was tried as a second solution [61]. Finally, sonicating the sol with an ultrasonic probe as shown in Figure 2.7 for a few minutes resulted in obtaining a homogeneous dispersion liquid for obtaining VO_x thin film coating.

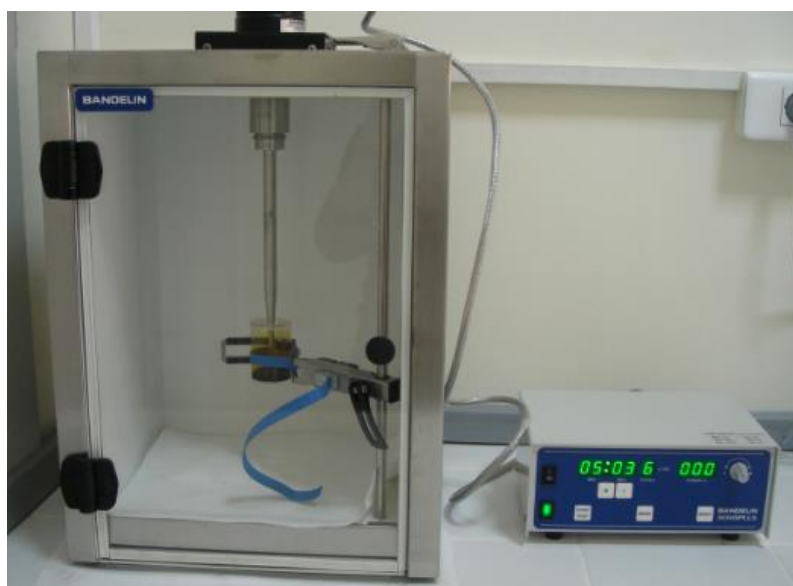


Figure 2.7. The photograph of ultrasonic probe used for homogenizing the coating liquid for VO_x thin deposition.

One or two milliliters of prepared sol were dispensed onto the substrate and then, spin coating was performed at different rpm values ranging between 1000 and 3000 for one minute. Successful coatings could be obtained as shown in Figure 2.8.

After spin coating process, the substrates were dried and sintered at different temperatures for different time durations for various characterizations. The details of characterization of thin films made before and after heat treatment will be given in the next section.

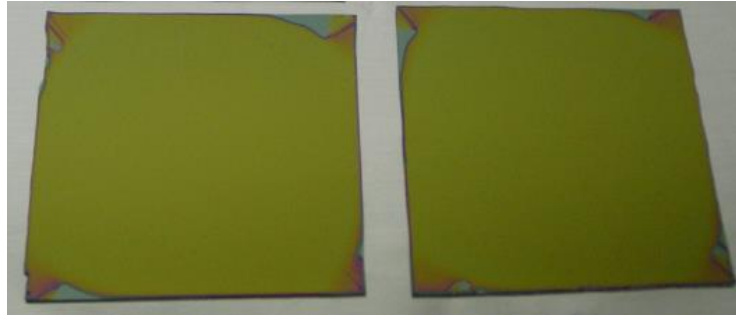


Figure 2.8. The photograph of 3.5x3.5-cm² Si/SiN_x square substrates spin coated with ultrasonically homogenized sol at 2000 rpm for 1 min.

2.3. The Characterization of VO_x Thin Films

Samples were prepared in order to characterize sheet resistance, thickness, resistivity, morphology and phase of VO_x thin films. For this, 4-inch Si/SiN_x wafers were again cut into 3.5x3.5-cm² square pieces and cleaned by keeping in acetone, ethanol, and rinsing with DI water, respectively, as mentioned in the previous section. The coating sol was prepared by ultrasonically mixing 0.1 g V₂O₅.nH₂O (n≤1.8) with per 3 mL DI water and then aging it for 24 hours. Spinning was performed at three different speeds, 1000, 2000, and 3000 rpm, in order to vary film thickness. Before spin coating, circular teflon bands having diameter about 1 cm were pasted at the center of substrates in order to create step height for thickness measurement. They were peeled off after coating. After drying the substrates on a hot plate at 120°C for 1 h, they were sintered at three different temperatures, 200°C, 300°C, and 400°C for 1 h. The heating and cooling rates of furnace were adjusted to 10°C/min.

The sheet resistance (R_s) of thin films was measured from 5 to 8 different regions of substrates with QuadPro four-point probe equipment found in the METU-MEMS facilities. The arithmetic mean of measured R_s values with their standard deviations is given in Table 2.2. Figure 2.9 shows the same data of samples annealed below 400°C in a chart form.

Table 2.2. The sheet resistance of VO_x thin films spin coated at different rpm's and annealed at different temperatures.

	Sheet Resistance (MΩ/square)		
	1000 rpm	2000 rpm	3000 rpm
120°C	1.7 ± 1.0	2.1 ± 0.3	3.2 ± 0.2
200°C	3.2 ± 0.8	3.3 ± 0.9	4.2 ± 0.7
300°C	2.8 ± 0.8	3.2 ± 0.9	3.3 ± 1.4
400°C	29.1 ± 2.0	38.9 ± 6.6	51.6 ± 4.0

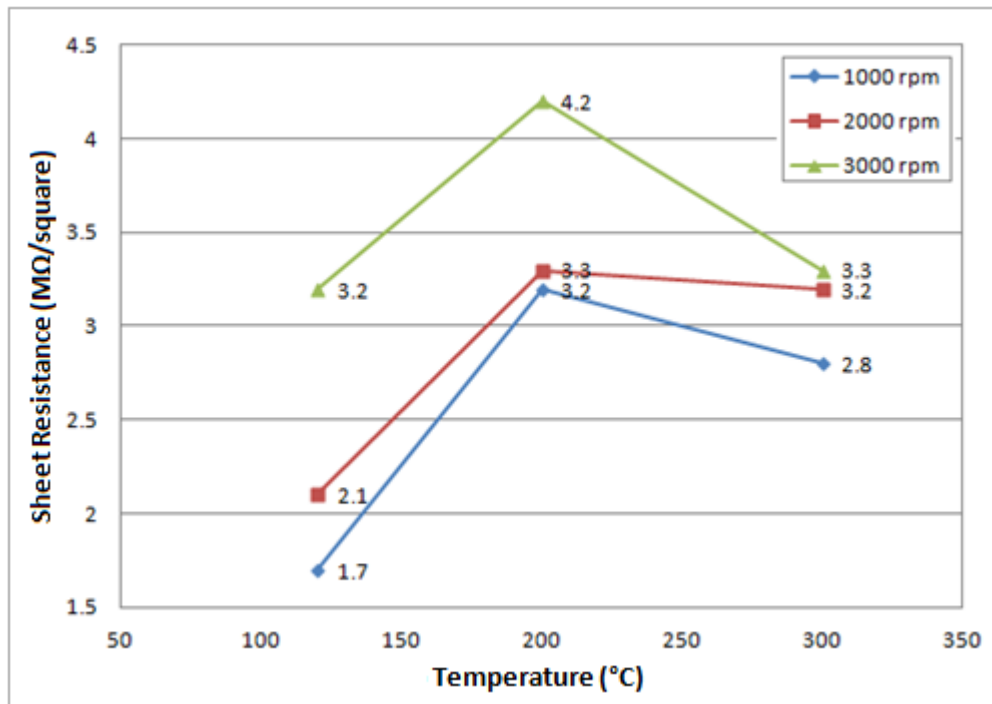


Figure 2.9. The sheet resistance vs temperature plots for VO_x thin films annealed below 400°C.

As it is seen from the values in Table 2.2, sheet resistance increases abruptly when annealing is performed at 400°C. This is an expected result because, the phase of VO_x thin film changes at temperatures above 340°C. That is, the gel form which is V₂O₅.nH₂O turns into polycrystalline V₂O₅ which is also revealed by the XRD data given in Figure 2.10.

The thickness measurement was conducted in DEKTAK 8 Surface Profiler found in the METU-MEMS facilities first. However, no reasonable results could be obtained because, the tip of surface profiler deformed the VO_x thin films, although, the force applied by the tip was decreased to its minimum value. Therefore, JEOL 7500-F Scanning Electron Microscope (SEM) found in the METU-MEMS facilities was utilized for measuring the thickness. Only the thickness of four samples (i.e. spin coated at 2000 rpm) was measured. The cross sectional SEM picture of sample annealed at 120°C is given in Figure 2.11 as an example. The measurement results of others are tabulated in Table 2.3. The resistivity was calculated using the formula of $R_s = \rho/t$ where R_s is sheet resistance, ρ is resistivity, and t is thickness. These results are also given in Table 2.3. The resistivity measurement results also reveal that the resistivity doesn't much differ for the samples annealed at 120°C, 200°C, and 300°C, however, it increases abruptly for the sample annealed at 400°C due to the phase change.

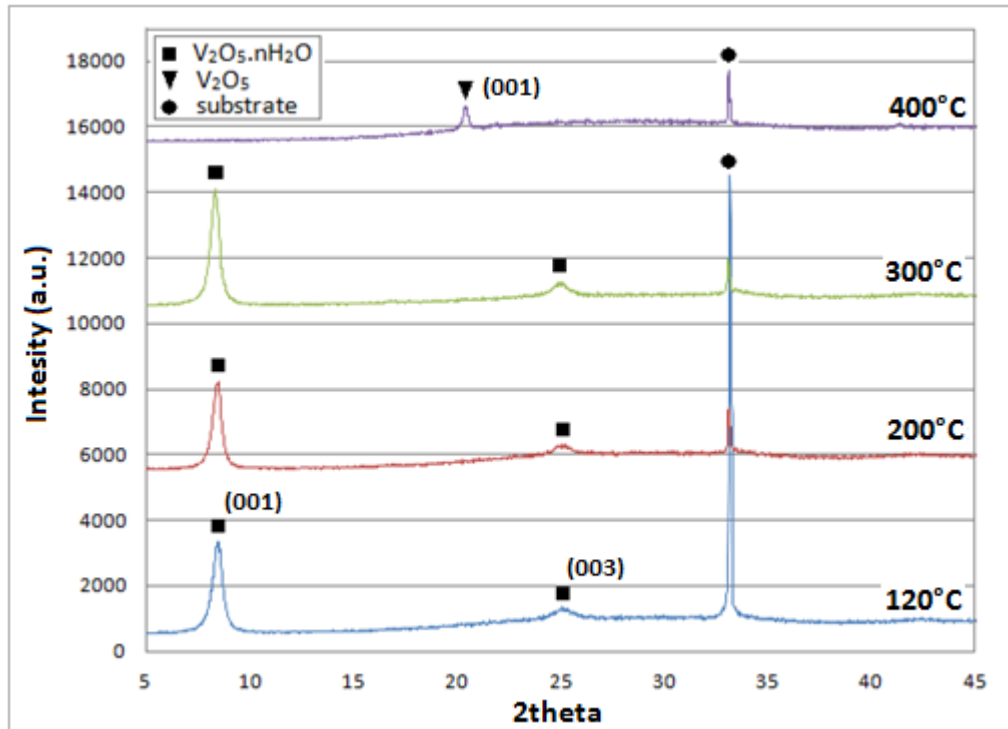


Figure 2.10. The XRD characterization result of VO_x thin films spin coated at 2000 rpm and annealed at 120°C, 200°C, 300°C, and 400°C.

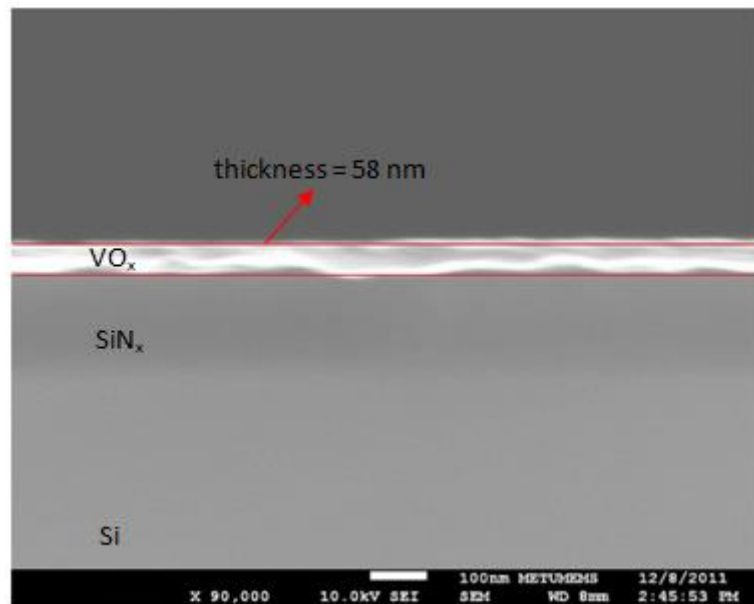


Figure 2.11. The cross sectional SEM picture of sample spin coated at 2000 rpm and annealed at 120°C for thickness measurement.

Table 2.3. The thickness measurement results of VO_x thin films spin coated at 2000 rpm and calculated resistivity values.

Annealing Temperature (°C)	Thickness (nm)	Resistivity (Ω.cm)
120	58	12 ± 2
200	54	18 ± 5
300	49	16 ± 4
400	40	156 ± 26

The surface morphology of samples spin coated at 2000 rpm was observed under Fei Nova Nano SEM 430 FESEM found in METU Metallurgical and Materials Engineering Department. The SEM pictures given in Figure 2.12 were taken after depositing 10-nm Au layer on the samples. As it is seen, the morphology of samples annealed at different temperatures is not much different from each other. The sample annealed at 400°C does not possess a grainy appearance at that SEM magnification although, its phase turned into polycrystalline V₂O₅ which was revealed by XRD.

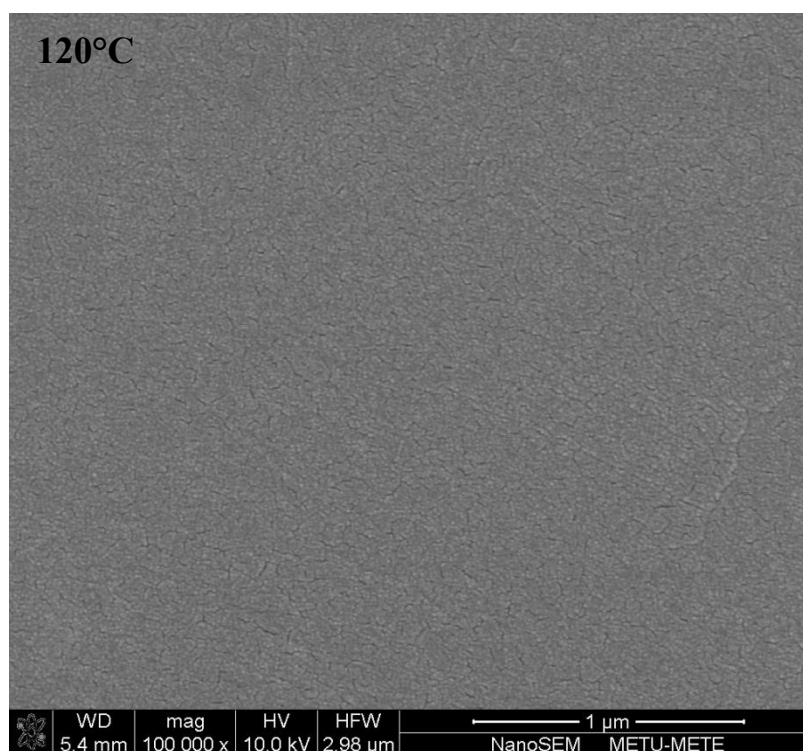


Figure 2.12. The SEM pictures of VO_x thin films spin coated at 2000 rpm and annealed at different temperatures.

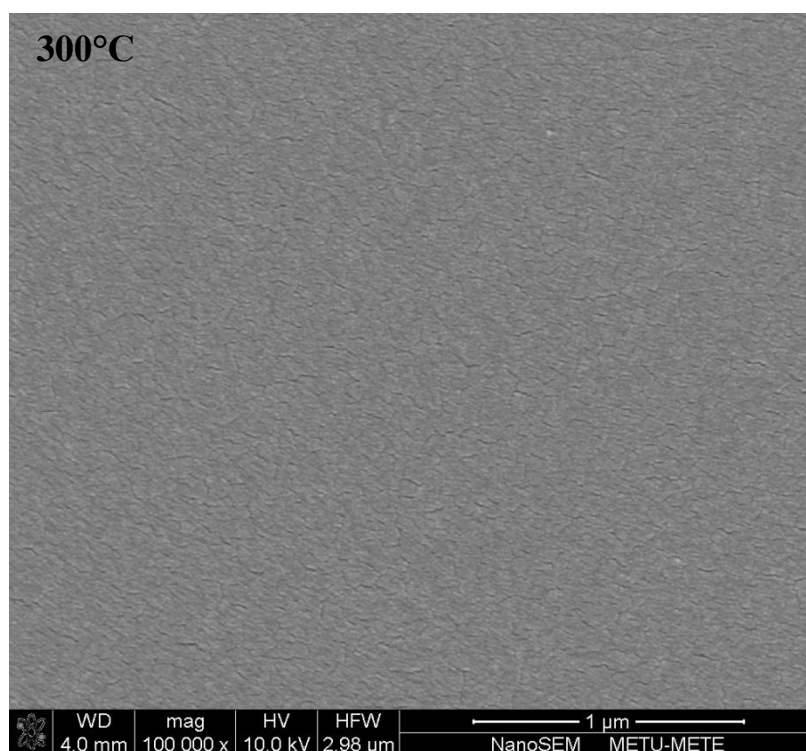
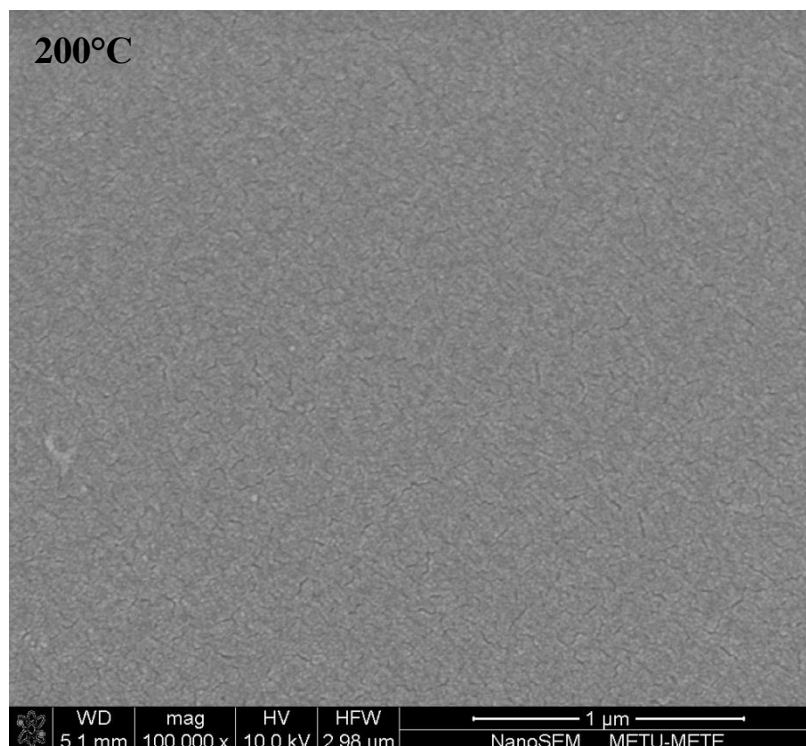


Figure 2.12 (cont'd). The SEM pictures of VO_x thin films spin coated at 2000 rpm and annealed at different temperatures.

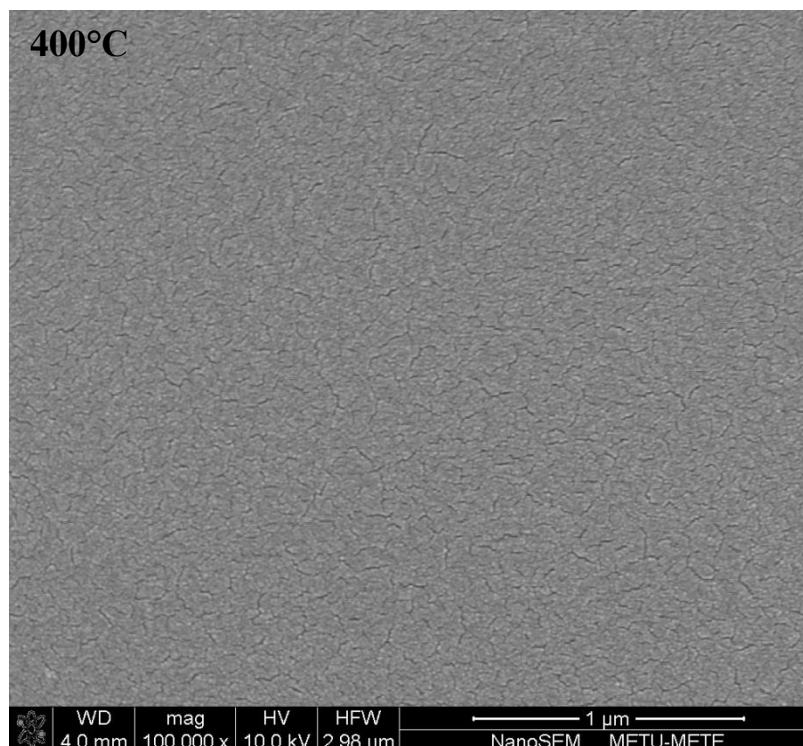


Figure 2.12 (cont'd). The SEM pictures of VO_x thin films spin coated at 2000 rpm and annealed at different temperatures.

After the deposition of VO_x thin films and their characterization, microresistor structures were tried to be fabricated in order to measure the resistance, TCR, and $1/f$ noise of sol-gel deposited VO_x material. The gel form of vanadium pentoxide, which is $\text{V}_2\text{O}_5 \cdot n\text{H}_2\text{O}$ ($n \leq 1.8$), was planned to be used due to its low resistivity. The details of these trials will be given in the following chapter.

2.4. Conclusions

This chapter presented the optimization of sol preparation, VO_x thin film deposition and material characterization. The sol-gel route was optimized as dissolving V powder in 30 wt % H_2O_2 (aq) for 5-6 h at 2°C in a H_2O_2 to V molar ratio of 45. The hydrosol formed after the dissolution reaction was dried at 80°C and a solid material was obtained for material characterization. The characterization results revealed that the solid material is $\text{V}_2\text{O}_5 \cdot n\text{H}_2\text{O}$ ($n \leq 1.8$). A homogenous coating liquid was achieved by mixing this solid material with DI water ultrasonically. Uniform VO_x thin films were prepared on Si/ SiN_x substrates by spin coating and they were heat treated for characterization. The XRD results showed that the thin films have the structure of $\text{V}_2\text{O}_5 \cdot n\text{H}_2\text{O}$ ($n \leq 1.8$) when annealed below 340°C and turn into polycrystalline V_2O_5 when annealed above that temperature. The resistivity of $\text{V}_2\text{O}_5 \cdot n\text{H}_2\text{O}$ thin films were measured to be below $20 \Omega \cdot \text{cm}$ whereas that of V_2O_5 thin film was measured around $150 \Omega \cdot \text{cm}$. Therefore, the gel form of vanadium pentoxide, which is $\text{V}_2\text{O}_5 \cdot n\text{H}_2\text{O}$

($n \leq 1.8$), was decided to be used as the bolometric material in order to be able to obtain 60 k Ω planar type microresistors that can be fit into 35 μm pixel.

CHAPTER 3

MICRORESISTOR FABRICATION AND PERFORMANCE TEST RESULTS

In order to measure the resistance, TCR, and $1/f$ noise of sol-gel deposited VO_x material, microresistors were planned to be fabricated on 4" and 6" Si wafers. Section 3.1 describes the method of TCR and noise measurements and Section 3.2 gives the details of microresistor fabrication and performance test results. Finally, Section 3.3 summarizes the chapter.

3.1. The Description of TCR and Noise Measurements

The TCR measurement is conducted in a Tenney environmental chamber which can control temperature and humidity inside. The picture of alumina substrate used in the TCR measurements is given in Figure 3.1a. A temperature sensor (AD590), which is connected to a DC supply and an ammeter as shown in Figure 3.1b, periodically measures the change in the environment temperature. The output of ammeter directly gives the absolute temperature. The resistor is placed in the middle of alumina substrate and electrical connections from the resistor's pads to the gold lines on the alumina substrate are provided via metal wires. The resistor is connected to a current source and a voltmeter as shown in Figure 3.1c. The voltmeter periodically reads the voltage of resistor biased with a constant current while increasing the temperature of environmental chamber from 15 to 40°C. All received data is sent to a computer and recorded utilizing HP Vee software program. The photograph of TCR measurement set-up is also given in Figure 3.2.

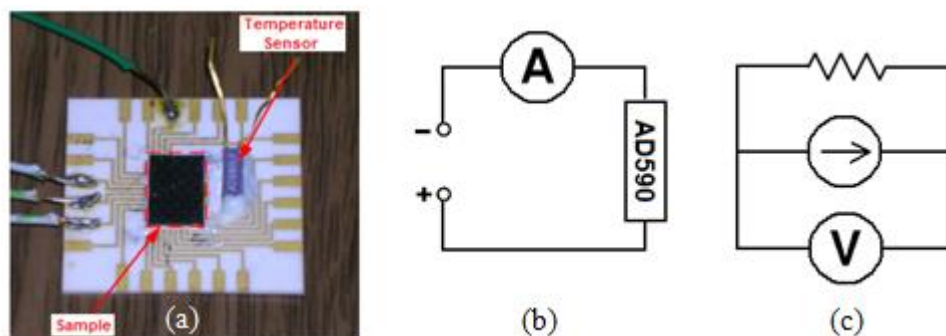


Figure 3.1. (a) The photograph of alumina substrate used in the TCR measurements. The schematic of circuit used for (b) temperature measurement and (c) resistance measurement.

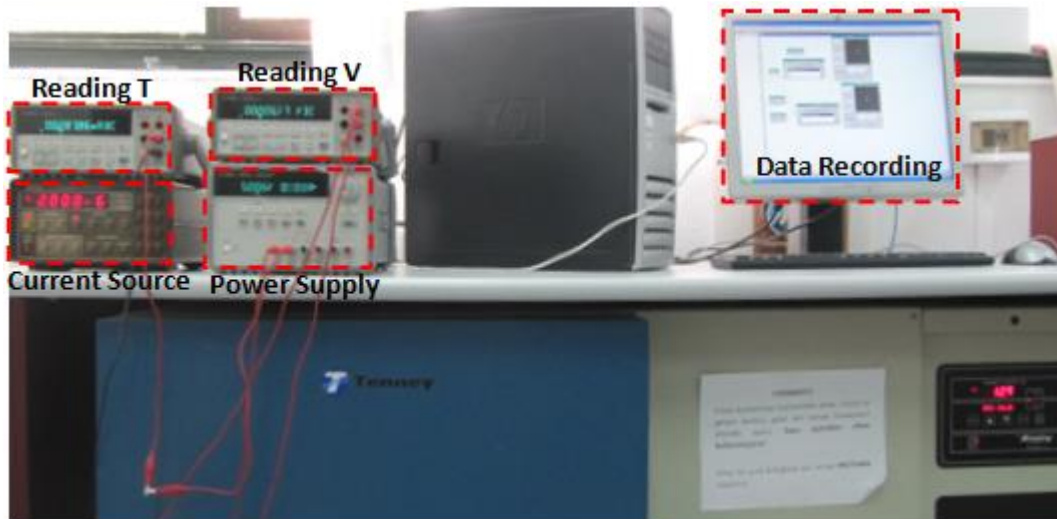


Figure 3.2. The photograph of TCR measurement set-up

After the measurements are taken, the resistance of resistor is simply calculated by dividing the recorded voltage data to the applied bias current. Then, Resistance versus Temperature graph is plotted and a curve is fitted onto it which gives the equation of resistance change with temperature. Taking the derivative of this equation, TCR is simply obtained by using the formula given in Eqn (1.3).

The noise performance of resistors are tested using the circuit of which simplified schematic is given in Figure 3.3 inside a nested Faraday cage as shown in Figure 3.4.

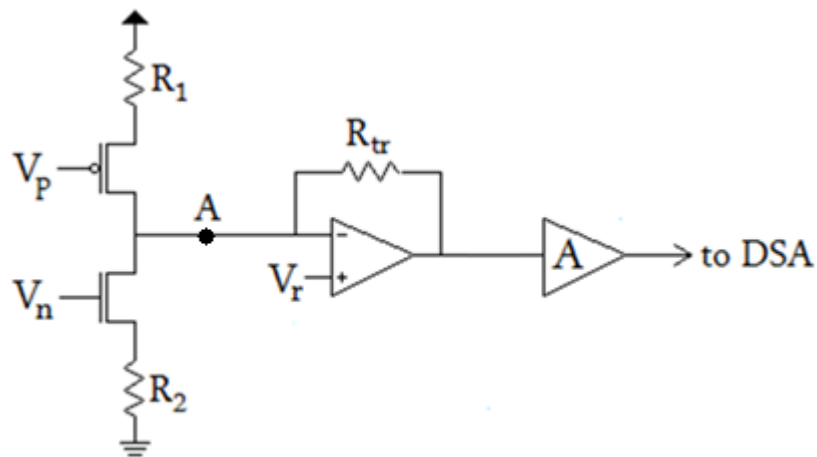


Figure 3.3. The circuit schematic of the noise measurement set-up.

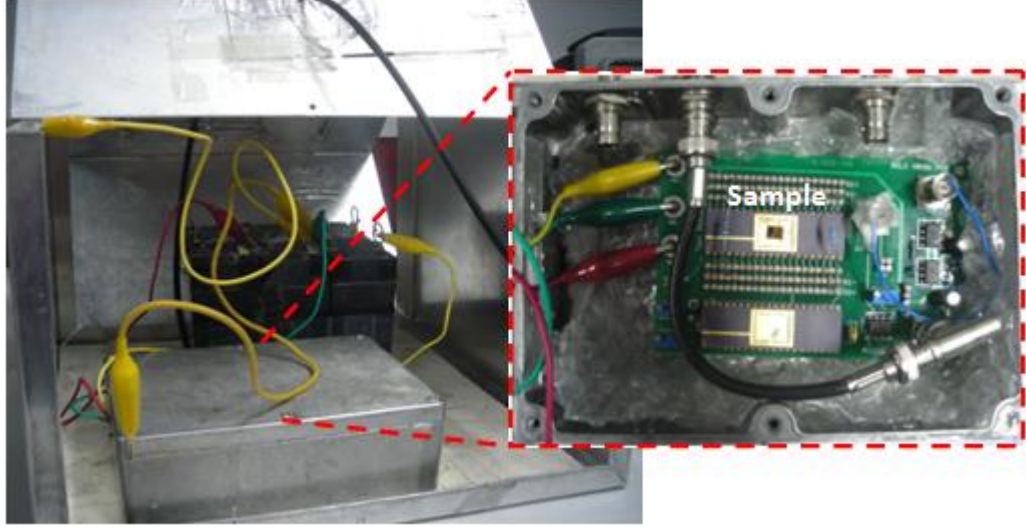


Figure 3.4. The photograph of noise measurement set-up.

The Transimpedance Amplifier (TIA) block in the circuit converts the current to the voltage being sent to a Dynamic Signal Analyzer (DSA) after amplifying a certain amount. The circuit incorporates a pair of resistors, one representing a pixel in the Focal Plane Array (FPA) of a microbolometer and the other one representing the reference pixel used for bias heating cancellation. Both resistors contribute to the total noise. Their resistance should be as similar as possible for proper operation. Differences between them can be compensated by adjusting V_p and V_n of two Field Emission Transistors shown in Figure 3.3.

A noise power spectral density given in Figure 3.5 as an example is obtained after the measurement. In order to determine $C_{1/f}$ parameter given in Eqn (1.21), a curve was fitted onto this power spectral density again as shown in Figure 3.5 by utilizing OriginPro 8 software program. The equation of fitted curve is in the form of:

$$S_I(f) = S_{I,flicker}(f) + S_{I,thermal}(f) = A \frac{1}{f^\beta} + D \quad (3.1)$$

where $S_I(f)$, $S_{I,flicker}(f)$, and $S_{I,thermal}(f)$ are total, flicker, and thermal noise power spectral density having the unit of A^2/Hz , respectively, and f is frequency.

$S_{I,thermal}(f)$ which is D in Eqn (3.1) is a constant and calculated by using Eqn (1.16) as given below:

$$S_{I,thermal}(f) = \frac{4kT\Delta f}{R_1} + \frac{4kT\Delta f}{R_2} \quad (3.2)$$

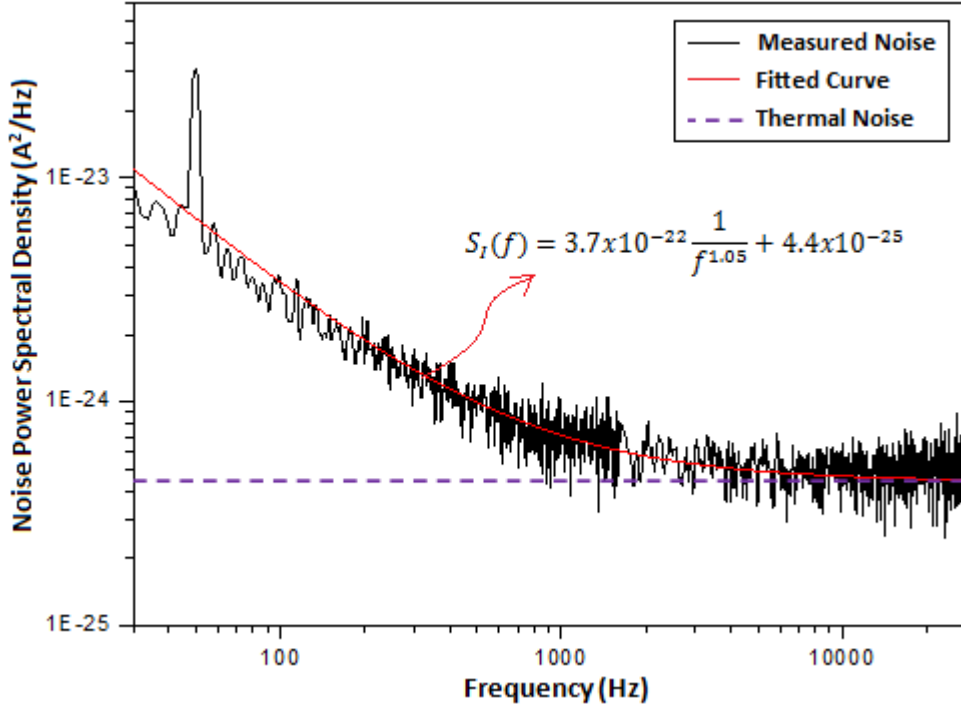


Figure 3.5. The noise power spectral density of a 75 kΩ metal resistor pair obtained under 20 μA bias current and its fitted curve.

Finally, $C_{1/f}$ parameter is simply calculated by using Eqn (1.21) and Eqn (3.1) as follows:

$$S_{I,flicker}(f) = C_{1/f} \frac{I_d^2}{f^\beta} = A \frac{1}{f^\beta} \Rightarrow C_{1/f} = \frac{A}{I_d^2} \quad (3.3)$$

Another quantitative measure for 1/f noise is “corner frequency”, which is the frequency where total noise is equal to two times the noise floor. Consequently, corner frequency (f_c) can be calculated by using Eqn (3.1):

$$S_I(f) = 2 \times S_{I,thermal}(f) = A \frac{1}{f_c^\beta} + D \quad (3.4)$$

$$\Rightarrow S_I(f) = 2 \times S_{I,thermal}(f) = A \frac{1}{f_c^\beta} + S_{I,thermal}(f) \quad (3.5)$$

$$\Rightarrow f_c = \left(\frac{A}{I_d^2} \right)^{(1/\beta)} \quad (3.6)$$

The lower the corner frequency is, the better the noise performance is. It should also be kept in mind that f_c is dependent on measuring conditions such as bias current or voltage on the contrary to $C_{1/f}$ parameter. As bias current or voltage decreases, the corner frequency also

decreases. Therefore, in order to make comparison between two different obtained f_c values, the bias current applied during the measurements should be the same.

3.2. The Fabrication of Microresistors and Their Performance Test Results

As mentioned before, microresistors were planned to be fabricated on 4" and 6" Si wafers for performance tests. Figure 3.6 and Figure 3.7 illustrate the top and perspective view of standard and finger type planar electrodes that would be utilized in the resistor formation, respectively. The distance between the electrodes in the figures determines the length of resistor (L), while the total length of fingers determines the width of resistor (W). The IR active material, VO_x , is deposited between and onto the electrodes. In order to have low resistance value, W/L ratio of the detector should be made as large as possible

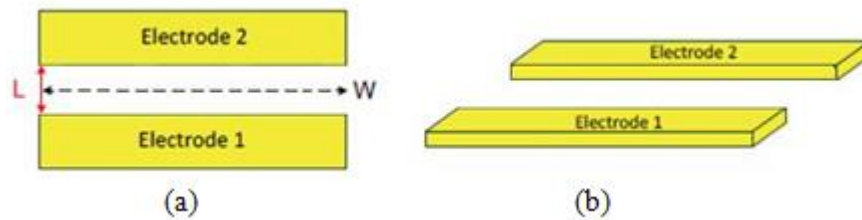


Figure 3.6. The (a) top and (b) perspective view of standard type planar electrodes.

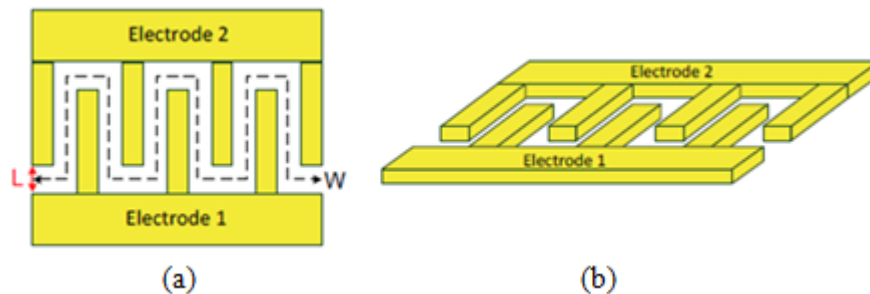


Figure 3.7. The (a) top and (b) perspective view of finger type planar electrodes.

The resistor formation process flow followed in both METU-MEMS facilities and METU Metallurgical and Materials Engineering Department is simply illustrated in Figure 3.8. First, an insulator layer, SiN_x , is deposited on a 4" or 6" Si wafer by Plasma Enhanced Chemical Vapor Deposition (PECVD). Then, the electrode metal (i.e. gold) with an underlying adhesion promoter metal layer (i.e. titanium or chromium) is deposited by sputtering and patterned by photolithography. Finally, vanadium oxide layer is deposited by sol-gel method and again patterned by photolithography.

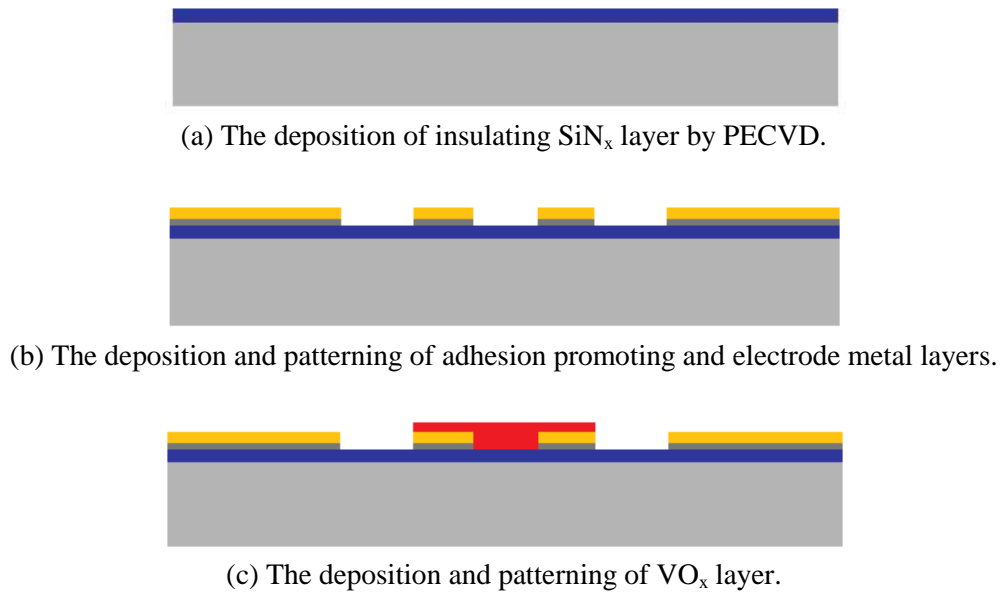


Figure 3.8. The representative cross sectional views of resistor formation steps.

The etching of metal layers (i.e. Au, Ti, and Cr) has already been optimized in the context of previous thesis studies conducted in the METU-MEMS facilities [6,18], however, the etching of VO_x layer is a new concern. Wet or dry etching could be performed. The former one was decided to be tried at first. Therefore, the relevant handbooks [68,69] and literature [70] about VO_x (especially for V₂O₅ phase) wet etching were searched and it was seen that acidic and basic solutions could be used. V₂O₅ is also soluble in H₂O₂ (aq), thus, it could be another alternative etchant.

The first VO_x resistor fabrication run was performed on a 4" Si wafer following the process steps in Figure 3.8, however, a problem was encountered during the photolithography for VO_x patterning. That is, the developer solution used for photoresist patterning severely degraded the VO_x layer. In fact, this is a problem which was also encountered by other groups studying VO_x thin film deposition in literature. They solved such a problem by depositing a very thin passivation SiN_x layer before photolithography [71]. Therefore, a second fabrication run of which sol-gel VO_x deposition details are given in Table 3.1 was performed again on a 4" Si wafer. However, this time, 0.2 μm SiN_x layer was deposited onto the VO_x layer prior to photolithography in order to protect it from the photolithography chemicals. It was seen that 0.2 μm SiN_x sufficed for protecting the VO_x layer and the photoresist could be patterned successfully without damaging the VO_x layer as shown in Figure 3.9.

Table 3.1. The sol-gel VO_x deposition details of second microresistor fabrication run.

Sol	0.1 g of V ₂ O ₅ .nH ₂ O / 4 mL DI water
Spin Speed	Step 1 → 500 rpm for 7 sec Step 2 → 2000 rpm for 1 min
Drying	at 120°C for 1 h
Annealing	at 300°C for 1 h (heating rate was 5°C / min)

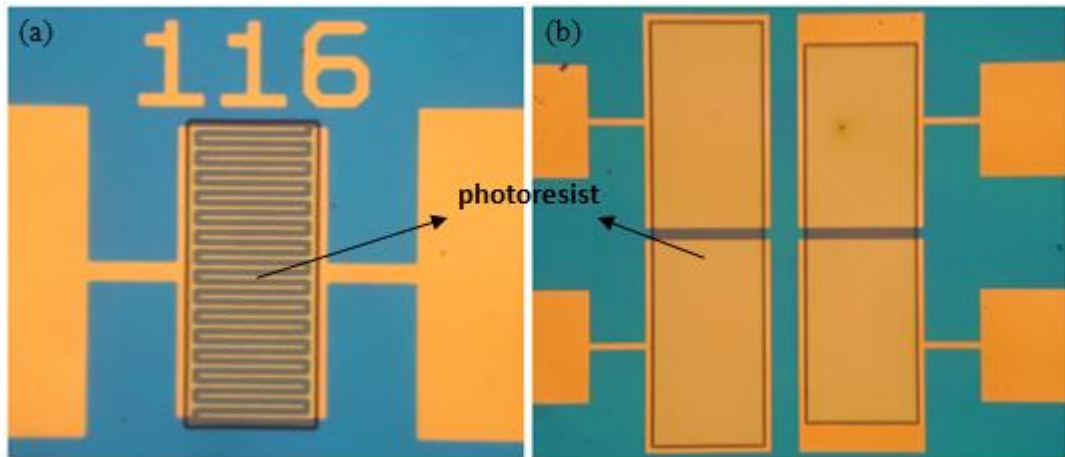


Figure 3.9. The photographs of VO_x resistors after photolithography. 0.2 μm SiN_x layer was deposited on VO_x by PECVD in order to protect it from the photolithography chemicals.

After photolithography, the top SiN_x layer used for VO_x passivation was etched by reactive ion etching (RIE). Then, the wafer was cut into pieces and some of the dies were used in the optimization of VO_x layer wet etching with H₂O₂ (aq). After trying different H₂O₂ (aq) concentrations, the etchant was finally determined as a mixture of DI water and 30 wt % H₂O₂ in a volume ratio of 20:1 (H₂O:H₂O₂) and the etching duration was optimized as 10-30 sec.

Figure 3.10 shows the layout of a 4” wafer in which the numbered dies include planar type resistors with and without fingers having different W/L ratios (Figure 3.6). The resistance value of same type of resistors from at least 5 different dies (each die also includes three resistors having the same type) was measured by utilizing a probe station and a multimeter after VO_x etching and then, the average of these measurements was calculated together with its standard deviation. Therefore, the resistance value given with its standard deviation for a certain type of resistor will refer to the average of several measurement results hereafter.

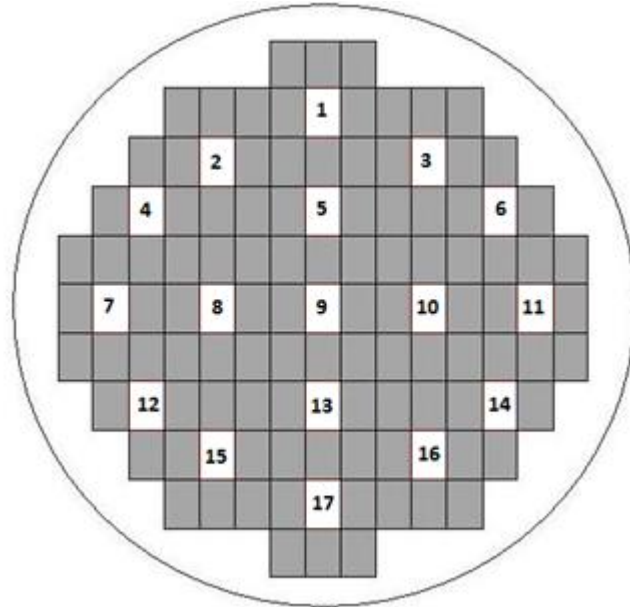


Figure 3.10. The representation of a 4" wafer showing the location of dies including the microresistor structures by numbering.

The resistance of finger type microresistors (Figure 3.9a) having the largest W/L ratio (i.e. 716) was measured to be $61.5 \pm 7.2 \text{ k}\Omega$. The resistance of standard type microresistors (Figure 3.9b) having the largest W/L ratio (i.e. 47) was measured to be $135.6 \pm 16.3 \text{ k}\Omega$. As it is seen, the resistance of finger type resistors having a W/L ratio of 716 is low enough to be compatible with the ROIC, however, the goal is to reach below $100 \text{ k}\Omega$ resistance (as explained in Section 1.5) for the finger type resistors having a W/L ratio roughly lower than 100 in order to be able to fit its contact electrodes into a $35 \mu\text{m}$ pixel pitch.

The TCR of a $55 \text{ k}\Omega$ finger type resistor and a $180 \text{ k}\Omega$ standard type resistor were measured under $10 \mu\text{A}$ bias current following the procedure described in Section 3.1. The Resistance and TCR versus Temperature graphs of finger and standard type resistors are given in Figure 3.11 and Figure 3.12, respectively. As a result, the TCR of finger and standard type resistors were measured to be $-1.8 \text{ } \%/^{\circ}\text{C}$ and $-1.7 \text{ } \%/^{\circ}\text{C}$ at 25°C , respectively, which are comparable values with literature (Table 1.2). Another good result is that the TCR is not changing with temperature very much.

As a next step, the flicker noise performance of VO_x resistors was tested but, before the VO_x resistors, the noise of a $95 \text{ k}\Omega$ metal resistor under $10 \mu\text{A}$ current was measured in order to check the reliability of noise measurement set-up. After obtaining its noise power spectral density, the $1/f$ noise parameter, $C_{1/f}$, and corner frequency, f_c , were obtained as described in Section 3.1 and are given in Table 3.2.

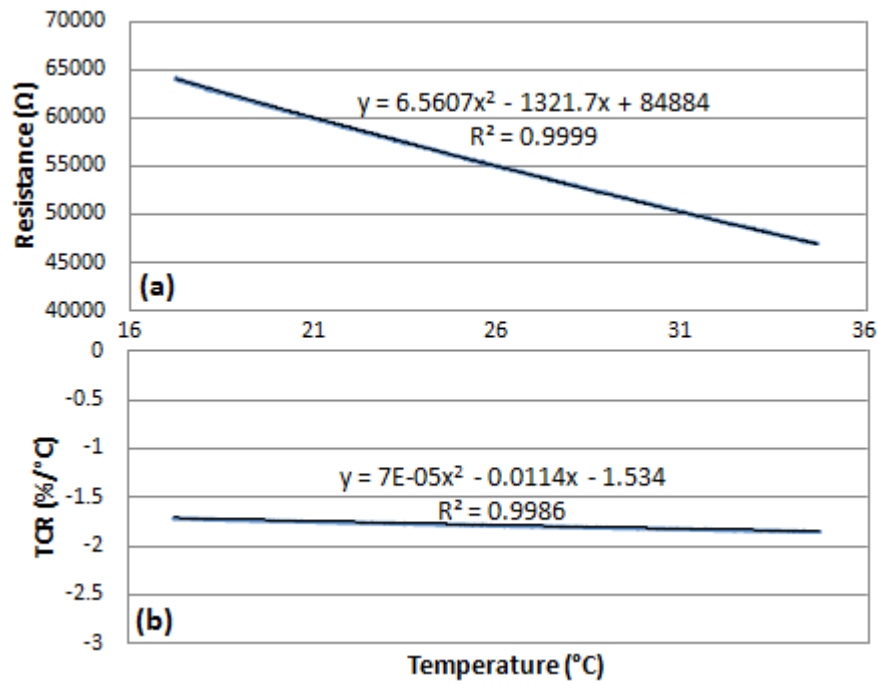


Figure 3.11. The (a) resistance and (b) TCR vs temperature graph of a 55 kΩ finger type VO_x resistor under 10 μA bias current. The TCR at 25°C is -1.8 %/°C.

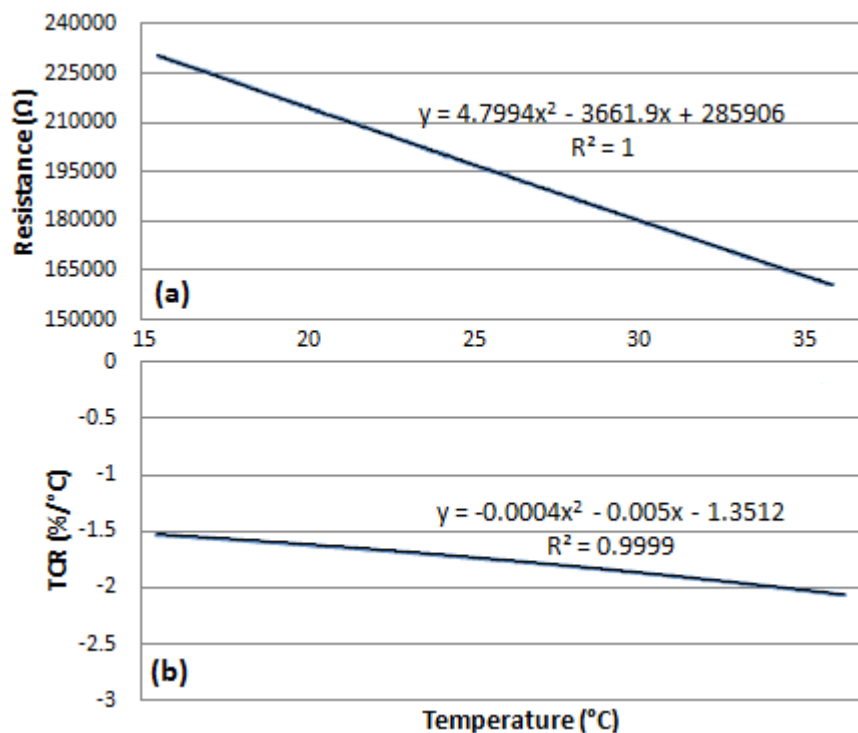


Figure 3.12. The (a) resistance and (b) TCR vs temperature graph of a 180 kΩ standard type VO_x resistor under 10 μA bias current. The TCR at 25°C is -1.7 %/°C.

Table 3.2. The noise measurement results of metal and different VO_x resistor pairs under different bias current.

Resistor	Resistance (kΩ)	Thermal Noise (A ² /Hz)	Bias Current (μA)	β	C _{1/f} parameter	f _c (kHz)
Metal	95	3.4x10 ⁻²⁵	10	1.05	5.3x10 ⁻¹²	1.1
Standard type VO _x	130	2.6x10 ⁻²⁵	14	1.08	1.3x10 ⁻¹⁰	42.6
			9	1.05	1.3x10 ⁻¹⁰	24.9
Standard type VO _x	145	2.3x10 ⁻²⁵	13	1.10	2.6x10 ⁻¹⁰	63.7
			10	1.08	2.6x10 ⁻¹⁰	48.1
Finger type VO _x	65	5.1x10 ⁻²⁵	10	1.05	5.5x10 ⁻¹⁰	62.1
			20	1.05	5.2x10 ⁻¹⁰	220.4
			30	1.05	5.6x10 ⁻¹⁰	512.1
Finger type VO _x	75	4.4x10 ⁻²⁵	10	1.05	3.6x10 ⁻¹⁰	47.5
			20	1.05	4.0x10 ⁻¹⁰	196.8
			27	1.05	4.2x10 ⁻¹⁰	365.1

The results given in Table 3.2 are higher than expected for a metal resistor pair. In fact, it is expected that C_{1/f} parameter and f_c should be below 1.0x10⁻¹² and 0.6 kHz, respectively. This discrepancy indicates that there is an additional noise source in the measurement set-up. Because, the additional noise source would be added to the all measurement results in the same amount, the noise of different VO_x resistor pairs was measured in any case under different bias current in spite of the existence of additional noise source in order to investigate whether the measured C_{1/f} parameters are independent of measuring conditions or not (as mentioned in Section 1.5) which is bias current in our case. The noise measurement results of these VO_x resistor pairs are also summarized in Table 3.2 and the results given in the table verify this indicated argument.

The I-V curves of VO_x resistors were also checked by utilizing a current source and a multimeter. The I-V curves of one standard type and one finger type resistor are given in Figure 3.13 and Figure 3.14, respectively. The I-V curves of others were observed to have the same trend, therefore, they are not given here for saving space. The non-linear behavior both in Figure 3.13 and Figure 3.14 might be an indication of poor electrical contacts which might be due to insufficient etching of VO_x layer on the gold pads.

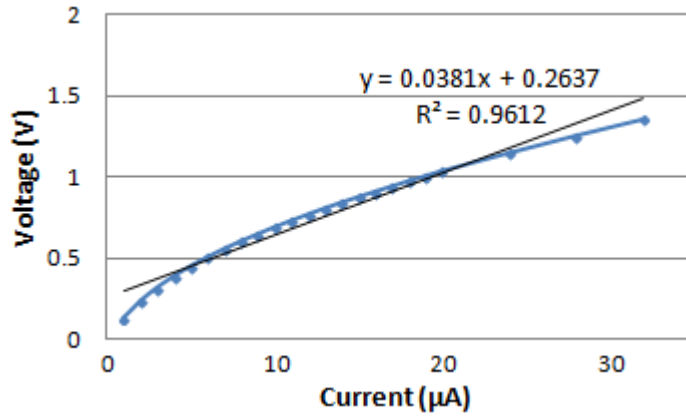


Figure 3.13. The I-V curve of one finger type VO_x resistor.

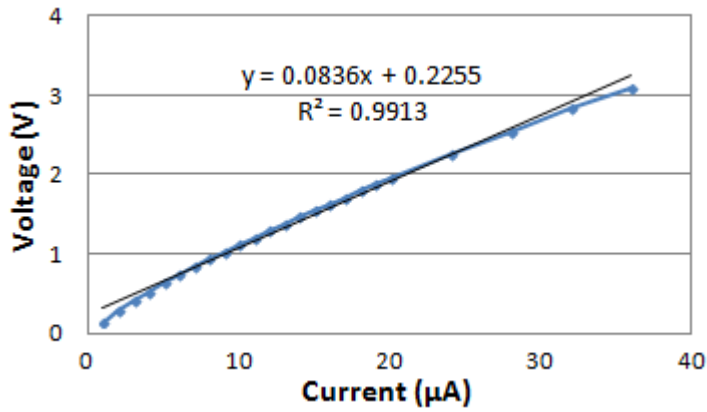


Figure 3.14. The I-V curve of one standard type VO_x resistor.

In order to investigate whether the electrical contacts between the Au pads and the ball of wire bonding are poor due to insufficient etching of VO_x layer on the Au pads, the EDX of Au pads was taken and is given in Figure 3.15. As it is seen, some amount of vanadium is still remaining on the pads which might lead to the poor electrical contacts, thus, increase in 1/f noise.

After the noise measurements mentioned above were conducted, an improvement in the noise measurement set-up was made by connecting a bypass capacitor in parallel with the power supply of the circuit (Figure 3.3) in order to make the circuit's operation more stable (the improvement was made by Burak Eminoğlu). It was expected that this change would be reflected in the measured noise value. Therefore, the set-up was first checked by measuring the noise of a 75 kΩ metal resistor pair under 20 µA bias current and then, the noise of a 180 kΩ standard type VO_x resistor pair was measured. Table 3.3 gives the obtained results.

As it is seen, the noise of metal resistor is as expected and the $C_{1/f}$ parameter of VO_x resistor calculated as 4.7×10^{-11} is lower than the values given in Table 3.2.

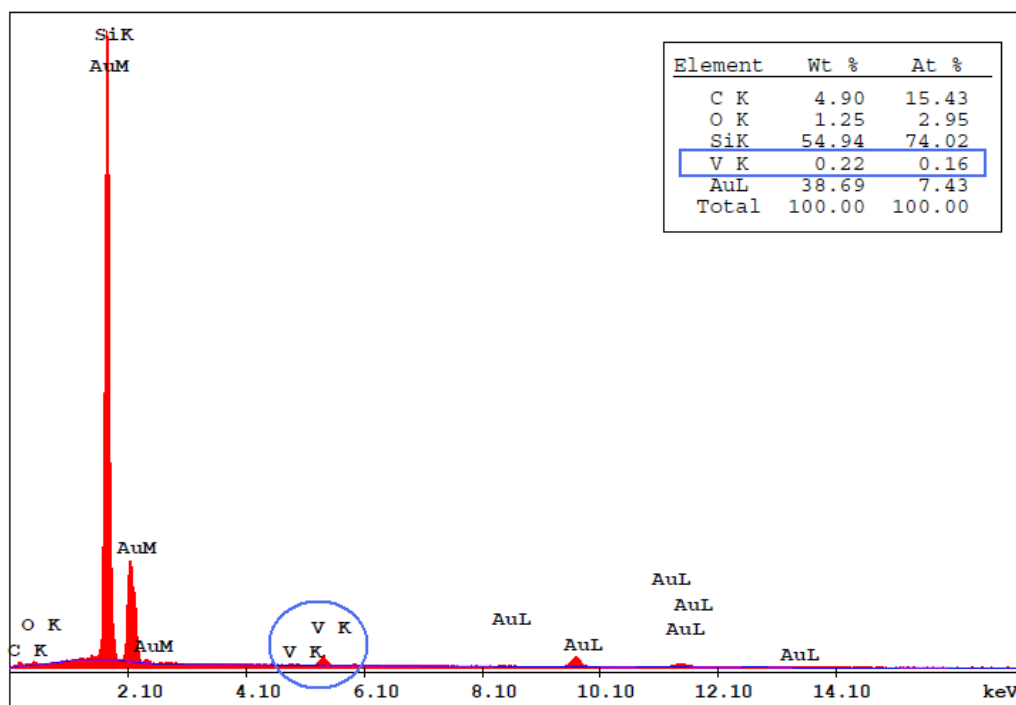


Figure 3.15. The EDX spectrum of the Au pads of a VO_x resistor of which VO_x layer was etched by using H_2O_2 (aq). The etchant was a mixture of DI water and 30 wt % H_2O_2 in a volume ratio of 20:1 ($H_2O:H_2O_2$) and etching duration was 10-30 sec.

Table 3.3. The noise measurement results of metal and VO_x resistor pairs after an improvement in the noise measurement set-up was made.

Resistor	Resistance (k Ω)	Thermal Noise (A ² /Hz)	Bias Current (μ A)	β	$C_{1/f}$ parameter	f_c (kHz)
Metal	75	4.4×10^{-25}	20	1.05	9.3×10^{-13}	0.6
Standard type VO_x	180	1.8×10^{-24}	10	1.10	4.7×10^{-11}	1.2

In order to maintain lower resistance values, another resistor formation trial was performed with thicker $V_2O_5 \cdot nH_2O$ thin film. The details of sol-gel VO_x deposition of this third resistor

fabrication run is given in Table 3.4. Different than the previous one, the water amount of sol was decreased from 4 mL to 2 mL per 0.1 g $V_2O_5 \cdot nH_2O$.

Table 3.4. The sol-gel VO_x deposition details of third microresistor fabrication run.

Sol	0.1 g of $V_2O_5 \cdot nH_2O$ / 2 mL DI water
Spin Speed	Step 1 → 500 rpm for 7 sec Step 2 → 2000 rpm for 1 min
Drying	at 120°C for 1 h
Annealing	at 300°C for 1 h (heating rate was 5°C / min)

As it is known, the final step of resistor fabrication is etching of VO_x layer. Therefore, the wafer was again cut into pieces for wet etching trials. At first, 1.6 wt % H_2O_2 (aq) was tried, however, a problem was encountered. That is, when the VO_x layer got thicker, the etchant solution penetrated between the VO_x thin film and substrate and then, lifted off the VO_x layer residing on the electrodes also. The weight percentage of H_2O_2 was gradually increased upto 30 in the following etching trials, however, the problem still continued. Some acidic and basic solutions listed below were also tried other than H_2O_2 (aq), nevertheless, they did not solve the problem:

- 1) 5 wt % HCl (aq)
- 2) 1 wt % HCl (aq)
- 3) 0.8 wt % NaOH (aq)
- 4) 100 g of **0.50** wt % NaOH (aq) + 1 mL of 30 wt % H_2O_2 (aq)
- 5) 100 g of **0.33** wt % NaOH (aq) + 1 mL of 30 wt % H_2O_2 (aq)
- 6) 100 g of **0.20** wt % NaOH (aq) + 1 mL of 30 wt % H_2O_2 (aq)
- 7) 100 g of **0.05** wt % NaOH (aq) + 1 mL of 30 wt % H_2O_2 (aq)

Because wet etching became problematic, it was decided to try dry etching. For this, cut wafer pieces are pasted onto 4" or 6" wafers with a special compound which is thermally conductive. As a first trial, a gas mixture of Ar and Cl_2 was applied in the metal reactive ion etching (MRIE) equipment for upto 1.5 min. However, this gas mixture is not selective to gold; therefore, Au pads were also etched away as shown in Figure 3.16.

It was seen in literature that CF_4 , which is selective to gold, could be used for VO_x etching [71], therefore, a gas mixture of CF_4 and O_2 was tried in the RIE equipment as the second dry etchant. The process parameters used as the starting point are given in Table 3.5.

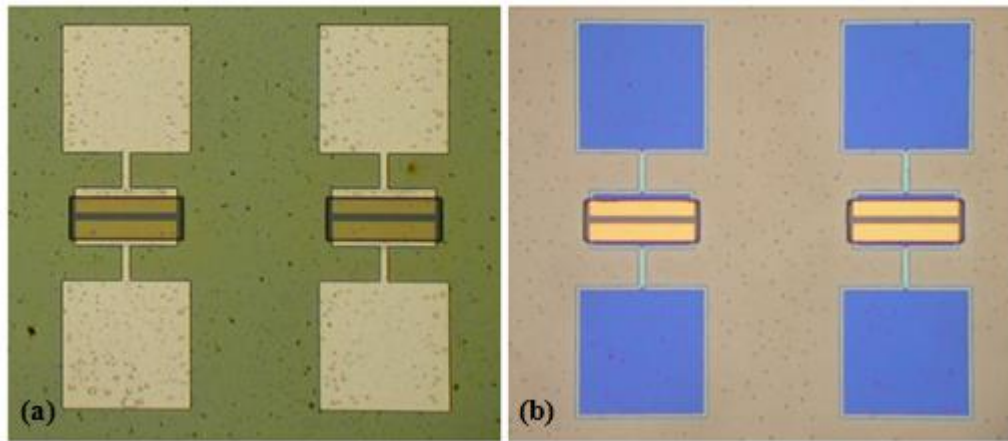


Figure 3.16. The photographs of VO_x resistors after dry etching the VO_x layer with a gas mixture of Cl₂ and Ar in MRIE equipment for (a) 50 sec and (b) 1.5 min.

It was seen this gas mixture etches the VO_x layer successfully without damaging the Au pads, however, is unfortunately not selective to the SiN_x layer underneath the Au pads used for isolating the resistors from the Si substrate as shown in Figure 3.17. The resistance and TCR could still be measured, however, the absence of an insulating layer (i.e. SiN_x) created problem while measuring 1/f noise. That is, the wire bonding also touches to Si substrate besides the Au pads as represented in Figure 3.18 and because, Si substrate has also its own electrical conductivity, this leads to fluctuations in the current passing through the VO_x resistors and therefore, instability problem in the noise measurement circuit. Therefore, the flicker noise of these VO_x resistors couldn't be measured.

Table 3.5. The process parameters used as the starting point for VO_x dry etching with a gas mixture CF₄ and O₂.

CF₄ : O₂ Flow Rate	60 sccm : 10 sccm
Power	225 W
Pressure	40 mTorr
Etching Duration	2 min

The measured resistance values of various VO_x resistors having different W/L ratios are given in Table 3.6. As it is seen, the resistances were decreased to low enough values which even do not require the utilization of finger type electrodes. The TCR of a 6 kΩ standard type resistor measured under 10 μA bias current was found to be -1.7 %/°C at 25°C. Figure 3.19 gives the obtained resistance and TCR vs temperature plots of this measurement.

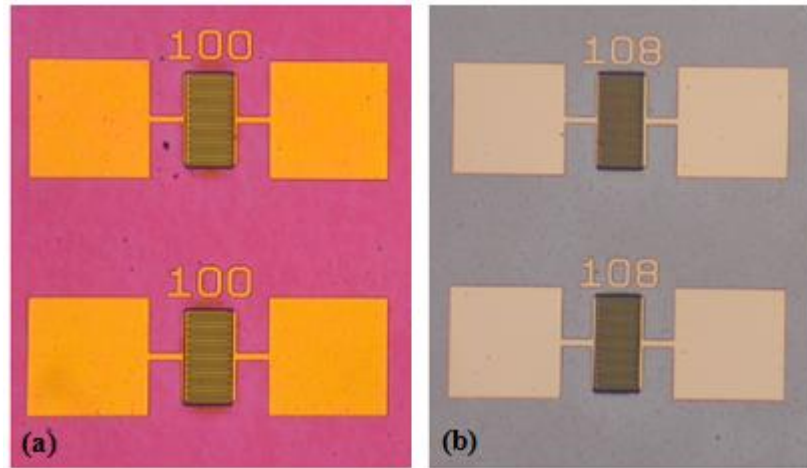


Figure 3.17. The photographs of VO_x resistors (a) before and (b) after VO_x dry etching with CF₄ and O₂ gas mixture in the RIE equipment for 2 min.

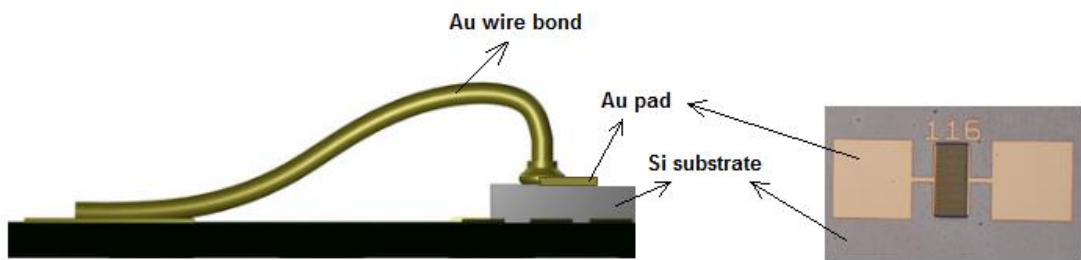


Figure 3.18. The representation of a VO_x resistor of which wire bonding is performed in order to make 1/f noise test.

Table 3.6. The measured resistance values of VO_x resistors whose VO_x layer was deposited thicker and dry etched by using CF₄ in the RIE equipment.

Type of the Resistor	W/L Ratio	Resistance
Standard	18	10.8 ± 1.0 kΩ
Finger	52	13.4 ± 1.4 kΩ
Finger	75	5.4 ± 1.3 kΩ
Finger	716	0.7 ± 0.1 kΩ

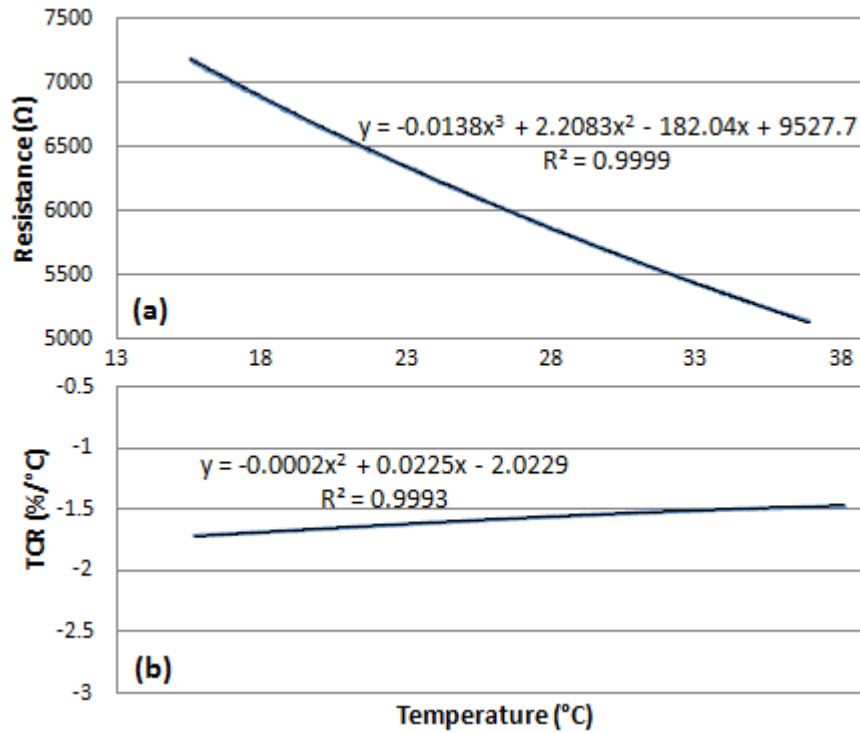


Figure 3.19. The (a) resistance and (b) TCR vs temperature plot of a 6 kΩ standard type VO_x resistor whose VO_x layer was deposited thicker and dry etched by using CF₄ in the RIE equipment. The bias current was 10 μA. The TCR at 25°C is -1.7 %/°C.

The I-V curve of VO_x resistor used in the TCR measurement was also obtained by utilizing a current source and a multimeter and given in Figure 3.20. It is seen that the resistor is ohmic.

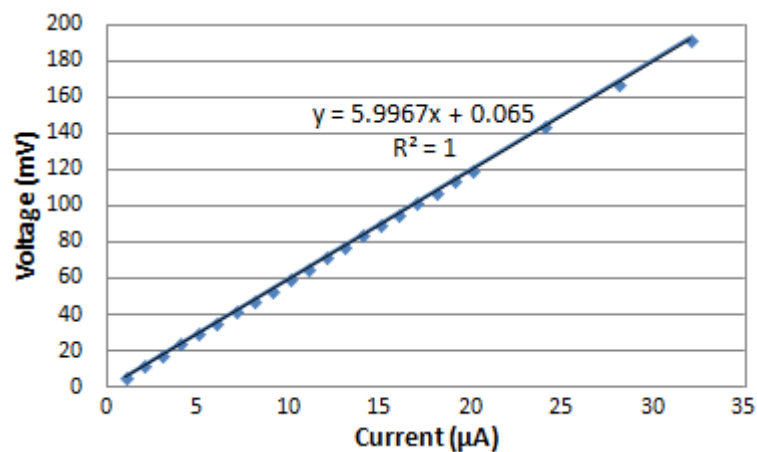


Figure 3.20. The I-V curve of a standard type VO_x resistor whose VO_x layer was deposited thicker and dry etched by using CF₄ in the RIE equipment.

The EDX characterization of Au pads was also performed after dry etching with CF_4 and Figure 3.21 gives the obtained spectrum. As it is seen, there is no vanadium oxide remaining on the metal pads which also explains why a linear I-V plot given in Figure 3.20 was obtained this time. That is, the etching of VO_x layer on the Au pads seems to be successful providing the electrical contacts to be in good quality. However, as mentioned before, the selectivity of etching recipe to SiN_x should be optimized which could be realized by changing the plasma power or gas flow rate indicated in Table 3.5.

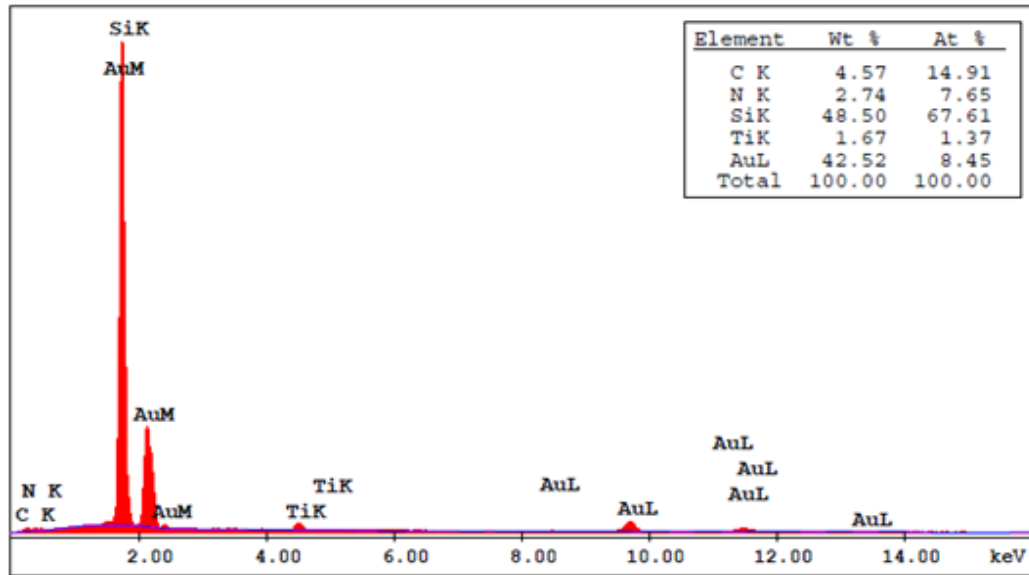


Figure 3.21. The EDX spectrum of Au pads of a VO_x resistor of which VO_x layer was dry etched by using CF_4 in the RIE equipment.

Before optimizing the VO_x dry etching with CF_4 , it was decided to use glass wafers instead of Si substrates in order to be able to measure the $1/f$ noise of VO_x resistors. Consequently, new microresistors were fabricated on a 4" glass wafer. The details of sol-gel VO_x deposition step are given in Table 3.7.

Table 3.7. The sol-gel VO_x deposition details of fourth microresistor fabrication run which was on a 4" glass wafer.

Sol	0.1 g of $\text{V}_2\text{O}_5 \cdot n\text{H}_2\text{O}$ / 3 mL DI water
Spin Speed	Step 1 → 500 rpm for 7 sec Step 2 → 3000 rpm for 1 min
Annealing	at 250°C for 20 min (heating rate was 10°C / min)

Different than the previous fabrication run, the water amount for sol preparation was increased from 2 mL to 3 mL in order to increase the resistance because, the noise measurement set-up had been designed for measuring the noise of resistors having resistance higher than 40 k Ω . When the resistance is lower than this value, the noise of transistors increases, hence, brings additional noise source in the overall noise power spectral density [72]. Moreover, the drying step was eliminated and the annealing temperature and time were decreased from 300C to 250°C and 1 h to 20 min, respectively.

After RIE of SiN_x (i.e. the passivation layer), the wafer was cut into pieces and some of them were pasted onto 6” wafers for VO_x dry etching. The VO_x layer was etched in the RIE equipment by using the same process parameters given in Table 3.5. Only the etching duration was kept as 2.5 min.

The resistance of standard type resistors having a W/L ratio of 47 and 23.5 was measured to be 31.5 ± 5.2 and 51.0 ± 5.6 k Ω , respectively. The 1/f noise performance of three different standard type VO_x resistor pairs was tested under 20 μ A bias current after, checking the reliability of measurement set-up by testing a 60 k Ω metal resistor pair again under 20 μ A bias current. All results are summarized in Table 3.8. As it is seen, the noise of metal resistor pair was measured to be higher than expected (The expected values: $C_{1/f} < 1.0 \times 10^{-12}$ and $f_c < 0.6$ kHz). Therefore, the noise performance of VO_x resistors should be evaluated taking this into consideration. Nevertheless, the $C_{1/f}$ values given in Table 3.8 are lower than those of given in Table 3.3. This could be attributed to the increased quality of electrical contacts by complete etching of VO_x layer residing on the Au pads.

Table 3.8. The noise measurement results of metal and VO_x resistor pairs. The VO_x resistors were fabricated on a glass wafer and the VO_x layer was etched with CF₄ in the RIE equipment. The biasing current was 20 μ A in all of the measurements.

Resistor	Resistance (kΩ)	Thermal Noise (A²/Hz)	β	$C_{1/f}$ parameter	f_c (kHz)
Metal	60	5.5×10^{-25}	1.10	3.8×10^{-12}	1.3
Standard type VO _x	50	6.9×10^{-25}	1.10	1.8×10^{-11}	4.5
Standard type VO _x	52	6.3×10^{-25}	1.10	1.6×10^{-11}	4.5
Standard type VO _x	42	7.8×10^{-25}	1.10	2.3×10^{-11}	5.1

The TCR of a 33 kΩ standard type VO_x resistor was measured under 20 μA bias current and obtained Resistance as well as TCR versus Temperature graphs are given in Figure 3.22. Accordingly, the TCR at 25°C was measured to be -2.4 %/°C.

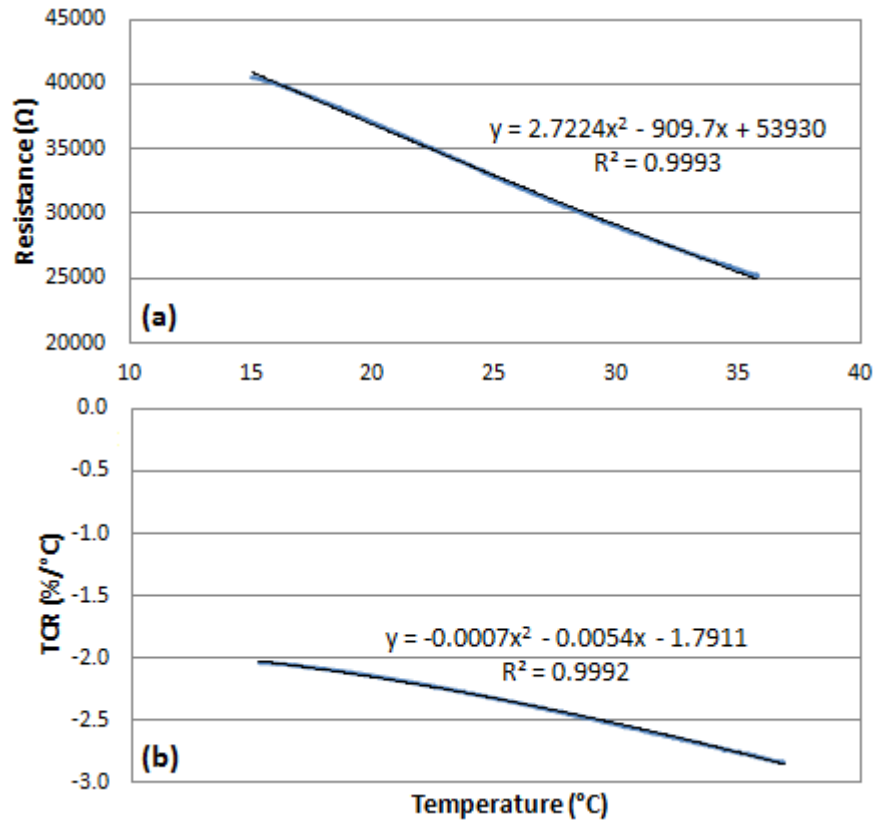


Figure 3.22. The (a) resistance and (b) TCR vs temperature plot of a 33 kΩ standard type VO_x resistor fabricated on a glass wafer and whose VO_x layer was etched with CF₄ in the RIE equipment. The bias current was 20 μA. The TCR at 25°C is -2.4 %/°C.

The comparison of lowest $C_{1/f}$ value of V₂O₅.nH₂O obtained till now with those of other types of bolometric materials reported in literature is shown in Table 3.9. Additionally, the progress in terms of resistance, TCR, and noise performance upto this point in this thesis study is given in Table 3.10.

In order to implement this sol-gel deposited VO_x material into the current microbolometer fabrication process flow being performed in the METU-MEMS facilities, the problem in the dry etching of VO_x should be solved. That is, the selectivity of VO_x RIE recipe to SiN_x should be adjusted. It was also thought whether the lift-off process could be a solution as a second alternative and therefore, its trials were performed. The next section will mention these trials.

Table 3.9. The comparison of $C_{1/f}$ values of different bolometric materials reported in literature with this work.

Material	Deposition Technique	Process Temp. (°C)	Resistivity (Ω .cm)	TCR (%/K)	$C_{1/f}$ Parameter
This work ($V_2O_5.nH_2O$)	Sol-Gel + Annealing	250	< 20	-2.4	1.6×10^{-11}
V-W-O [31,32]	Sputtering + Annealing	300	5	-3.0	6.0×10^{-12}
VO_x [38]	Sputtering	450	< 1	-2.9	4.0×10^{-11}
$Ge_xSi_{1-x}O_y$ [26,42]	Sputtering	25	4×10^3 to 12×10^3	-3 to -5	2.9×10^{-11}
$Si_xGe_{1-x}O_y:H$ [43,44]	Sputtering + Annealing	250	$\sim 10^5$	-4 to -5	2.2×10^{-10}
SiC:H (B doped) [48]	CVD	250	8.1×10^4	2.3	1.5×10^{-10}

Table 3.10. The progress in terms of resistance, TCR, and noise performance upto this point in this thesis study.

	2 nd Fabrication Run	3 rd Fabrication Run	4 th Fabrication Run
PROCESS DETAILS	<u>Sol:</u> 0.1 g $V_2O_5.nH_2O$ / 4 mL water <u>Heat Treatment:</u> 300°C for 1 h	<u>Sol:</u> 0.1 g $V_2O_5.nH_2O$ / 2 mL water <u>Heat Treatment:</u> 300°C for 1 h	<u>Sol:</u> 0.1 g $V_2O_5.nH_2O$ / 3 mL water <u>Heat Treatment:</u> 250°C for 20 min
Resistance (W/L = 47)	135.6 ± 16.3 k Ω	4.2 ± 0.4 k Ω	31.5 ± 5.2 k Ω
TCR @ 25°C	-1.7 %/°C	-1.7 %/°C	-2.4 %/°C
$C_{1/f}$ Parameter	4.7×10^{-11}	NA	1.6×10^{-11}

3.2.1. The VO_x Lift-Off Process Trials

The process flow proposed for VO_x lift-off is given in Figure 3.23. First, a negative photoresist is spun on a Si/SiN_x wafer of which metal electrodes are already formed by following the process steps given in Figure 3.8. After it is patterned by photolithography, the VO_x material is deposited by sol-gel method and its physical water is removed by heat

treatment at 120°C for 20 min. Finally, the photoresist is stripped in acetone which also lifts off the VO_x layer residing on top of it.



(a) Spin coating of a negative photoresist.



(b) Sol-gel VO_x deposition and heat treatment at 120°C for physical water removal.



(c) Stripping the photoresist in acetone which also lifts off the VO_x layer residing on top of it.

Figure 3.23. The representative cross sectional views of VO_x lift-off process.

A first run for VO_x microresistor fabrication by lift-off was performed following the above mentioned process steps. Table 3.11 gives the details of sol-gel VO_x deposition step.

After VO_x lift-off in acetone, some of the resistors were came out to be patterned successfully, however, some of them were not so as shown in Figure 3.24. As a solution to that, the type of negative photoresist was changed and a thicker one was used instead in the second fabrication run. Same process flow including the sol-gel VO_x deposition step given in Table 3.11 was repeated and this time, the resistors were successfully patterned after VO_x lift-off in acetone as shown in Figure 3.25.

Table 3.11. The sol-gel VO_x deposition details of first microresistor fabrication by VO_x lift-off.

Sol	0.1 g of V ₂ O ₅ .nH ₂ O / 3 mL DI water
Spin Speed	Step 1 → 500 rpm for 7 sec Step 2 → 3000 rpm for 1 min
Annealing	at 120°C for 20 min

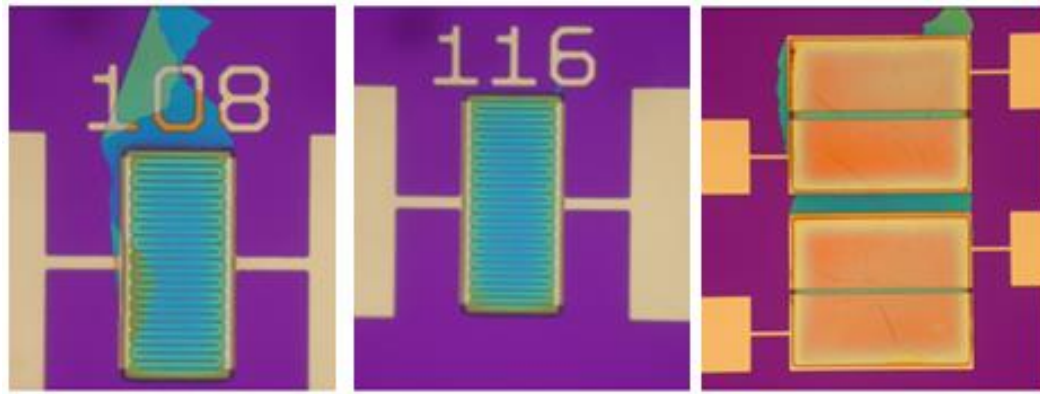


Figure 3.24. The photographs of some resistors after VO_x lift-off of the first fabrication run.

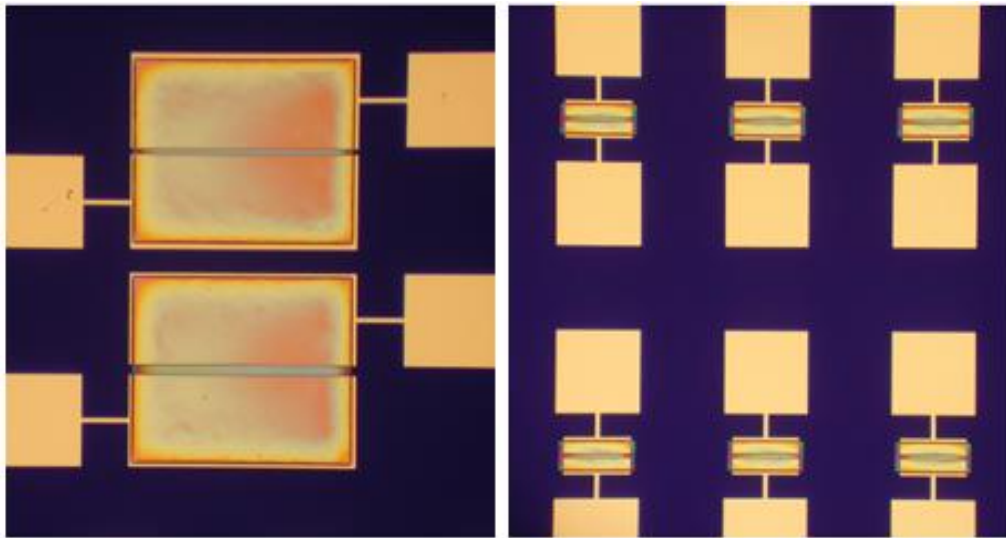


Figure 3.25. The photographs of some resistors after VO_x lift-off of the second fabrication run in which a thicker negative photoresist was used.

The resistance of standard type resistors having a W/L ratio of 47 was measured to be $86.2 \pm 4.1 \text{ k}\Omega$. This value is higher than the one obtained in the fourth microresistor fabrication run mentioned in Section 3.2 (i.e. $31.5 \pm 5.2 \text{ k}\Omega$). One reason for that might be the difference in the annealing temperatures. The TCR of a $90 \text{ k}\Omega$ standard type resistor was measured under $10 \mu\text{A}$ bias current and the obtained Resistance and TCR versus Temperature graphs are given in Figure 3.26. The TCR at 25°C was measured as $-2.4 \text{ \%}/^\circ\text{C}$.

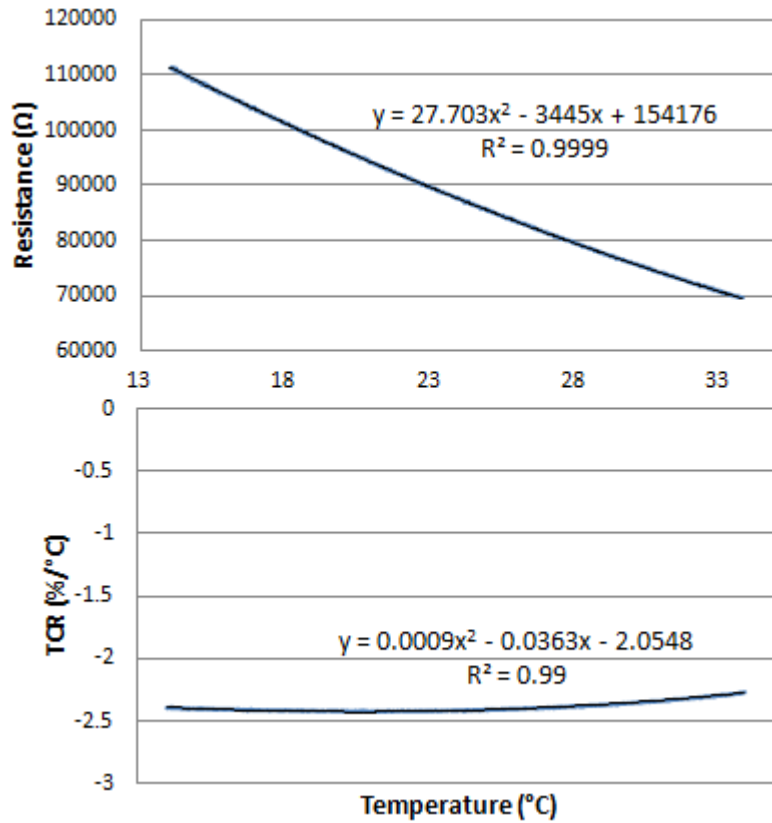


Figure 3.26. The (a) resistance and (b) TCR vs temperature graphs of a 90 kΩ standard type VO_x resistor fabricated by lift-off process. The bias current was 10 μA. The TCR at 25°C is -2.4 %/°C.

The noise of a 63 kΩ standard type resistor pair was measured under 20 μA bias current and obtained noise performance parameters is given in Table 3.12. It is much higher than the values given in Table 3.10 in which the VO_x resistors were fabricated by passivating them with SiN_x and then, etching the VO_x layer by RIE. Then, annealing was performed at two different temperatures, 250°C and 300°C, for 30 min and 1 h, respectively and noise tests of these samples were also conducted. The results are also tabulated in Table 3.12. As it is seen, annealing has positive effect in terms of decreasing resistance and noise, however, the noise is still high when compared to the previously obtained values. The reason for that might be increase in the surface roughness of VO_x layer when it is processed by lift-off.

As a result, resistor fabrication by VO_x lift-off was abandoned due to high noise performance and it was decided to optimize VO_x RIE process instead.

Table 3.12. The noise test results of VO_x resistors processed by lift-off and annealed at different temperatures.

	Resistors annealed @ 120°C for 20 min	Resistors annealed @ 250°C for 30 min	Resistors annealed @ 300°C for 1 h
Resistance (kΩ)	63	66	30
Bias Current (μA)	20	20	20
Thermal Noise Floor (A²/Hz)	5.34x10 ⁻²⁵	4.73 x10 ⁻²⁵	1.1x10 ⁻²⁴
Corner Frequency (kHz)	297	203	95
C_{1/f} parameter	1.4x10 ⁻⁹	7.2x10 ⁻¹⁰	3.7x10 ⁻¹⁰

3.2.2. The Optimization of VO_x RIE

As mentioned before, the VO_x dry etching recipe was decided to be optimized in such a way that it would be more selective to VO_x than SiN_x lying underneath VO_x. Looking at the VO_x RIE recipe given in Table 3.5, two parameters, gas flow rate and power, can be adjusted in order to manipulate VO_x/SiN_x selectivity. One study in literature shows that decreasing power and increasing CF₄ flow rate decrease SiN_x etching rate as given in Table 3.13 [73].

Table 3.13. The silicon nitride etching rate (nm/min) according to the power and flow rate of CF₄ with 4% O₂ [73].

Power (W)	100	150	200	250
Flow (sccm)				
30	40	65	90	140
35	38	70	60	120
40	30	50	80	120

As a first trial, VO_x RIE was performed by decreasing the power from 225 to 20 W. For this, VO_x thin film was sol-gel deposited on a 4" Si wafer on which 80 nm gold had been deposited by sputtering previously. VO_x was coated on Au layer in order to be able to observe the etching of VO_x more easily by inspection. Then, the VO_x layer was annealed at 250°C for half an hour. The wafer was cut into pieces and pasted on 6" wafers with a special thermally conductive compound for VO_x RIE trials as shown in Figure 3.27.

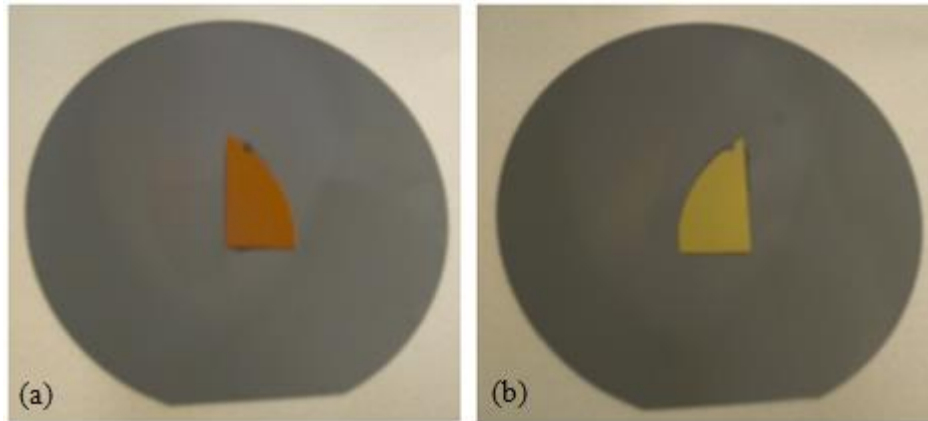


Figure 3.27. The photograph of Si/Au/VO_x wafer piece pasted onto a 6" wafer (a) before and (b) after 30 sec VO_x RIE with 20-W power.

After 30 sec VO_x RIE with 20 W power, the VO_x layer seems to be etched successfully as shown in Figure 3.27b. Then, microresistors on a 4" Si/SiN_x wafer were fabricated. The details of sol-gel VO_x deposition step was kept as the same with the ones given in Table 3.7. The wafers were again cut into pieces and pasted on 6" wafers for VO_x RIE trials. The etching duration of VO_x layer of one sample was kept as 50 sec again with 20 W power. Having inspected under optical microscope, it was seen that the VO_x layer was etched successfully without damaging SiN_x layer underneath.

The resistance of standard type resistors having a W/L ratio of 47 was measured as $32.1 \pm 8.2 \text{ k}\Omega$ which is close to the value obtained after 4th resistor fabrication run given in Table 3.10 (i.e. $31.5 \pm 5.2 \text{ k}\Omega$). This shows the repeatability of fabrication. Then, the noise performance of a 55 k Ω standard type VO_x resistor pair was measured under 20 μA bias current. Beforehand, the noise of a 51 k Ω metal resistor pair was measured under 20 μA bias current for checking the operation of noise measurement set-up. The results are summarized in Table 3.14. The noise parameters of metal resistor pair are again higher than expected. Therefore, the evaluation of VO_x resistor's noise performance should be made accordingly. In any case, its $C_{1/f}$ parameter is not much far from the one obtained previously and given in Table 3.10 (i.e. 1.6×10^{-11}).

After optimizing the VO_x RIE without damaging the SiN_x underneath, the VO_x resistors were fabricated on a 6" Si/SiN_x wafer, however, this time, the VO_x RIE was performed at wafer level, not die level. The details of sol-gel VO_x deposition step was again the same with the ones given in Table 3.7. Having etched the VO_x layer with the power of 20 W for 45 sec, it seems that the RIE of VO_x layer is successful throughout the whole wafer without damaging the SiN_x layer underneath. The photographs of some resistors after VO_x RIE are shown in Figure 3.28. As it is seen, the SiN_x layer remains undamaged.

Table 3.14. The noise measurement results of metal and VO_x resistor pairs. The VO_x layer was etched by RIE with 20-W power. The biasing current was 20 μA in all of them.

Resistor	Resistance (kΩ)	Thermal Noise (A ² /Hz)	β	C _{1/f} parameter	f _c (kHz)
Metal	51	6.5x10 ⁻²⁵	1.10	7.1x10 ⁻¹²	2.0
Standard type VO _x	55	6.0x10 ⁻²⁵	1.10	3.1x10 ⁻¹¹	9.2

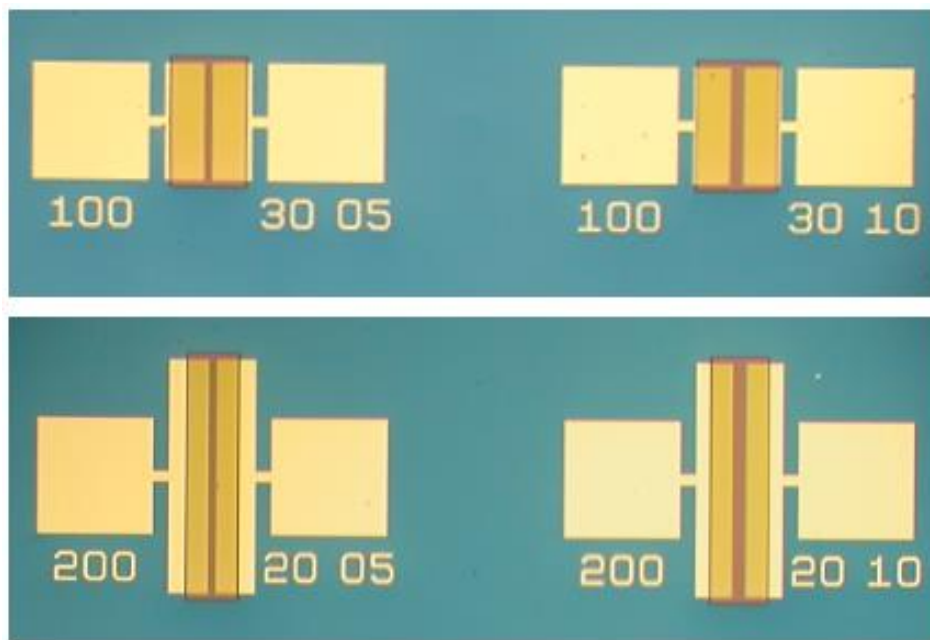


Figure 3.28. The photographs of some resistors from the 6” Si/SiN_x wafer after the VO_x RIE had been performed at 20-W power for 45 sec.

The resistance of standard type resistors having a W/L ratio of 20 was measured to be 66.8 ± 12.1 kΩ. The noise of a 90 kΩ standard type VO_x resistor pair was measured after measuring the noise of a 97 kΩ metal resistor pair under 20 μA bias current. The results are tabulated in Table 3.15. As it is seen, the noise of metal resistor pair is as expected. The noise performance of VO_x resistor pair is close to the one obtained previously and given in Table 3.10 (i.e. 1.6×10^{-11}).

Table 3.15. The noise measurement results of both metal and VO_x resistor pairs. The VO_x resistors were fabricated on a 6” Si/SiN_x wafer and its VO_x layer was etched by RIE with 20-W power. The biasing current was 20 μA in all of them.

Resistor	Resistance (kΩ)	Thermal Noise (A ² /Hz)	β	C _{1/f} parameter	f _c (kHz)
Metal	97	3.4x10 ⁻²⁵	1.10	9.1x10 ⁻¹³	0.6
Standard type VO _x	90	3.8x10 ⁻²⁵	1.10	2.2x10 ⁻¹¹	9.4

3.3. Conclusions

This chapter presented the fabrication of microresistors with sol-gel deposited V₂O₅.nH₂O thin films on 4” and 6” wafers in order to measure the resistance, TCR, and 1/f noise performance. One problem encountered during the fabrication is that photolithography chemicals degraded the VO_x thin film. This problem was solved by passivating the VO_x with a thin layer of SiN_x deposited by PECVD. Another concern during the fabrication of VO_x microresistors is the etching of VO_x layer. Both wet and dry etching were tried and it was seen that dry etching with a gas mixture of CF₄ and O₂ by RIE was much more successful than wet etching in H₂O₂ (aq). The dry etching recipe was made more selective to VO_x than SiN_x by decreasing the RF power from 225 W to 20 W. Finally, the microresistors were fabricated successfully and 60 kΩ resistance for the planar type resistors that can be fit into 35 μm pixel was achieved. The TCR was measured to be between -1.7 and -2.4 %/°C and the lowest 1/f noise parameter, C_{1/f}, was obtained as 1.6x10⁻¹¹ which are promising values for using the V₂O₅.nH₂O phase as a bolometric material. The VO_x lift-off process was also tried. Although, VO_x microresistors were fabricated successfully with the lift-off method, this process was abandoned due to the high 1/f noise performance most probably because of the increased surface roughness of VO_x thin film when processed by lift-off.

CHAPTER 4

SUSPENDED SINGLE PIXEL FABRICATION AND PERFORMANCE TEST RESULTS

This chapter presents the fabrication of suspended single pixels as a first step to implement the developed VO_x material into the microbolometer technology. After the completion of single pixel fabrication, performance tests which are thermal conductance, responsivity, thermal time constant, and absorptance measurements were conducted in addition to the TCR and 1/f noise measurements. Section 4.1 describes the method of doing these additional performance tests. Section 4.2 gives the details of suspended pixel fabrication and performance test results. Section 4.3 summarizes and concludes the chapter.

4.1. The Description of Thermal Conductance, Responsivity, and IR Absorptance Measurements

The thermal conductance (G_{th}), responsivity (R_V), and IR absorptance (η) of a suspended single pixel were measured by utilizing SÜSS MicroTec PAV 200 equipment found in the METU-MEMS facilities. The photograph of equipment is shown in Figure 4.1.

For thermal conductance measurement, the sample is placed in the equipment chamber and the probes are lowered on the pads of sample for applying current and measuring voltage. By this way, the resistance is calculated by simply dividing the measured voltage to the applied current.

First, the resistance of pixel is measured at atmospheric pressure and this is accepted as the real resistance value because, the detector is assumed not to be heated up with the applied electrical power at atmospheric pressure. Then, the chamber is vacuumed and the detector resistance is again measured by applying the same constant current. This time the resistance will be different due to the heating up of detector with the applied electrical power. Then, the thermal conductance is calculated by using the following equation [6]:

$$G_{th} = \frac{I^2 R \alpha}{\ln\left(\frac{R}{R_0}\right)} \quad (4.1)$$

where G_{th} is detector's thermal conductance, I is applied bias current, R is detector resistance under vacuum, α is TCR of the detector, and R_0 is detector resistance at atmospheric pressure.



Figure 4.1. The photograph of SÜSS MicroTec PAV 200 equipment utilized in the thermal conductance, responsivity, and absorptance measurements.

As mentioned in Section 1.4, responsivity is another performance parameter for microbolometers which is defined as the output signal of detector per infrared radiation power incident on the detector. It has the unit of V/W when the detector is biased with constant voltage. Utilizing the thermal circuit analogy of a microbolometer to an electrical circuit as described in Section 1.4, the current responsivity, R_V , is finally derived as:

$$R_V = \frac{\eta I_d \alpha R_d}{G_{th} \sqrt{1 + (\omega \tau)^2}} = \frac{R_{DC}}{\sqrt{1 + (\omega \tau)^2}} \quad (4.2)$$

where η is absorptance, I_d is bias current, α is TCR, R_d is detector resistance, G_{th} is thermal conductance, ω is modulation frequency of the infrared power, and τ is thermal time constant. As depicted in Eqn (4.2), the term $(\eta I_d \alpha R_d / G_{th})$ is expressed as DC responsivity, R_{DC} , where the incident radiation is not modulated.

For responsivity measurement, the detector is again placed in the equipment chamber which is vacuumed afterwards in order to eliminate the thermal conductance of air and increase the detector performance. A germanium window and a blackbody are placed on the top window of chamber for the IR radiation to enter the chamber. “The blackbody is heated to 1000°C and the radiation coming from the blackbody is modulated by the help of a frequency

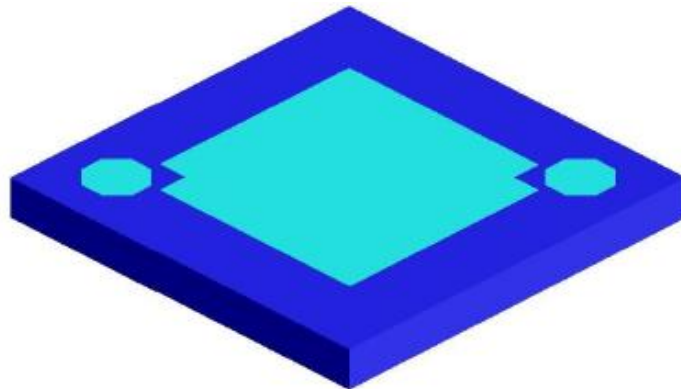
controlled chopper. A reference detector is used to measure the power of the infrared radiation. The detector is biased at constant current (0.1 μA in this test in order to eliminate the self-heating effect) with a current source and the voltage across the detector is measured with a dynamic signal analyzer. The signal at the chopping frequency gives the voltage value on the detector due to the infrared radiation. The ratio of this voltage to the incident infrared power gives the voltage responsivity of the detector at that frequency [6].”

After measuring the responsivity at different modulation frequencies, curve fitting is applied onto that data and by this way, the DC responsivity is extracted. After substituting the DC responsivity into Eqn (4.2), the absorptance (η) can easily be calculated because, the detector bias current, resistance, thermal conductance, and TCR are also known.

4.2. The Fabrication of Suspended Single Pixels and Performance Test Results

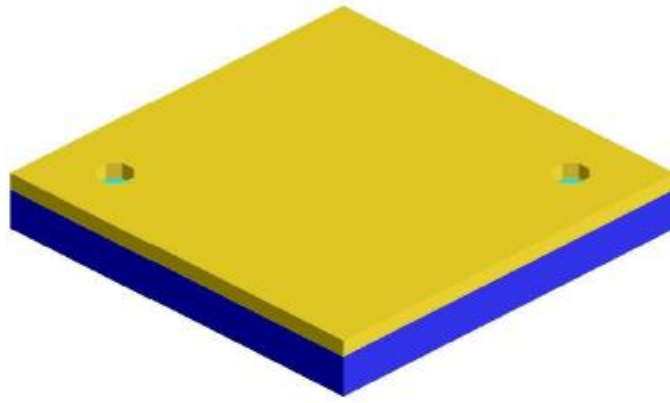
The 3-D view of process steps to be followed in the fabrication of 35 μm suspended single pixels into which the developed sol-gel deposited VO_x material is going to be implemented are shown in Figure 4.2 [6]. The process steps apart from the VO_x deposition had already been optimized in the context of other thesis studies conducted at METU [6,18]. Therefore, these optimized recipes whose details are given in Appendix A were followed during the fabrication of single pixels.

Figure 4.3 shows one pixel from one die drawn by utilizing Cadence software program which was going to be fabricated. The other pixels in the same die have different electrodes and arms in size for optimization purposes (The pixels were designed and their mask set for fabrication was drawn by Başak Kebapçı).

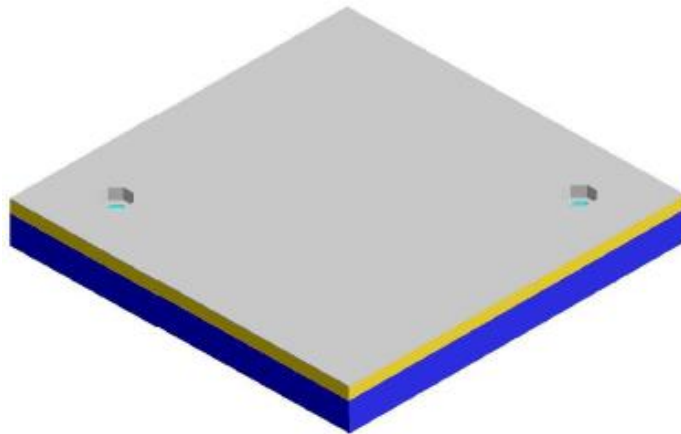


(a) The deposition and patterning of metal layer used as a mirror for IR radiation

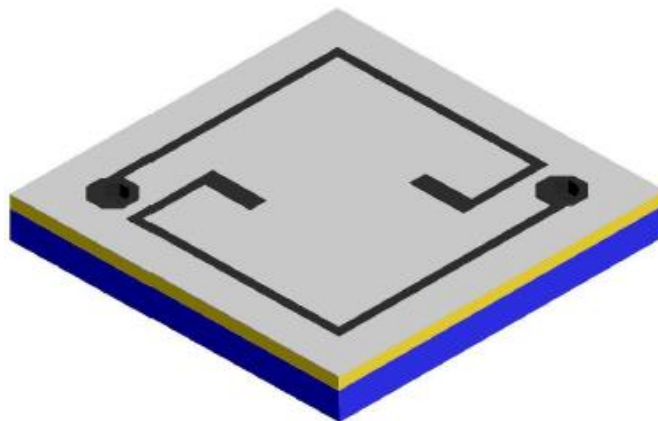
Figure 4.2. The 3-D view of process steps for the fabrication of suspended single pixels [6].



(b) The deposition and patterning of sacrificial layer that the pixel is built on

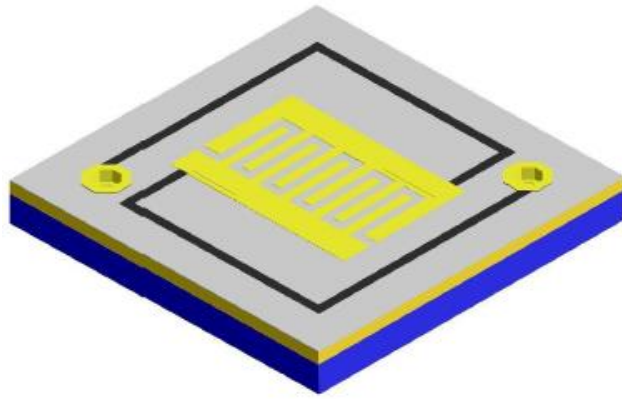


(c) The deposition and patterning of structural layer and opening contacts at the anchors

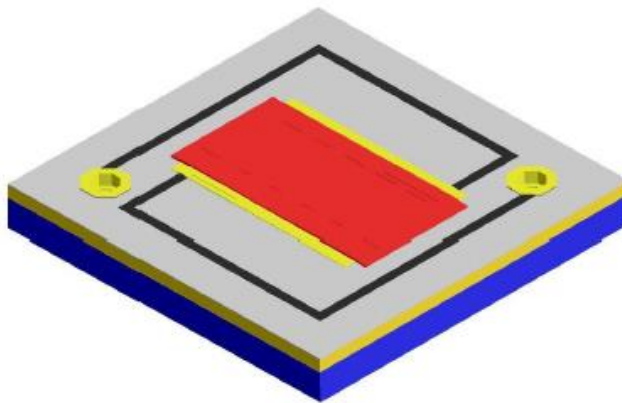


(d) The deposition and patterning of interconnect metal arms

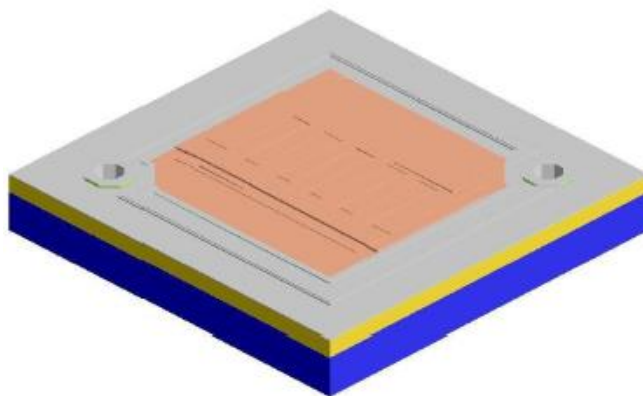
Figure 4.2 (cont'd). The 3-D view of process steps for the fabrication of suspended single pixels [6].



(e) The deposition and patterning of electrode metals

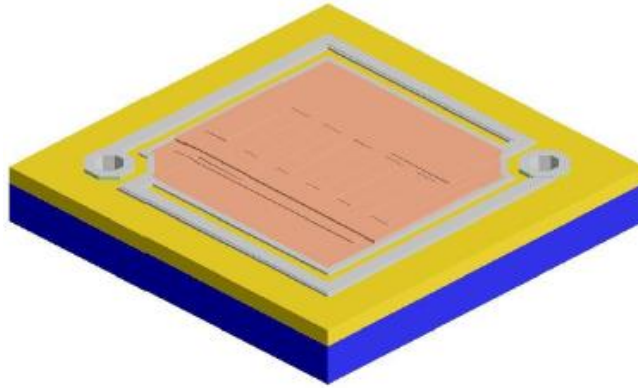


(f) The deposition and patterning of active detector material

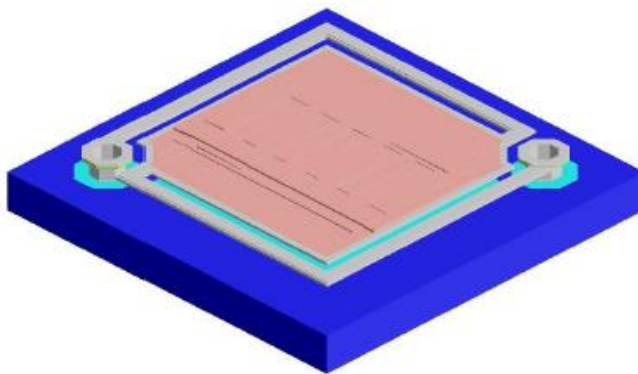


(g) The deposition of upper structural layer followed by the deposition and patterning of absorber layer

Figure 4.2 (cont'd). The 3-D view of process steps for the fabrication of suspended single pixels [6].



(h) The patterning of structural layer to obtain the support arms and pixel body



(g) The etching of sacrificial layer and isolation of pixel from the substrate

Figure 4.2 (cont'd). The 3-D view of process steps for the fabrication of suspended single pixels [6].

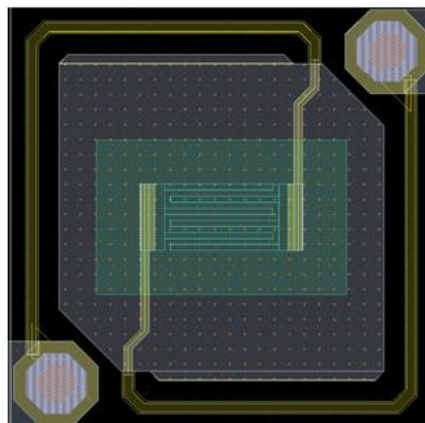


Figure 4.3. The representation of one pixel having 35 μm pitch into which the developed sol-gel deposited VO_x material is going to be implemented during its fabrication.

The sixth step of fabrication process is the deposition and patterning of VO_x layer as given in Appendix A. The details of sol-gel VO_x deposition in this step is given in Table 4.1.

Table 4.1. The sol-gel VO_x deposition details of suspended single pixel fabrication.

Sol	0.1 g of $\text{V}_2\text{O}_5 \cdot n\text{H}_2\text{O}$ / 3 mL DI water
Spin Speed	Step 1 → 500 rpm for 7 sec Step 2 → 3000 rpm for 1 min
Annealing	at 250°C for 20 min

The final process of the sixth step (i.e. after the VO_x RIE) is the removal of photoresist as known. The procedure given below was followed for stripping the photoresist: i) Applying 10-min O_2 plasma, ii) Keeping in acetone for 15 min, iii) Rinsing with isopropyl alcohol, and iv) Applying additional 10-min O_2 plasma for removing photoresist residuals.

The photoresist seemed to be removed successfully under optical microscope. The wafer was also inspected in the SEM and the photoresist seems to be removed in the SEM, too, as shown in Figure 4.4. However, the resistance values increased nearly two fold. Either Ti arms were oxidized or VO_x changed characteristics due to the O_2 plasma application. This photoresist removal step should be optimized in the future work. Nevertheless, the fabrication of single pixels was continued anyway in spite of this resistance increase after the photoresist stripping.

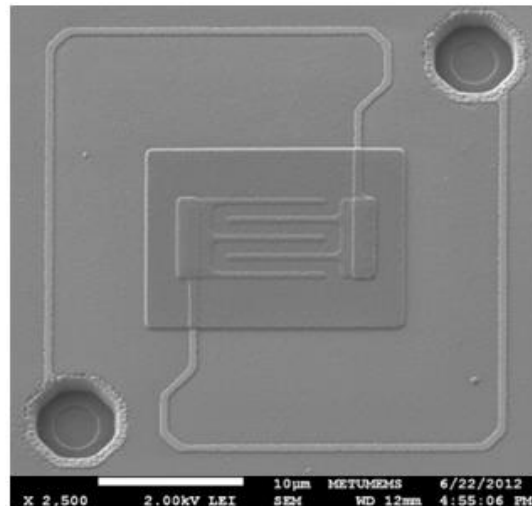


Figure 4.4. The SEM photograph of one pixel after the VO_x layer was patterned and the photoresist was removed.

Having conducted the final fabrication step which is the suspension of pixels by removing the sacrificial layer (i.e. polyimide) in O_2 plasma, the pixels were released successfully. To note that, the wafer was cut into pieces beforehand to perform the releasing die level. The photographs of some pixels both under optical microscope and in the SEM are shown in Figure 4.5.

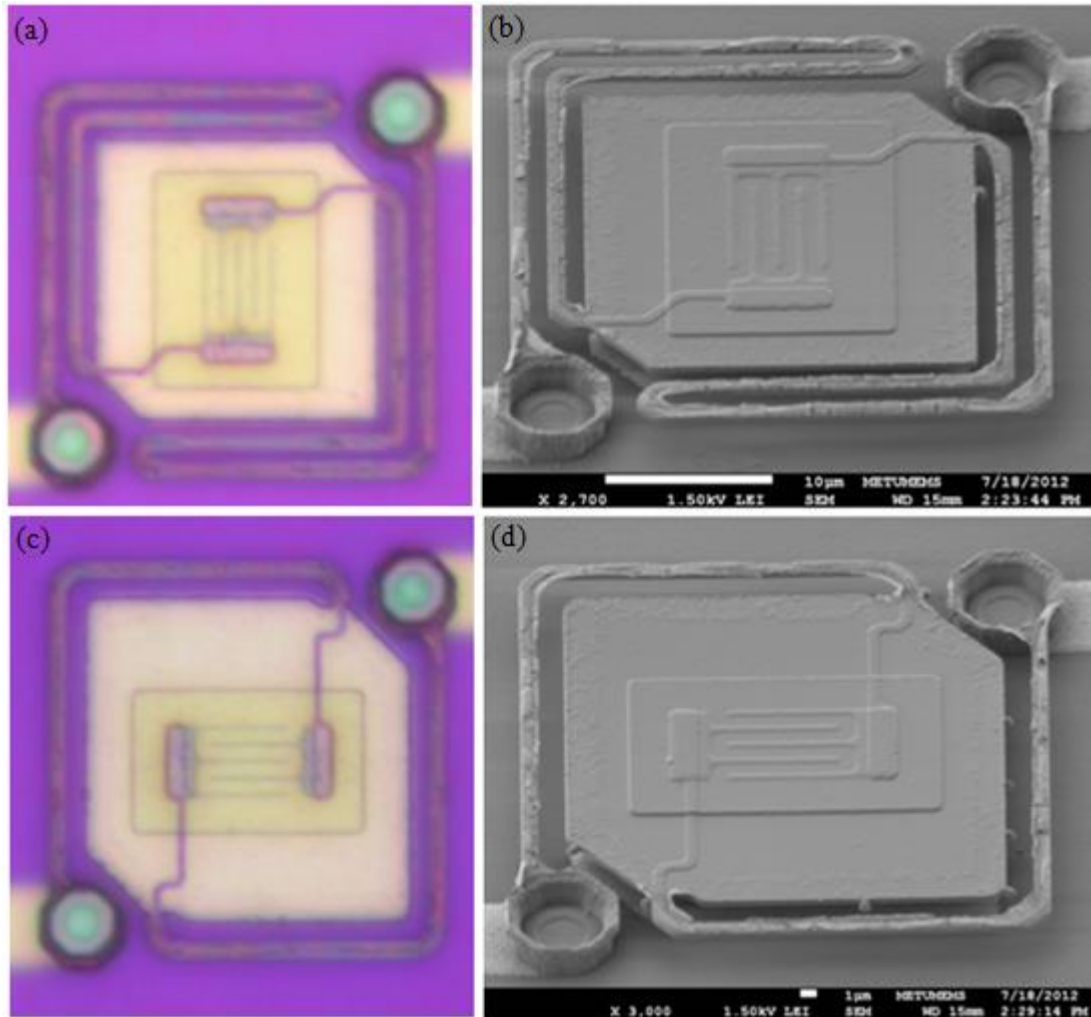


Figure 4.5. The photographs of some pixels both under optical microscope and in the SEM after releasing by etching the polyimide in O_2 plasma.

The resistance of pixels having the electrode type shown in Figure 4.5 (W/L ratio = 54.7) was measured to be $78.2 \pm 6.2 \text{ k}\Omega$. First, the TCR of a $90 \text{ k}\Omega$ pixel was measured under $2 \mu\text{A}$ bias current. The resistance and TCR vs temperature curves are given in Figure 4.6. The TCR at 25°C is $-2.4 \text{ \%/}^\circ\text{C}$.

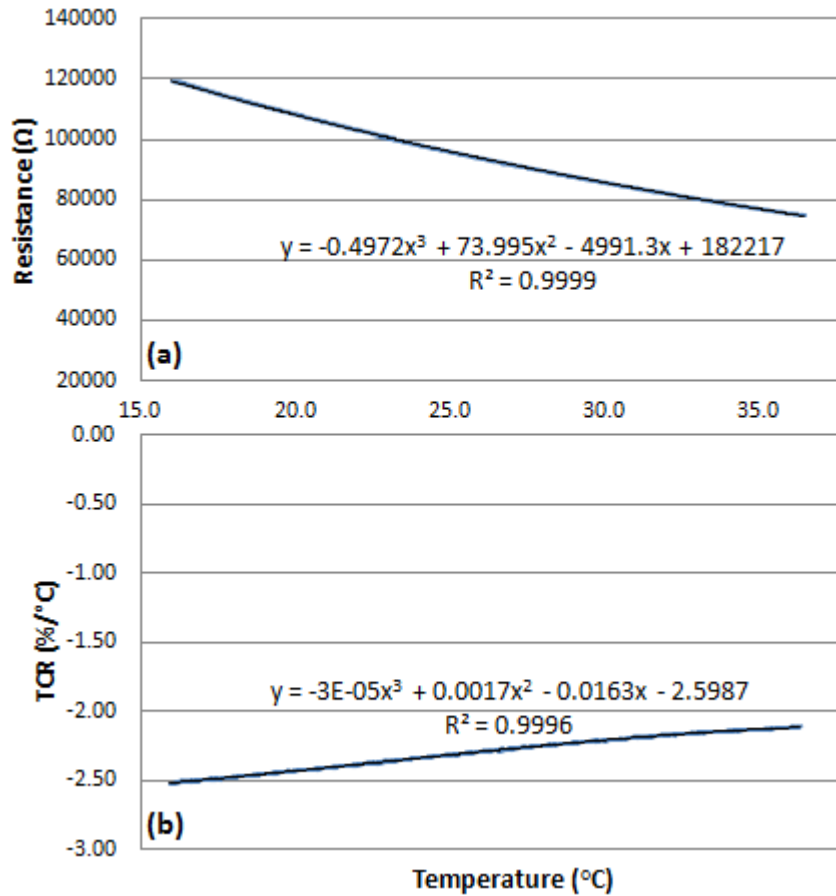


Figure 4.6. The (a) resistance and (b) TCR vs temperature graphs of a 90 kΩ VO_x single pixel. The bias current was 2 μA. The TCR at 25°C is -2.4 %/°C.

Second, the flicker noise of two 75 kΩ resistor pairs was tried to be measured under 20 μA. However, a consistent power spectral density could not be obtained due to the instability problem in the noise measurement set-up, although, it was checked to be operating properly by measuring the noise of a 75 kΩ metal resistor pair under 20 μA bias current in advance.

When the pixels are inspected under the SEM at a higher magnification, it is observed that there is some kind of residue all over the field after pixel releasing as given in Figure 4.7. The gold pads also seem to be not perfectly clean when inspected under optical microscope. Therefore, the problem in the noise measurement might be due to poor electrical contacts arising from the contaminated pads and field.

The thermal conductance of a single pixel having the type shown in Figure 4.5a and resistance of 84 kΩ was measured as described in Section 4.1 and it was found to be 3.37×10^{-8} W/K which has the expected order of magnitude (i.e. 10^{-8} W/K) (The measurement was performed by Dr. Yusuf Tanrıku).

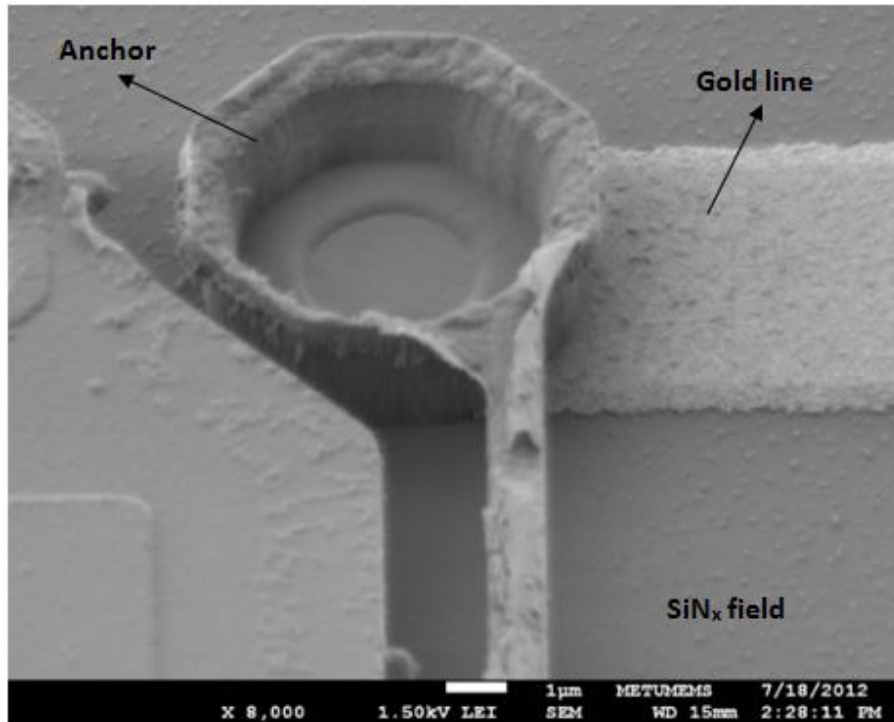


Figure 4.7. The SEM photograph of anchor of one suspended single pixel. There is some kind of residue all over the SiN_x field and on the gold metal lines.

The responsivity of pixel used in the thermal conductance measurement was measured under $1 \mu\text{A}$ bias current at different modulation frequencies (the measurement was performed by Dr. Yusuf Tanrikulu). Figure 4.8 gives this responsivity data measured at different modulation frequencies. From the fitted curve shown in Figure 4.8, the DC responsivity and thermal time constant (τ) are extracted as $50,569 \text{ V/W}$ and 20.9 ms , respectively. By using Eqn (4.2), the absorptance (η) is found as 87% .

In order to investigate the noise performance, it was decided to fabricate only the resistors of $35 \mu\text{m}$ single pixels instead of starting another single pixel fabrication run, because, it would be much easier and less time consuming.

Having followed the resistor fabrication steps depicted in Figure 3.8 in Section 3.2, the VO_x resistors were formed successfully as shown in Figure 4.9. The details of sol-gel VO_x deposition step were the same with the ones given in Table 4.1. To note that, metal reactive ion etching (MRIE) was utilized instead of wet etching for the formation of metal electrodes this time because, the finger thickness and space between the fingers are 0.5 , 0.7 , or $1.0 \mu\text{m}$.

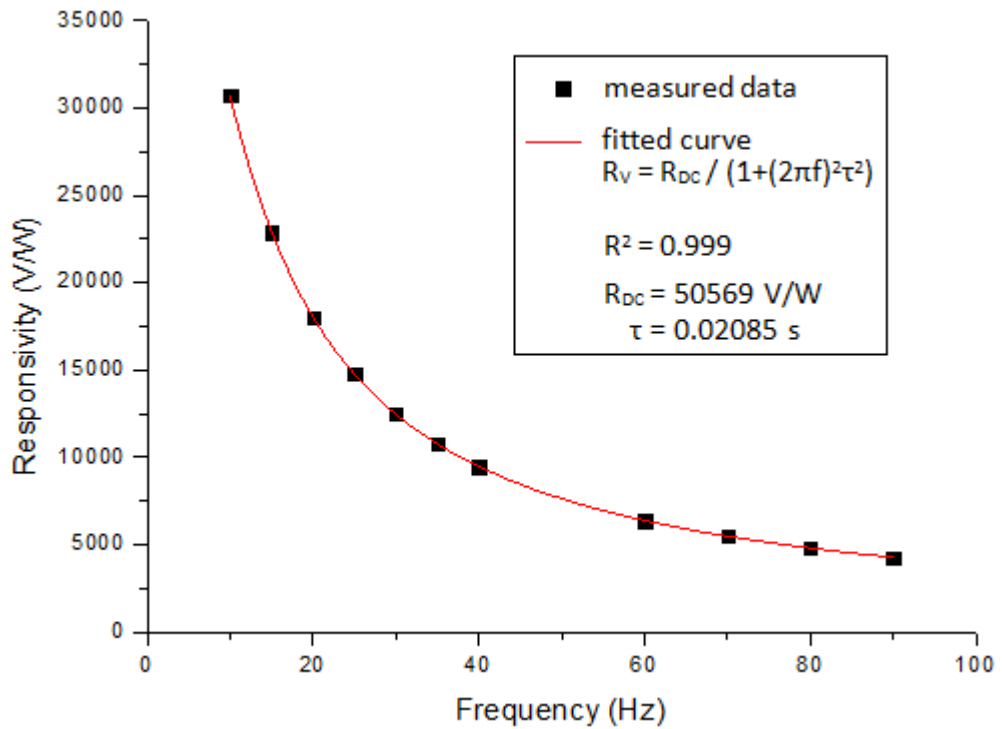


Figure 4.8. The responsivity measurement of pixel having the type shown in Figure 4.5a and resistance of 84 kΩ under 0.1 μA bias current at different modulation frequencies.

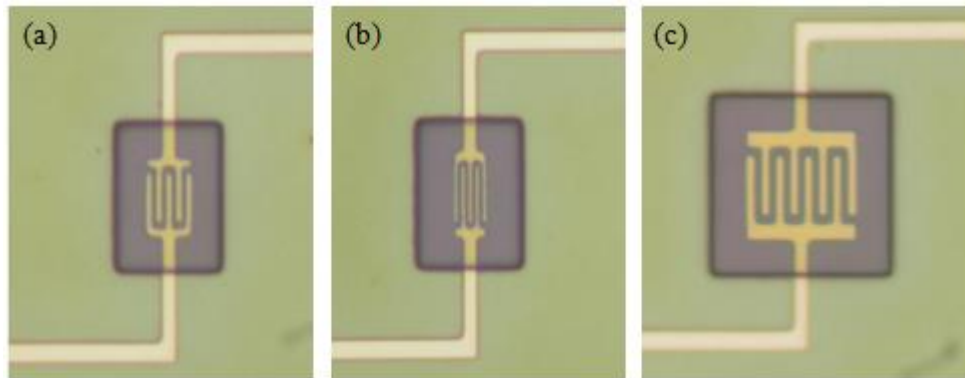


Figure 4.9. The photographs of VO_x test resistors of 35 μm pitch single pixels after the deposition and patterning of the VO_x layer.

The resistance of VO_x resistors having the type shown in Figure 4.9c (W/L = 84) was measured to be 18.3 ± 5.2 kΩ. Then, the flicker noise of two resistor pairs again having the type shown in Figure 4.9c was measured under 20 μA bias current and obtained noise performance parameters are given in Table 4.2. As it is seen, the noise is measured to be higher than the ones obtained previously and given in Table 3.10 (The minimum $C_{1/f}$

parameter obtained is 1.6×10^{-11}). However, the noise is expected to be higher in this case because, as mentioned before the noise measurement set-up had been designed for measuring the noise of resistors having resistance higher than 40 k Ω and when the resistance is lower than this value, the noise of transistors increases, hence, bringing additional noise source in the overall noise power spectral density [72]. This can be understood by checking the noise performance parameters of 10 k Ω and 22 k Ω metal resistor pairs under 20 μ A bias current tabulated in Table 4.2. The expected values, which are much less than the measured ones, are also given in the table. Therefore, the measured noise values of VO_x resistors should be evaluated taking this into consideration.

Table 4.2. The noise measurement results of metal and VO_x resistor pairs under 20 μ A bias current. The VO_x resistors are the test resistors of 35 μ m pitch pixels.

Resistor	Resistance (k Ω)	Thermal Noise (A ² /Hz)	β	$C_{1/f}$ parameter	f_c (kHz)
Metal*	10	2.4×10^{-24}	1.10	3.2×10^{-11}	2.5
Metal*	22	9.1×10^{-25}	1.10	2.9×10^{-11}	1.5
VO _x resistor	15	2.4×10^{-24}	1.10	9.3×10^{-10}	88
VO _x resistor	23	1.4×10^{-24}	1.10	4.7×10^{-10}	58

* The expected values: $C_{1/f} < 1.0 \times 10^{-12}$ and $f_c < 0.6$ kHz

4.3. Conclusions

This chapter presented the fabrication of 35 μ m suspended single pixels as a first step to implement the developed VO_x material into the microbolometer technology. The pixels were fabricated successfully and their performance tests were conducted. The TCR at 25°C was measured to be -2.4 %/°C. It was attempted to perform 1/f noise measurement, however, a consistent power spectral density could not be obtained because of the instability problem in the noise measurement set-up most probably due to the poor electrical contacts. The other performance parameters, thermal conductance, DC responsivity, thermal time constant, and absorptance were measured as 3.37×10^{-8} W/K, 50,569 V/W, 20.9 ms, and 87 %, respectively. These results show that sol-gel deposited vanadium pentoxide gel can be used as an IR active material in large microbolometer FPAs such as 384x288 for obtaining good performance.

CHAPTER 5

FABRICATION OF 384x288 MICROBOLOMETER FOCAL PLANE ARRAY AND PERFORMANCE MEASUREMENTS

A 384x288 microbolometer array having 35 μm pixels on a 6" ROIC wafer was planned to be fabricated in which sol-gel deposited VO_x was going to be used as the IR active material (The ROIC portion of the detector was designed by Alperen Toprak [74]). Before fabricating the microbolometer array, the test resistors having the same type of electrodes with the array pixels were planned to be prepared in order to investigate resistance, TCR and 1/f noise performance of sol-gel deposited VO_x . Section 5.1 mentions the fabrication and test results of these test resistors and Section 5.2 gives the details of microbolometer array fabrication. The summary and conclusions of the chapter is presented in Section 5.3.

5.1. The Fabrication of Test Resistors of 384x288 Microbolometer Array

The type of one pixel from the 384x288 microbolometer array which is going to be fabricated is shown in Figure 5.1a and its test resistor is given in Figure 5.1b.

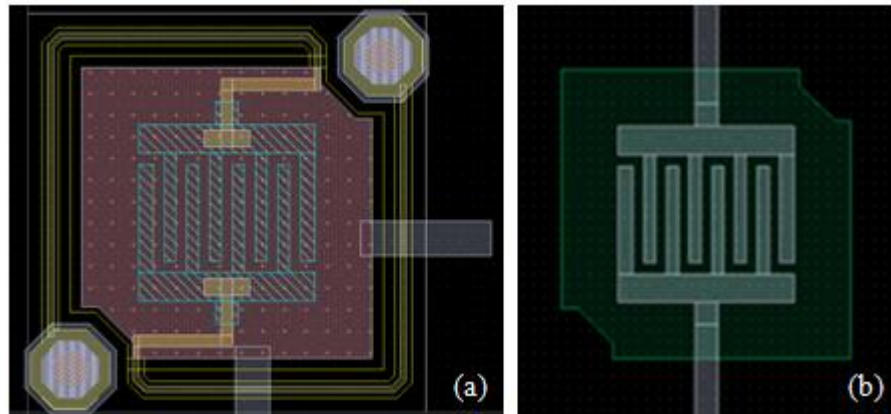


Figure 5.1. The representation of (a) 35 μm pixel whose 384x288 microbolometer array is going to be fabricated on a 6" ROIC wafer and (b) its test resistor.

The sol-gel deposited VO_x test resistors of pixel shown in Figure 5.1 has the same type with the resistors fabricated previously and shown in Figure 4.9c in Chapter 4. Their noise tests

had also been performed of which results are tabulated in Table 4.2. However, the resistance was measured to be ranging between 15 and 25 k Ω which is low for the detector on a ROIC wafer (The sol used for VO_x deposition had been prepared as 0.1 g V₂O₅.nH₂O/3 mL water). The resistance should be higher than 40 k Ω in order to be compatible with the ROIC. Therefore, in order to increase the resistance, it was planned to use a more dilute sol while depositing the VO_x layer. That is, the water amount was increased to 3.7 mL per 0.1 g V₂O₅.nH₂O and new test resistors were fabricated accordingly following the process steps depicted in Figure 3.8. Figure 5.2 shows the photographs of a test resistor under optical microscope after some process steps.

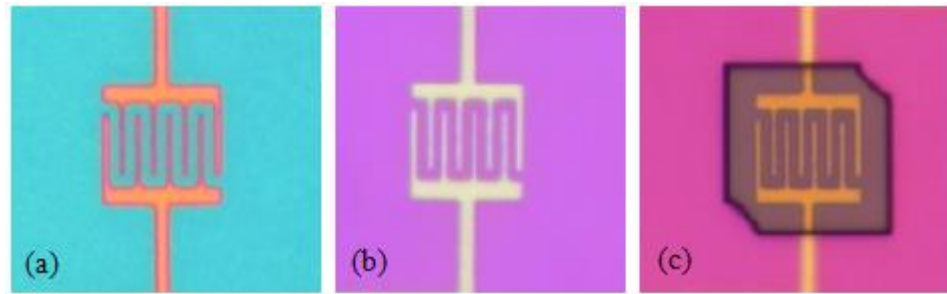


Figure 5.2. The photographs of a test resistor after (a) VO_x deposition and annealing at 250°C for 20 min, (b) SiN_x PECVD for VO_x passivation, and (c) photolithography for SiN_x and VO_x RIE.

After the resistors were patterned successfully, the resistance was measured at certain locations throughout the whole 6" wafer. The results are shown in Figure 5.3. The average resistance was measured as 55.8 \pm 9.8 k Ω and the resistance non-uniformity was calculated as 30.1 % using the formula given below:

$$U(\%) = \frac{R_{max} - R_{min}}{2R_{avg}} \times 100 \quad (5.1)$$

where U is non-uniformity, R_{max} is maximum resistance, R_{min} is minimum resistance, and R_{avg} is the average of all measured resistance. The calculated 30.1 % non-uniformity is most probably due to the thickness variation of VO_x thin film throughout the wafer coming from the spin coating technique itself. Additionally, because the finger type electrodes were patterned by wet etching, there would be variation in their W/L ratio (see Figure 3.7) throughout the wafer which would also bring variation in the resistance. However, die level non-uniformity is a more important parameter than the wafer level non-uniformity as long as the resistance is below 100 k Ω . The resistance variation in one die can be compensated by the designed ROIC on which the detectors will be fabricated as long as the resistance is varying \pm 5 % [72].

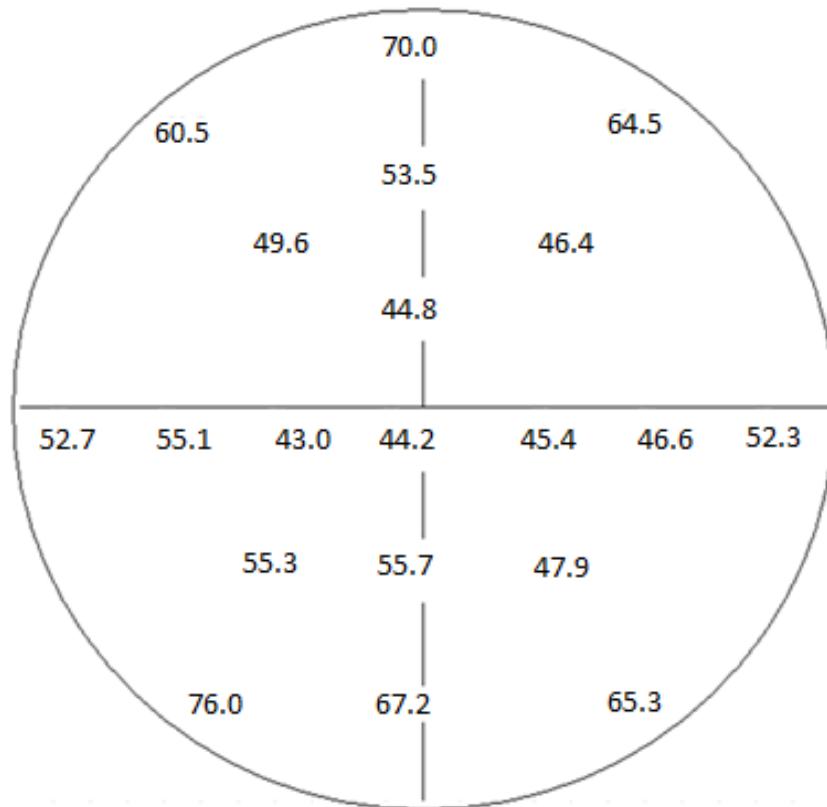


Figure 5.3. The measured resistance values of VO_x test resistors in kΩ and their location on the 6" wafer. The average resistance and non-uniformity were measured as 55.8 ± 9.8 kΩ and 30.1 %, respectively.

Second, the TCR of a 60 kΩ VO_x resistor was measured under 2 μA bias current. The resistance vs temperature and TCR vs temperature plots are given in Figure 5.4a and Figure 5.4b. The TCR at 25°C is -1.9 %/°C.

The noise of a 46 kΩ VO_x resistor pair was measured after measuring the noise of a 51 kΩ metal resistor pair under 20 μA bias current. The noise measurement results are tabulated in Table 5.1. As it is seen, the noise of metal resistor pair was again measured to be higher than expected. Therefore, the noise of VO_x resistor pair should be evaluated accordingly.

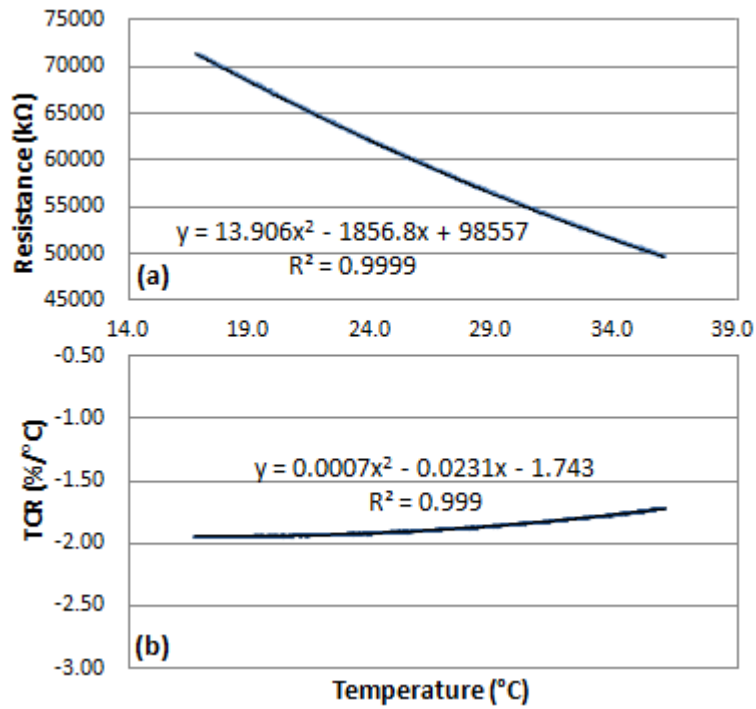


Figure 5.4. The (a) resistance and (b) TCR vs temperature graphs of a 60 kΩ VO_x single pixel. The bias current was 2 μA. The TCR at 25°C is -1.9 %/°C.

Table 5.1. The noise measurement results of metal and VO_x resistor pairs under 20 μA bias current.

Resistor	Resistance (kΩ)	Thermal Noise (A ² /Hz)	β	$C_{1/f}$ parameter	f_c (kHz)
Metal*	51	6.5×10^{-25}	1.10	1.1×10^{-11}	3.0
VO _x resistor	46	7.0×10^{-25}	1.10	6.3×10^{-10}	133

* The expected values: $C_{1/f} < 1.0 \times 10^{-12}$ and $f_c < 0.6$ kHz

After fabricating the test resistors of 384x288 microbolometer array and seeing that the resistance was achieved to be in the vicinity of 60 kΩ, the 384x288 microbolometer array on a ROIC wafer was started to be fabricated with one dummy wafer in addition. The details of this process will be given in the next section.

5.2. The Fabrication of 384x288 Microbolometer Array on a 6" ROIC Wafer

The fabrication steps of microbolometer array are same with those of single pixel fabrication whose 3-D views are represented in Figure 4.2 and described in Section 3.2.

The first fabrication step is mirror layer formation as depicted in Figure 4.2. For this, 20 nm Ti and 80 nm Au are deposited sequentially by sputtering and then, these metals are patterned by wet etching after photolithography. As shown in Figure 5.5, the mirror layer was formed successfully.

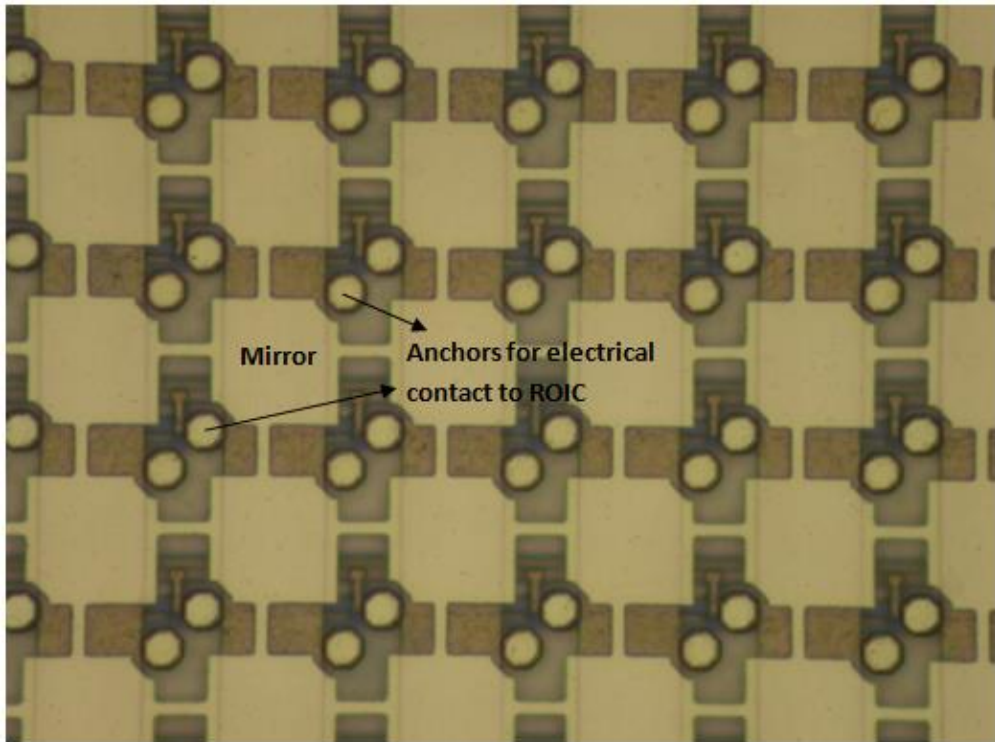


Figure 5.5. The photograph of mirror layer formed for microbolometer array fabrication on a ROIC wafer under optical microscope.

The second fabrication step is deposition and patterning of sacrificial layer which is polyimide (PI) in our case. For this, the polyimide is spun onto the wafer and cured at 300°C first. Then, 20 nm titanium as the masking material is sputtered onto the PI because, PI is etched by O₂ plasma in the RIE equipment and the photoresist would not stand if it was used as the masking material alone. After photolithography, Ti is patterned by wet etching (the etchant is HF:H₂O₂:H₂O in the ratio of 1:1:400) and finally, PI is etched by RIE. After, PI patterning, the Ti layer is stripped by again using the same wet etchant. These process steps for PI patterning are also represented in Figure 5.6.

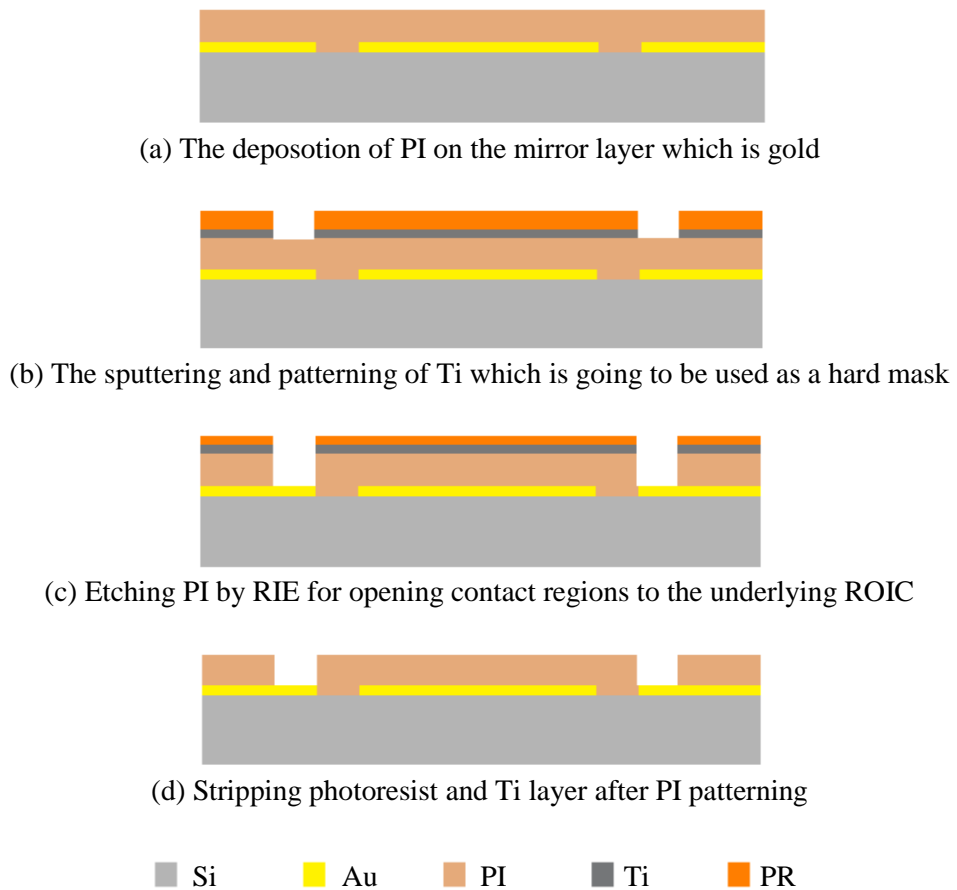


Figure 5.6. The representation of process steps for PI patterning for opening contact regions to the underlying ROIC.

The process steps till Ti wet etching mentioned above were realized successfully. However, an interesting problem arose in the step of Ti wet etching. That is, Ti on the anchor regions couldn't be removed no matter the etching duration was kept longer. Stripping all titanium layer in the wet etchant for redeposition of it was tried, nevertheless, Ti on the anchor regions had not still gone, although, Ti on the field other than the contact regions were all etched away as shown in Figure 5.7a. The second interesting thing is that this problem didn't arise in the dummy wafer as shown in Figure 5.7b.

In order to remove this unknown Ti compound, several etching methods which are listed below were, however, no change was observed:

- HF:H₂O₂:H₂O in the ratio of 1:1:115 for 10 min
- HF:H₂O₂:H₂O in the ratio of 1:1:36 for 15 min
- NH₃:H₂O₂ in the ratio of 1:8 for 3 min
- Pure % 48 HF for 3 min

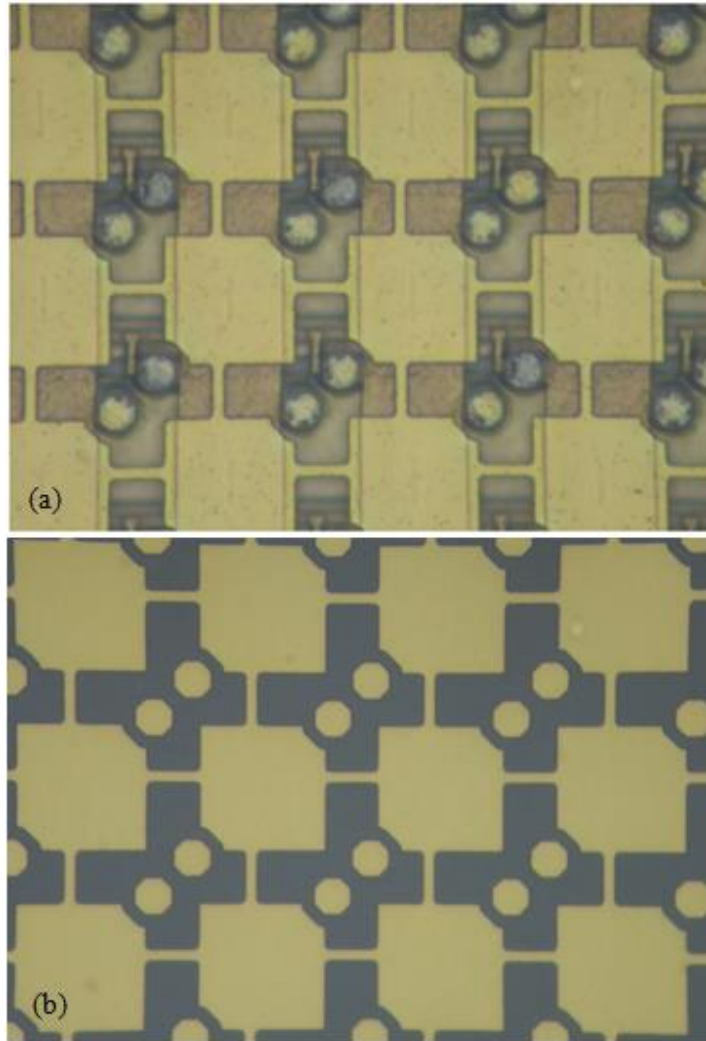


Figure 5.7. The photograph of (a) ROIC wafer and (b) dummy wafer after Ti used as the masking material for PI patterning was stripped. The ROIC wafer has unknown Ti compound remnants whereas the dummy wafer does not so.

Metal reactive ion etching (MRIE) recipes for etching gold and titanium thin films were also tried separately, nonetheless, these trials didn't solve the problem.

A literature survey was conducted about whether Ti could react with PI or not. It was found that it could so and the resulting compound is TiC [75]. Then, the wet etchants for TiC was searched and a study in which a mixture of $\text{HNO}_3:\text{H}_2\text{SO}_4:\text{H}_2\text{O}$ in a ratio of 5:1:4 is used for etching TiC thin film was found [76]. This mentioned acid mixture and also aqua regia solution ($\text{HNO}_3:\text{HCl}:\text{H}_2\text{O}$ in a ratio of 1:2:5) were tried, however, they didn't etch the unknown Ti compound too. As a next solution to this problem, the type of PI was changed but, the problem still continued. Moreover, using aluminum as the masking material instead of Ti was tried. Unfortunately, aluminum also left remnants on the anchor regions like Ti.

Finally, it was decided to replace the PI with amorphous silicon (a-Si) as the sacrificial layer. This replacement brings the requirement of a-Si etching optimization with XeF_2 which is beyond the scope of this thesis study for the suspension of pixels without damaging them. This optimization study had been conducted by Dr. Yusuf Tanrikulu and accomplished in the end after many trails. The SEM picture of a successfully released pixel is given in Figure 5.8. Note that, the pixel structures were made out of SiN_x only.

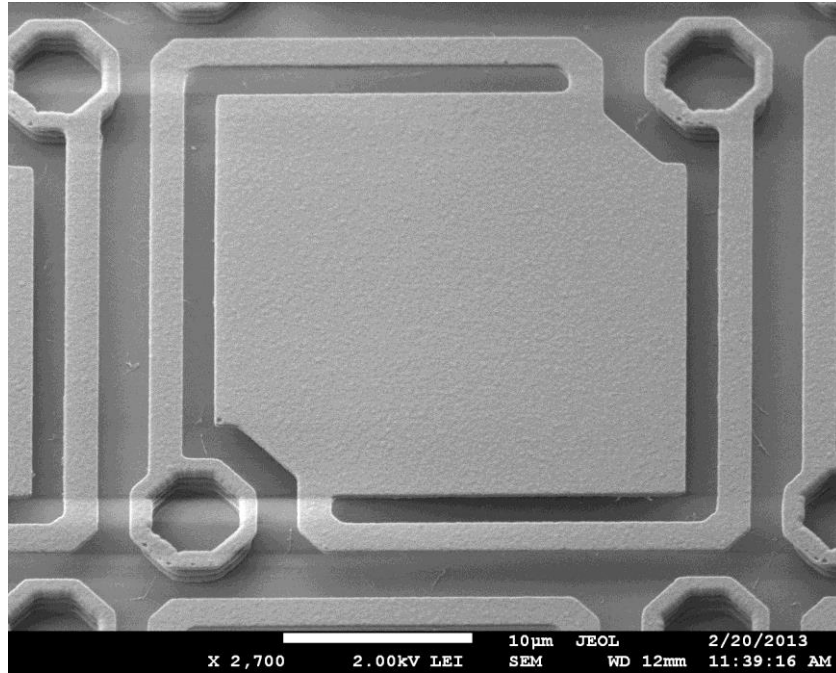


Figure 5.8. The SEM picture of a successfully suspended pixel made out of SiN_x only by etching a-Si as the sacrificial layer with XeF_2 .

Afterwards, it was planned to fabricate full pixel bodies (including the Ti arms, Au electrodes, IR active material, and absorber layer) in an array on plain Si wafers using a-Si as the sacrificial layer and perform releasing of them with the optimized XeF_2 recipe. This study was also completed successfully by Eren Çanga. Figure 5.9 shows the SEM picture of a region from that fabricated microbolometer array.

After the optimization of a-Si as the sacrificial layer was completed, the fabrication of 384x288 microbolometer array with the sol-gel deposited VO_x on a ROIC was started again by using a-Si instead of PI as the sacrificial layer this time. The details of process steps followed during the array fabrication are given in Appendix B. Figure 5.10 shows the photograph of a region from the array under optical microscope after the realization of each process step.

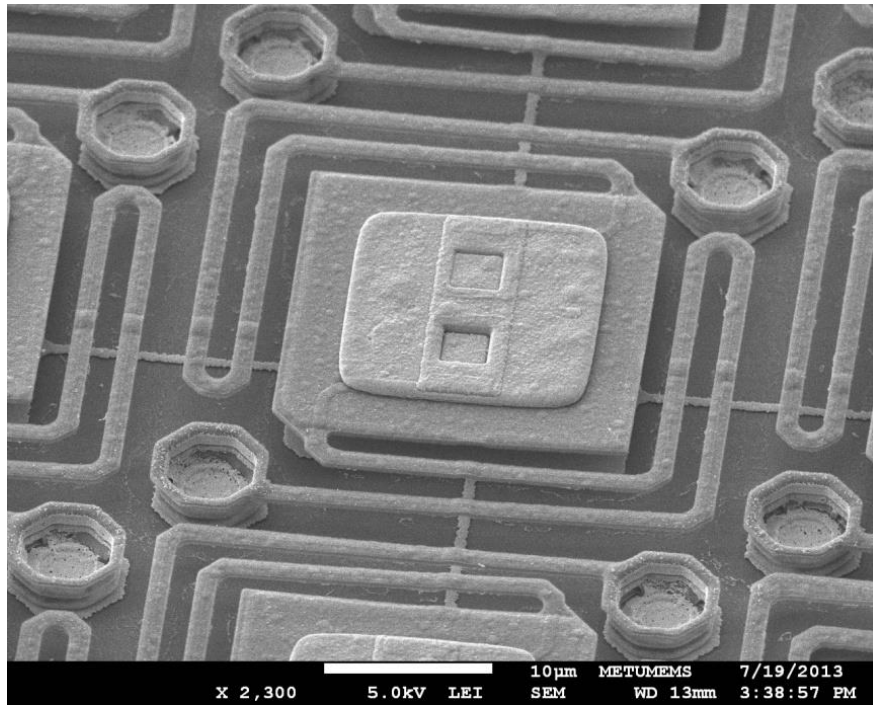
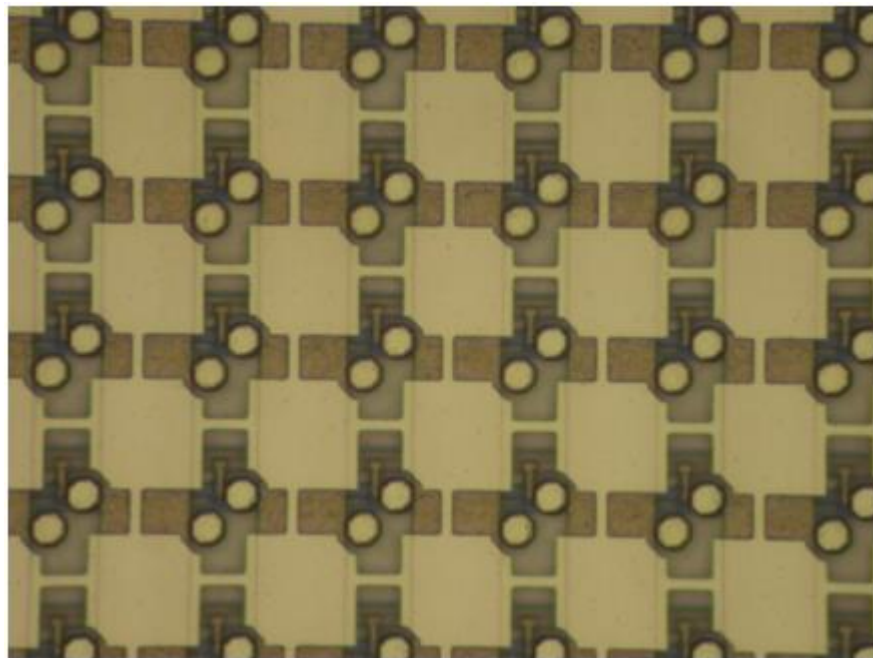
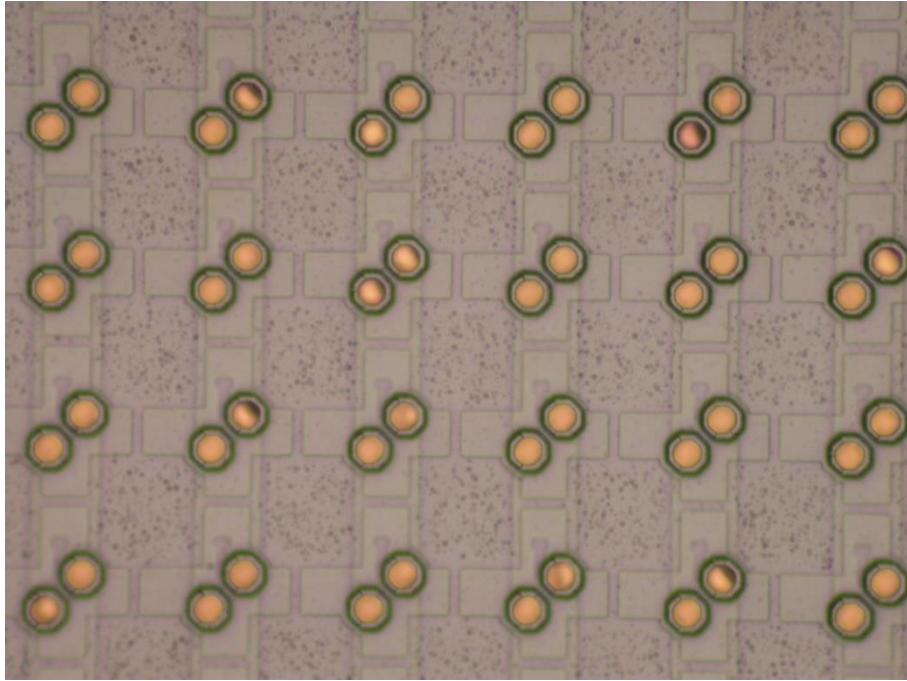


Figure 5.9. The SEM picture of successfully released full pixel bodies fabricated on a plain Si wafer in which a-Si was used as the sacrificial layer and then, etched with XeF_2 .

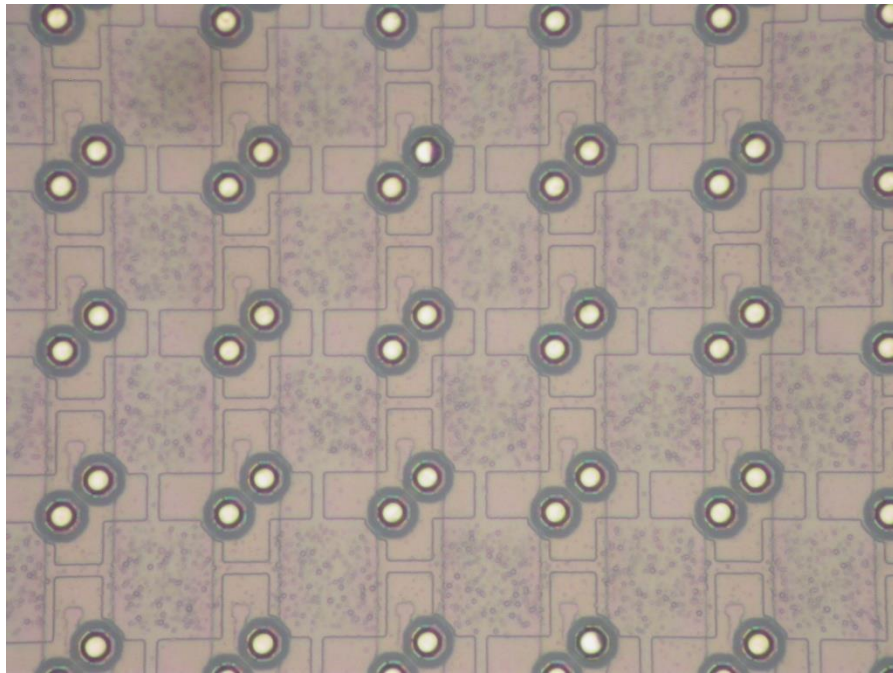


(a) The deposition and patterning of mirror layer which is gold

Figure 5.10. The microscope view of 384x288 microbolometer array fabricated on a 6" ROIC after the realization of each process step.

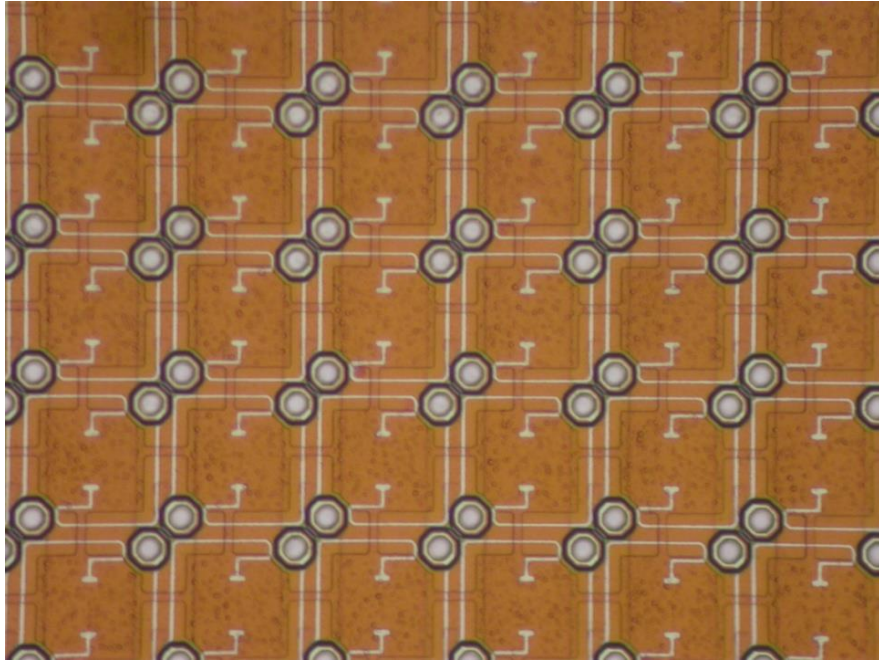


(b) The deposition and patterning of sacrificial layer which is a-Si

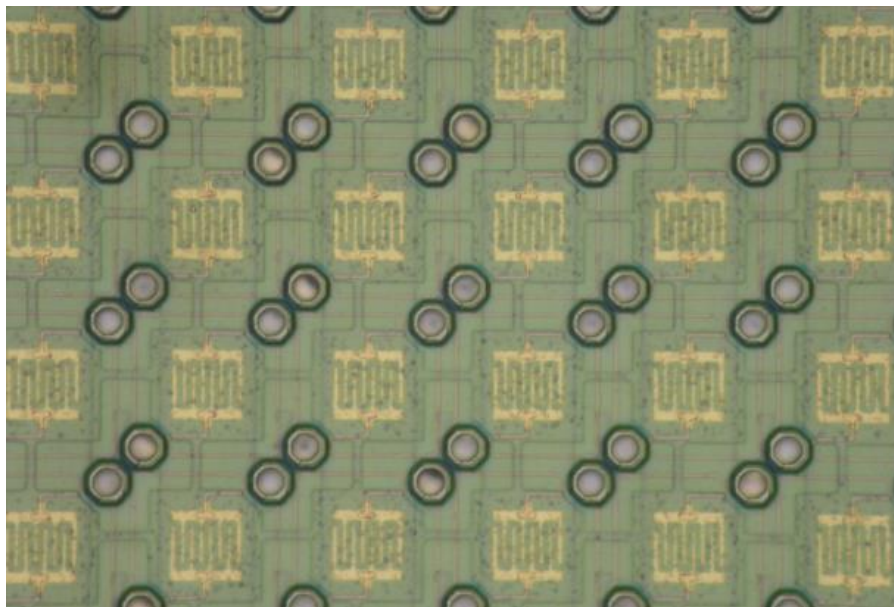


(c) The deposition and patterning of structural layer which is SiN_x

Figure 5.10 (cont'd). The microscope view of 384x288 microbolometer array fabricated on a 6" ROIC after the realization of each process step.

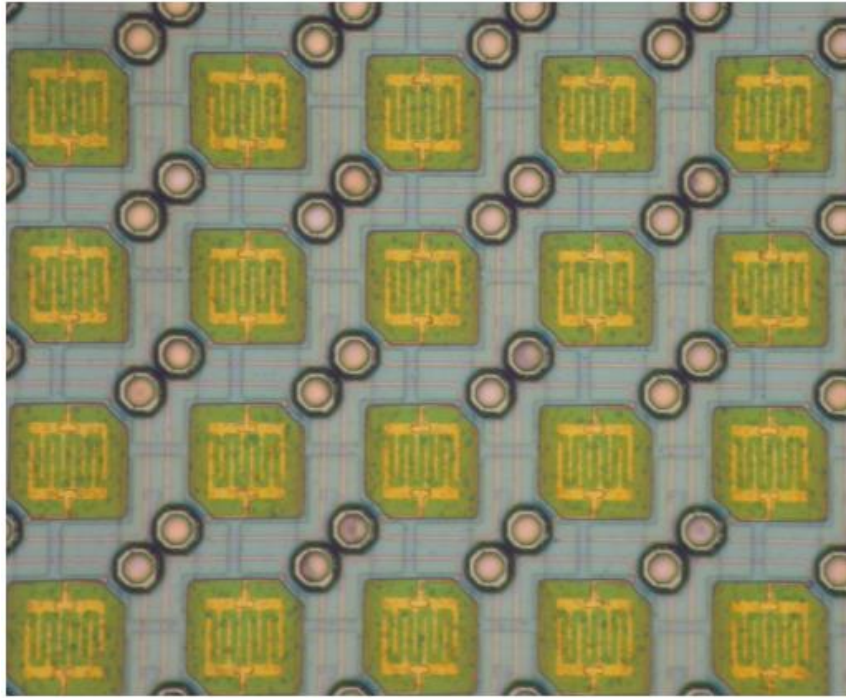


(d) The deposition and patterning of metal arms which are titanium

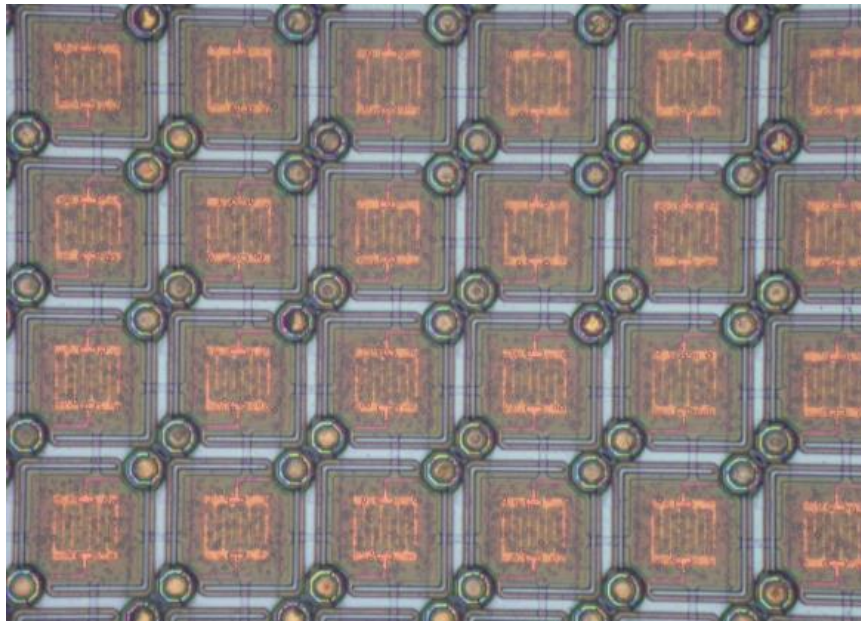


(e) The deposition and patterning of electrodes which are gold

Figure 5.10 (cont'd). The microscope view of 384x288 microbolometer array fabricated on a 6" ROIC after the realization of each process step.



(f) The deposition and patterning of VO_x layer



(g) The deposition of upper structural layer, SiN_x , deposition and patterning of absorber which is NiCr , and patterning of both bottom and upper SiN_x layers

Figure 5.10 (cont'd). The microscope view of 384x288 microbolometer array fabricated on a 6" ROIC after the realization of each process step.

After the pixel body was formed by etching both the upper and bottom SiN_x layers as shown in Figure 5.10g, the wafer was diced into dies. Figure 5.11 shows the photograph of whole wafer before dicing and pixel releasing. Note that, the photoresist is still remaining on the pixels in order to protect them during dicing. After the pixels are released, the photoresist is removed by O_2 plasma.

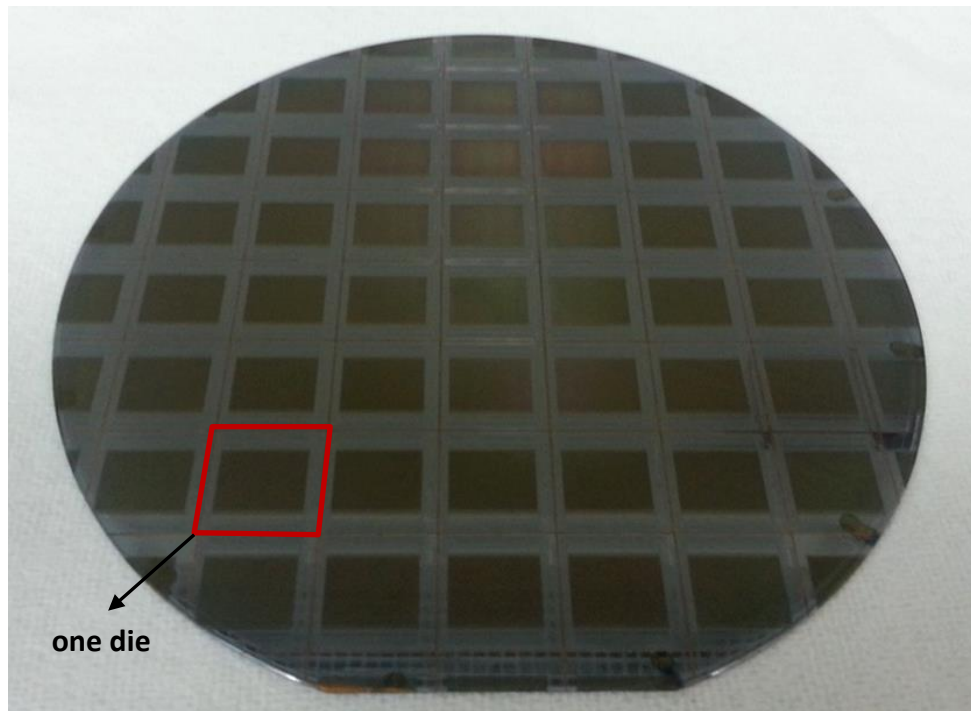


Figure 5.11. The photograph of whole 6" ROIC wafer on which the 384x288 microbolometer array was fabricated. The remaining steps are dicing, releasing the pixels, and stripping the photoresist.

The pixel releasing process is performed die level. After etching the sacrificial layer, a-Si, with XeF_2 , the array pixels were suspended successfully. Figure 6.12 and Figure 6.13 show the photograph of released array pixels under optical microscope and SEM, respectively. The establishment of required electrical set-up for measuring the performance parameters (resistance distribution, responsivity, and NETD) of the fabricated detectors and obtaining IR images is still continuing. Therefore, the performance tests will be left as the future work.

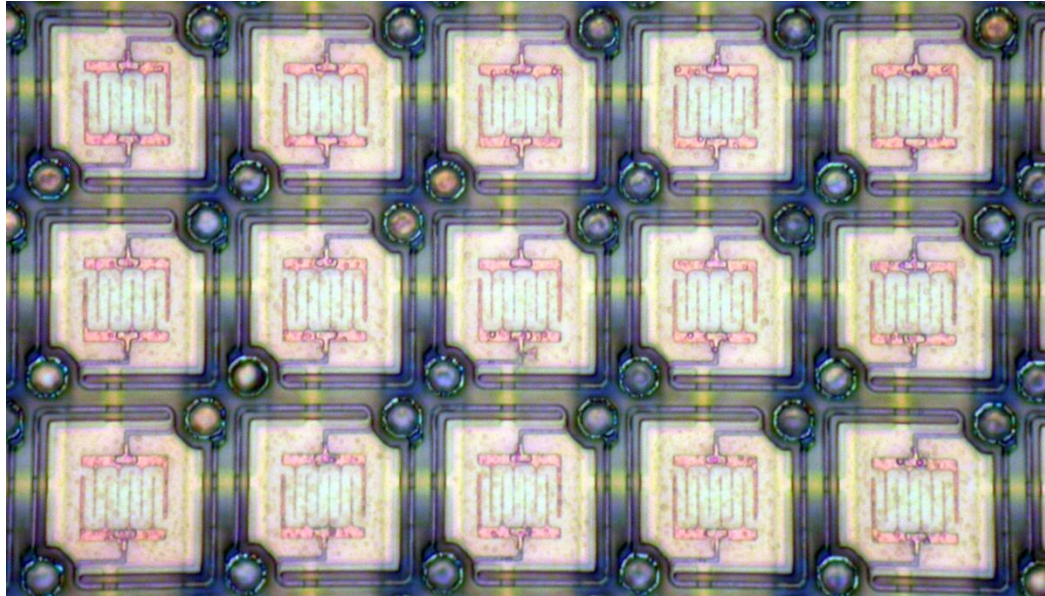


Figure 6.12. The optical image of fabricated 384x288 microbolometer array after releasing the pixels and stripping the photoresist.

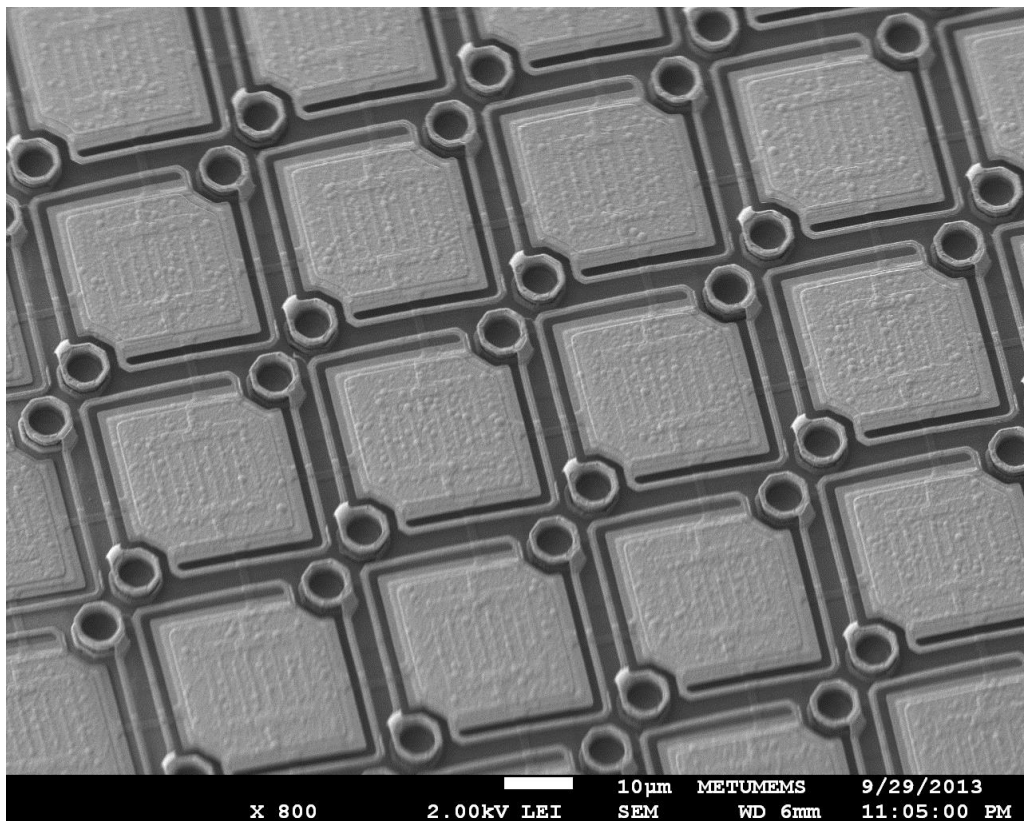


Figure 6.13. The SEM photograph of fabricated 384x288 microbolometer array after releasing the pixels and stripping the photoresist.

5.4. Conclusions

This chapter presented the fabrication of a 384x288 microbolometer array on a ROIC wafer having 35 μm pixels. Before fabricating the microbolometer array, the test resistors having the same type of electrodes with the array pixels were prepared in order to investigate resistance, TCR and 1/f noise performance of sol-gel deposited VO_x . The resistance was maintained around 60 k Ω by slightly diluting the coating liquid of VO_x thin films. The TCR at 25°C and $C_{1/f}$ parameter were measured as -1.9 %/°C and 6.3×10^{-10} , respectively. The fabrication of microbolometer array was started, however, it couldn't be continued due to the problem which arose in the sacrificial layer patterning step. That is, the titanium layer sputtered on the polyimide (PI) and used as a hard mask during PI patterning reacted with PI resulting in an unknown compound that couldn't be etched away on the anchor regions. This problem couldn't be solved and therefore, it was decided to switch PI with amorphous silicon (a-Si) as the sacrificial layer. The optimization studies for using the a-Si as the sacrificial layer were conducted and accomplished by METU MEMS Center staff. Afterwards, the fabrication of 384x288 microbolometer array in which the sol-gel deposited VO_x was used as the bolometric material was completed successfully by utilizing a-Si as the sacrificial layer. The establishment of required electrical set-up for measuring the performance parameters (resistance distribution, responsivity, and NETD) of the fabricated detectors and obtaining IR images from them is still continuing. Therefore, the performance tests will be left as the future work.

CHAPTER 6

CONCLUSIONS AND FUTURE WORK

The objective of this study is to develop a high performance bolometric material for microbolometers. For this purpose, vanadium oxide was chosen to be developed due to its high TCR, low $1/f$ noise parameter, ROIC compatible resistivity and processing temperature. Among various fabrication methods for vanadium oxide thin films, sol-gel deposition method was determined to be implemented due to its several advantages. The sol preparation route followed is dissolution of metallic vanadium powder in aqueous H_2O_2 .

The achievements and results of this thesis study are summarized below:

1. Several experimental runs were performed in order to optimize the dissolution step and dissolving V powder in 30 wt % H_2O_2 (aq) with a H_2O_2 to V molar ratio of 45 for 5-6 h was found to be the most appropriate procedure. The coating liquid was prepared by drying the sol formed after this dissolution step and ultrasonically remixing it with given amount of water.
2. Uniform coatings on Si/SiN_x substrates could be achieved by spinning this coating liquid which results in $V_2O_5 \cdot nH_2O$ ($n \leq 1.8$) thin films at first stage. DTA/TGA results and XRD patterns revealed that the hydrated form turns into orthorhombic V_2O_5 upon heat treatment at temperatures above 350°C.
3. Microresistors were fabricated by utilizing $V_2O_5 \cdot nH_2O$ phase due to the low resistivity of that phase. One of the main issues encountered during microresistor fabrication was the fact that the photolithography chemicals degraded VO_x . This problem was solved by passivating the VO_x thin film with a thin layer of SiN_x which is deposited by PECVD.
4. Another issue during microresistor fabrication was the etching of VO_x thin film. Wet etching with H_2O_2 (aq) was tried first, however, it later became problematic as the VO_x layer got thicker. Therefore, dry etching was tried and it was seen that RIE with a gas mixture CF_4 and O_2 was successful in etching VO_x . Optimization studies were also performed in order to manipulate VO_x/SiN_x selectivity and the RIE recipe was maintained more selective to VO_x than SiN_x by decreasing the plasma power from 225 W to 20 W.
5. Microresistors were successfully fabricated with $V_2O_5 \cdot nH_2O$ phase on 4" and 6" Si wafers and resistance values below 100 kΩ were achieved for the microresistors that can be fit into a 35 μm pixel pitch. The TCR was measured as ranging between -1.7 and -2.4 %/°C and the lowest $1/f$ noise parameter, $C_{1/f}$, maintained is 1.6×10^{-11} which are

comparable values with literature. This is the first time in literature that vanadium pentoxide gel (i.e. $V_2O_5 \cdot nH_2O$) phase is used as a bolometric material.

6. After microresistor fabrication, suspended single pixels having 35 μm pixel pitch were fabricated by using the developed sol-gel deposited VO_x as the IR active material. Its performance tests were conducted and thermal conductance, DC responsivity, thermal time constant, and absorptance were found as 3.37×10^{-8} W/K, 50,569 V/W, 20.9 ms, and 87 %, respectively. TCR was measured to be $-2.3 \text{ } \%/^{\circ}C$ at $25^{\circ}C$. Consistent noise results could not be obtained most probably due to the problematic electrical contacts.
7. Fabrication of a 384x288 microbolometer array on a ROIC wafer was started, however, it could not be continued due to a problem that arose during sacrificial layer (i.e. polyimide) patterning. That is, the titanium layer sputtered on the polyimide (PI) and used as a hard mask during PI patterning reacted with PI resulting in an unknown compound that couldn't be etched away on the anchor regions. This problem couldn't be solved and therefore, it was decided to use amorphous silicon (a-Si) instead of PI as the sacrificial layer. When a-Si is used, the pixels are released by dry etching a-Si with XeF_2 . The optimization studies of this process step, which are beyond the scope of this thesis study, were conducted and accomplished by METU MEMS Center staff. Afterwards, a 384x288 microbolometer array on a ROIC wafer, in which the developed sol-gel deposited VO_x was used as the active material, was fabricated successfully by utilizing a-Si as the sacrificial layer this time and the fabrication was completed successfully. The establishment of required electrical set-up for measuring the performance parameters (resistance distribution, responsivity, and NETD) of the fabricated detectors and obtaining IR images is still continuing.

Although enormous effort has been spent to accomplish the major objectives of this Ph. D. study, there are also additional items that need to and can be studied as the future work:

1. Above of all, the performance tests of fabricated microbolometer detectors (i.e. resistance distribution, responsivity, NETD measurement) should be conducted and images should be obtained after the required electrical set-up is established.
2. The noise measurement set-up should be improved for obtaining more accurate noise performance results of the bolometric material.
3. It is known that doping VO_x with metals like tungsten, molybdenum, etc. even in small amounts could change the electrical properties of VO_x . This study can be conducted for maintaining better performing bolometric materials.

REFERENCES

- [1] F. Niklaus, A. Decharat, C. Jansson, and G. Stemme, "Performance Model for Uncooled Infrared Bolometer Arrays and Performance Predictions of Bolometers Operating at Atmospheric Pressure," *Infrared Physics & Technology*, Vol. 51, Iss. 3, pp. 168-177, 2008.
- [2] M. Kohin and N. Butler, "Performance Limits of Uncooled VO_x Microbolometer Focal Plane Arrays," *Proceedings of SPIE*, Vol. 5406, Iss. PART 2, pp. 447-453, August 2004.
- [3] <http://www.theses.ulaval.ca/2005/23016/apb.html>, last reached on 31.07.2013.
- [4] <http://en.wikipedia.org/wiki/Infrared>, last reached on 31.07.2013.
- [5] G. J. Zissis, "Sources of Radiation," *The Infrared & Electro-Optical Systems Handbook Vol. 1* edited by J. S. Accetta, D. L. Shumaker, Vol. 1, Bellingham, Washington USA: SPIE Press, 1993.
- [6] M. Y. Tanrikulu, "An Uncooled Infrared Microbolometer Array Using Surface Micromachined MEMS Technology," *Dissertation for the Degree of Doctor of Philosophy*, Middle East Technical University, Department of Electrical and Electronics Engineering, 2007.
- [7] S. Eminoğlu, M. Y. Tanrikulu, and T. Akin, "Low-Cost 64x64 Uncooled Infrared Detector Arrays in Standard CMOS," *The 12th International Conference on Solid-State Sensors and Actuators (TRANSDUCERS'03)*, Vol. 1, pp. 316-319, June 2003.
- [8] S. Eminoglu, M. Y. Tanrikulu, and T. Akin, "A Low-Cost 128x128 Uncooled Infrared Detector Array in CMOS Process," *IEEE/ASME Journal of MicroElectroMechanical Systems*, Vol. 17, No. 1, pp. 20-30, February 2008.
- [9] M. Ueno, Y. Kosasamaya, T. Sugino, Y. Nakaki, Y. Fujii, H. Inoue, K. Kama, T. Seto, M. Takeda, and M. Kimata, "640x480 Pixel Uncooled Infrared FPA with SOI Diode Detectors," *Proceedings of SPIE*, Vol. 5783, Iss. PART II, Art. No. 63, pp. 566-577, March 2005.
- [10] T. Akin, "Chapter 10: CMOS-based Thermal Sensors" in *Advanced Micro & Nanosystems Volume 2: CMOS-MEMS* edited by H. Baltes, O. Brand, G. K. Fedder, C. Hierold, J. Kornivk, O. Tabata, Wiley-VCH, AMN-Flyer, 2005.
- [11] A. Rogalski, "Infrared Detectors for the Future," *Acta Physica Polonica A*, Vol. 116, No. 3, pp. 389-406, 2009.
- [12] D. F. Murphy, M. Ray, J. Wyles, J.F. Asbrock, C. Hewitt, R. Wyles, E. Gordon, T. Sessler, A. Kennedy, and S.T. Baur, "Performance Improvements for VO_x

- Microbolometer FPAs,” *Proceedings of SPIE*, Vol. 5406, Iss. Part 2, pp. 531-540, August 2004.
- [13] N. Oda, Y. Tanaka, T. Sasaki, A. Ajisawa, A. Kawahara, and S. Kurashina, “Performance of 320x240 Bolometer-Type Uncooled Infrared Detector,” *NEC Research & Development*, Vol. 44, pp. 170-174, 2003.
- [14] S. Tohyama, M. Miyoshi, S. Kurashina, N. Ito, T. Sasaki, A. Ajisawa, and N. Oda, “New Thermally Isolated Pixel Structure for High-Resolution Uncooled Infrared FPAs,” *Proceedings of SPIE*, Vol. 5406, Iss. PART 1, pp. 428-436, April 2004.
- [15] C. Li, G. D. Skidmore, C. Howard, C. J. Han, L. Wood, D. Peysha, E. Williams, C. Trujillo, J. Emmett, G. Robas, D. Jardine, C.-F. Wan, and E. Clarke, “Recent Development of Ultra Small Pixel Uncooled Focal Plane Arrays at DRS,” *Proceedings of SPIE*, Vol. 6542, Art. No. 65421Y, April 2007.
- [16] D. Murphy, M. Ray, J. Wyles, C. Hewitt, R. Wyles, E. Gordon, K. Almada, T. Sessler, S. Baur, and D. Van Lue, “640x512 17- μ m Microbolometer FPA and Sensor Development,” *Proceedings of SPIE*, Vol. 6542, Art. No. 65421Z, April 2007.
- [17] A. Rogalski, “Progress in Focal Plane Array Technologies,” *Progress in Quantum Electronics*, Vol. 36, pp. 342-473, 2012.
- [18] Ş. U. Şenveli, “Development of High Thermal Performance Uncooled Infrared Detectors Pixels with Enhanced Resistor Structures,” *Dissertation for the Degree of Master of Science*, Middle East Technical University, Department of Electrical and Electronics Engineering, 2010.
- [19] P. W. Kruse and D. D. Skatrud, “*Uncooled Infrared Imaging Arrays and Systems*,” *Semiconductor and Semimetals*, Vol. 47, Academic Press, 1997.
- [20] S. Eminoğlu, “Uncooled Infrared Focal Plane Arrays with Integrated Readout Circuitry Using MEMS and Standard CMOS Technologies,” *Dissertation for the Degree of Doctor of Philosophy*, Middle East Technical University, Department of Electrical and Electronics Engineering, 2003.
- [21] J. L. Tissot, S. Tinnes, A. Durand, C. Minassian, P. Robert, and M. Vilain, “High Performance Uncooled Amorphous Silicon VGA and XGA IRFPA with 17 μ m Pixel-Pitch,” *Proceedings of SPIE*, Vol. 7834, Art. No. 78340K, September 2010.
- [22] G. Vasilescu, “*Electronic Noise and Interfering Signals: Principles and Applications*,” Springer, Berlin, Germany, 2005.
- [23] F. Çivitçi, “Development of High Fill Factor Uncooled Infrared Detector Pixels,” *Dissertation for the Degree of Master of Science*, Middle East Technical University, Department of Electrical and Electronics Engineering, 2008.
- [24] M. Moreno, A. Kosarev, A. Torres, and R. Ambrosio, “Fabrication and Performance Comparison of Planar and Sandwich Structures of Microbolometers with Ge Thermo-Sensing Layer,” *Thin Solid Films*, Vol. 515, Iss. 19, pp. 7607-7610, 2007.
- [25] M. Moreno, A. Kosarev, A. Torres, and R. Ambrosio, “Comparison of Three Uncooled Micro-bolometers Configurations Based on Amorphous Silicon-Germanium

- Thin Films Deposited by Plasma,” *Journal of Non-Crystalline Solids*, Vol. 354, Iss. 19-25, pp. 2598-2602, 2008.
- [26] A. Ahmed and R. N. Tait, “Noise Behavior of Amorphous $\text{Ge}_x\text{Si}_{1-x}\text{O}_y$ for Microbolometer Applications”, *Infrared Physics & Technology*, Vol. 46, Iss. 6, pp. 468-472, 2005.
- [27] M. Nahum, Q. Hu, P. L. Richards, S. A. Sachtjen, N. Newman, and B. F. Cole, “Fabrication and Measurement of High Tc Superconducting Microbolometers,” *IEEE Transactions on Magnetics*, Vol. 27, Iss. 2, pp. 3081-3084, 1991.
- [28] K. Tsutsumi, A. Yamashita, and H. Ohji, “The Experimental Study of High TCR Pt Thin Films for Thermal Sensors,” *Proceedings of IEEE Sensors*, Vol.1, Iss. 2, pp. 1002-1005, June 2002.
- [29] H. K. Lee, J. B. Yoon, E. Yoon, S. B. Ju, Y. J. Yong, W. Lee, and S. G. Kim, “A High Fill-Factor Infrared Bolometer Using Micromachined Multilevel Electrothermal Structures,” *IEEE Transactions on Electron Devices*, Vol. 46, Iss. 7, pp. 1489-1491, 1999.
- [30] F. N. Hooge, T. G. M. Kleinpenning, and L. K. J. Vandamme, “Experimental Studies on $1/f$ Noise,” *Reports on Progress in Physics*, Vol. 44, pp. 479-532, 1981.
- [31] N. Chi-Anh, H.-J. Shin, K. Kim, Y.-H. Han, and S. Moon, “Characterization of Uncooled Bolometer with Vanadium Tungsten Oxide Infrared Active Layer,” *Sensors and Actuators A: Physical*, Vol. 123-124, pp. 87-91, 2005.
- [32] N. Chi-Anh and S. Moon, “Excess Noise in Vanadium Tungsten Oxide Bolometric Material,” *Infrared Physics and Technology*, Vol. 50, Iss. 1, pp. 38-41, 2007.
- [33] V. Y. Zerov, V. G. Malyarov, I. A. Khrebtov, Y. V. Kulikov, I. I. Shaganov, and A. D. Smirnov, “Uncooled Membrane-Type Linear Microbolometer Array Based on a VO_x Film,” *Journal of Optical Technology*, Vol. 68, Iss. 6, pp. 428-431, 2001.
- [34] M. A. Todd, P. P. Donohue, R. Watton, D. J. Williams, C. J. Anthony, and M. G. Blamire, “High Performance Ferroelectric and Magnetoresistive Materials for Next-Generation Thermal Detector Arrays,” *Proceedings of SPIE*, Vol. 4795, pp. 88-89, July 2002.
- [35] N. Fieldhouse, S. M. Pursel, R. Carey, and M. W. Horn, S. S. N. Bharadwaja, “Vanadium Oxide Thin Films for Bolometric Applications Deposited by Reactive Pulsed DC Sputtering,” *Journal of Vacuum Science & Technology A*, Vol. 27, Iss. 4, pp. 951-955, 2009.
- [36] H. K. Kang, Y. H. Han, H. J. Shin, S. Moon., and T.H. Kim “Enhanced Infrared Detection Characteristics of VO_x Films Prepared Using Alternating V_2O_5 and V Layers,” *Journal of Vacuum Science & Technology B*, Vol. 21, Iss. 3, pp. 1027-1031, 2003.
- [37] M. A. Demyanenko, B. I. Fomin, V. N. Ovsyuk, I. V. Marchishin, I. O. Parm, L. L. Vasil'ieva, and V. V. Shashkin, “Uncooled 160×120 Microbolometer IR FPA Based on Sol-Gel VO_x ,” *Proceedings of SPIE*, Vol. 5957, Art. No. 59571R, 2005.

- [38] V. G. Malyarov, I. A. Khrebtov, Yu. V. Kulikov, I. I. Shaganov, and V. Yu. Zerov, "Comparative Investigations of Bolometric Properties of Thin-Film Structures Based on Vanadium Dioxide and Amorphous Hydrated Silicon," *Proceedings of SPIE*, Vol. 3819, pp. 136-142, October 1999.
- [39] R. E. Johanson, M. Güneş and S. O. Kasap, "Noise in Hydrogenated Amorphous Silicon," *IEE Proceedings: Circuits, Devices and Systems*, Vol. 149, Iss. 1, pp. 68-74, 2002.
- [40] S. Li, Z. Wu, Y. Jiang, W. Li, N. Liao, and J. Yu "Noise in Boron Doped Amorphous/Microcrystallization Silicon Films," *Applied Surface Science*, Vol. 254, Iss. 11, pp. 3274-3276, 2008.
- [41] P. C. Shan, Z. Çelik-Butler, D. P. Butler, A. Janhanzeb, C. M. Travers, W. Kula, and R. Sobolewski, "Investigation of Semiconducting YBaCuO Thin Films: A New Room Temperature Bolometer," *Journal of Applied Physics*, Vol. 80, Iss. 12, pp. 7118-7123, 1996.
- [42] A. H. Z. Ahmed and R. N. Tait, "Characterization of Amorphous $\text{Ge}_x\text{Si}_{1-x}\text{O}_y$ for Micromachined Uncooled Bolometer Applications," *Journal of Applied Physics*, Vol. 94, Iss. 8, pp. 5326-5332, 2003.
- [43] M. M. Rana and D. P. Butler, "Amorphous $\text{Ge}_x\text{Si}_{1-x}\text{O}_y\text{:H}$ Microbolometers with High Responsivity," *Proceedings of IEEE Sensors*, Art. No. 4388450, pp. 519-522, October 2007.
- [44] M. M. Rana and D. P. Butler, "Noise Reduction of a- $\text{Si}_{1-x}\text{Ge}_x\text{O}_y$ Microbolometers by Forming Gas Passivation," *Thin Solid Films*, Vol. 516, Iss. 18, pp. 6499-6503, 2008.
- [45] M. Moreno, A. Kosarev, A. Torres, and I. Juarez, "Arrays of Uncooled Microbolometers Based on Amorphous Silicon-Germanium Thin Films Deposited by Plasma," *Journal of Non-Crystalline Solids*, Vol. 354, pp. 2552-2555, 2008.
- [46] L. Dong, R. Yue, and L. Liu, "An Uncooled Microbolometer Infrared Detector Based on Poly-SiGe Thermistor," *Sensors and Actuators A: Physical*, Vol. 105, Iss. 3, pp. 286-292, 2003.
- [47] S. Sedky, P. Fiorini, K. Baert, L. Hermans, and R. Mertens, "Characterization and Optimization of Infrared Poly SiGe Bolometers," *IEEE Transactions on Electron Devices*, Vol. 46, Iss. 4, pp. 675-682, 1999.
- [48] H. K. Lee, S. Y. Myong, K. S. Lim, and E. Yoon, "Electrical Properties of Photo-CVD Boron-Doped Hydrogenated (p-nc-SiCH) Films for Uncooled IR Bolometer Applications," *Journal of Non-Crystalline Solids*, Vol. 316, Iss. 2-3, pp. 297-301, 2003.
- [49] T. Ichihara and K. Aizawa, "1/f Noise in a- $\text{Si}_{1-x}\text{C}_x\text{:H}$ Thin Films as Novel Thermistor Materials for Micro-Machined IR Sensors," *Journal of Non-Crystalline Solids*, Vol. 227-230, Iss. PART 2, pp. 1345-1348, 1998.

- [50] F. Yang, L. Mechin, J. M. Routoure, B. Guillet, and R. A. Chakalov, "Low-Noise $\text{La}_{0.7}\text{Sr}_{0.3}\text{MnO}_3$ Thermometers for Uncooled Bolometric Applications," *Journal of Applied Physics*, Vol. 99, No. 024903, pp. 1-6, 2006.
- [51] A. Lisauskas, S. I. Khartsev, and A. M. Grishin, "Studies of 1/f Noise in $\text{La}_{1-x}\text{M}_x\text{MnO}_3$ (M = Sr, Pb) Epitaxial Thin Films," *Journal of Low Temperature Physics*, Vol. 117, No. 5/6, pp. 1647-1651, 1999.
- [52] J. H. Kim, S. I. Khartsev, and A. M. Grishin, "Epitaxial Colossal Magnetoresistive $\text{La}_{0.67}(\text{Sr,Ca})_{0.33}\text{MnO}_3$ Films on Si," *Applied Physics Letters*, Vol. 82, Iss. 24, pp. 4295-4297, 2003.
- [53] P. Metcalf, "Metal Insulator Transitions in Non-Stoichiometric, Chromium and Titanium Doped Vanadium Oxide Thin Films," *Dissertation for the Degree of Doctor of Philosophy*, Purdue University, 2007.
- [54] J. Nag and J. R. F. Haglund, "Synthesis of Vanadium Dioxide Thin Films and Nanoparticles," *Journal of Physics Condensed Matter*, Vol. 20, Iss. 26, pp. 1-14, 2008.
- [55] F. J. Morin, "Oxides Which Show a Metal-to-Insulator Transition at the Neel Temperature," *Physical Review Letters*, Vol. 3, Iss. 1, pp. 34-36, 1959.
- [56] Y. Lv, M. Hu, M. Wu, and Z. Liu, "Preparation of Vanadium Oxide Thin Films with High Temperature Coefficient of Resistance by Facing Targets D.C. Reactive Sputtering and Annealing Process," *Surface and Coatings Technology*, Vol. 201, Iss. 9-11, pp. 4969-4972, 2007.
- [57] K. R. Speck, "Sol-Gel Growth of Vanadium Dioxide," *Dissertation for the Degree of Doctor of Philosophy*, The Johns Hopkins University, 1990.
- [58] G. Guzman, F. Beteille, R. Morineau, and J. Livage, "Electrical Switching in VO_2 Sol-Gel Films," *Journal of Material Chemistry*, Vol. 6, Iss. 3, pp. 505-506, 1996.
- [59] G. V. Jorgenson and J. C. Lee, "Doped Vanadium Oxide for Optical Switching Films," *Solar Energy Materials*, Vol. 14, Iss. 3-5, pp. 205-214, 1986.
- [60] Y. Wang and G. Cao, "Synthesis and Enhanced Intercalation Properties of Nanostructured Vanadium Oxides," *Chemistry of Materials*, Vol. 18, Iss. 12, pp. 2787-2804, 2006.
- [61] M. B. Sahana, C. Sudakar, C. Thapa, G. Lawes, V. M. Naik, R. J. Baird, G. W. Auner, R. Naik, and K. R. Padmanabhan, "Electrochemical Properties of V_2O_5 Thin Films Deposited by Spin Coating," *Materials Science and Engineering B: Solid-State Materials for Advanced Technology*, Vol. 143, Iss. 1-2, pp. 42-50, 2007.
- [62] J. Livage, "Vanadium Pentoxide Gels," *Chemistry of Materials*, Vol. 3, Iss. 4, pp. 578-593, 1991.
- [63] A. C. Pierre, "Introduction to Sol-Gel Processing," Kluwer Academic Publishers, USA, 2002.

- [64] T. Kudo and M. Hibino, "Lithium Intercalation into Coated Thin Films of a New 2-Dimensional Vanadium Oxide," *Thin Film Solid Ionic Devices and Materials*, Vol. 95, pp. 31-45, 1995.
- [65] M. Hibino, M. Ugaji, A. Kishimoto, and T. Kudo, "Preparation and Lithium Intercalation of a New Vanadium Oxide with a Two-Dimensional Structure," *Solid State Ionics*, Vol. 79, Iss. C, pp. 239-244, 1995.
- [66] Y. M. Li and T. Kudo, "Properties of Mixed-Oxide MoO₃/V₂O₅ Electrochromic Films Coated from Peroxo-olymolybdovanadate Solutions," *Solar Energy Materials and Solar Cells*, Vol. 39, Iss. 2-4, pp. 179-190, 1995.
- [67] A. A. Bahgata, F. A. Ibrahim, and M. M. El-Desoky, "Electrical and Optical Properties of Highly Oriented Nanocrystalline Vanadium Pentoxide," *Thin Solid Films*, Vol. 489, Iss. 1-2, pp. 68-73, 2005.
- [68] D.R. Lide, "*Handbook of Chemistry and Physics*," 86th ed., CRC Press
- [69] W.F. Linke, "*Solubilities of Inorganic and Metal-Organic Compounds K-Z*," Vol. 11, 4th ed., American Chemical Society, Washington, D.C.
- [70] A. Cheremisin, V. Putrolaynen, A. Velichko et al. "UV Laser Modification and Selective Ion-Beam Etching of Amorphous Vanadium Pentoxide Thin Films," *Physica Status Solid (A) Applications and Materials Science*, Vol. 206, Iss. 7, pp. 1484-1487, 2009.
- [71] Y. H. Han, K. T. Kim, N. Chi-Anh et al., "Fabrication and Characterization of Bolometric Oxide Thin Film Based on Vanadium-Tungsten Alloy," *Sensors and Actuators A: Physical*, Vol. 123-124, pp. 660-664, 2005.
- [72] M. Tepegöz, "A Monolithic Readout Circuit for Large Format Uncooled Infrared Detector Focal Plane Arrays," *Dissertation for the Degree of Doctor of Philosophy*, Middle East Technical University, Department of Electrical and Electronics Engineering, 2010.
- [73] M. Avram, A. Avram, F. Comanescu, A. M. Popescu, and C. Voitincu, "Reactive Ion Etching for Patterning High Aspect Ratio and Nanoscale Features," *Proceedings of the International Semiconductor Conference*, Vol. 1, pp. 253-256, October 2009.
- [74] A. Toprak, "CMOS Readout Electronics for Microbolometer Type Infrared Detector Arrays," *Dissertation for the Degree of Master of Science*, Middle East Technical University, Department of Electrical and Electronics Engineering, 2009.
- [75] F. S. Ohuchi and S. C. Freilich, "Metal Polyimide Interface: A Titanium Reaction Mechanism," *Journal of Vacuum Science & Technology A*, Vol. 4, No. 3, pp. 1039-1045, 1986.
- [76] J. D. Parsons, G. B. Kruaval, and A. K. Chaddha, "Low Specific Resistance ($<6 \times 10^{-6} \Omega \cdot \text{cm}^2$) TiC Ohmic Contacts to n-Type β -SiC," *Applied Physics Letters*, Vol. 65, No. 16, pp. 2075-2077, 1994.

APPENDIX A

DETAILS OF SUSPENDED SINGLE PIXEL FABRICATION STEPS

1.	<p>Mirror Layer Formation</p> <ol style="list-style-type: none"> a. Sputtering 20 nm Ti/80 nm Au b. Photolithography c. Etching Au in aqua regia ($\text{HNO}_3:\text{HCl}:\text{H}_2\text{O} = 1:2:5$) d. Etching Ti in $\text{H}_2\text{O}_2:\text{HF}:\text{H}_2\text{O} = 1:1:400$ e. Stripping photoresist (PR)
2.	<p>Sacrificial Layer Deposition and Patterning</p> <ol style="list-style-type: none"> a. Spin coating polyimide (PI) and curing at 300°C b. Sputtering 20 nm Ti for masking PI during RIE c. Photolithography d. Etching Ti in $\text{H}_2\text{O}_2:\text{HF}:\text{H}_2\text{O} = 1:1:400$ e. Etching PI by RIE f. Stripping PR g. Stripping Ti in $\text{H}_2\text{O}_2:\text{HF}:\text{H}_2\text{O} = 1:1:400$
3.	<p>Structural Layer Deposition and Patterning</p> <ol style="list-style-type: none"> a. Depositing 0.2 μm SiN_x by PECVD b. Photolithography c. Etching SiN_x by RIE d. Stripping PR
4.	<p>Metal Arm Formation</p> <ol style="list-style-type: none"> a. Sputtering 50 nm Ti b. Photolithography c. Etching Ti in $\text{NH}_3(\text{aq}):\text{H}_2\text{O}_2 = 1:8$ d. Stripping PR
5.	<p>Electrode Formation</p> <ol style="list-style-type: none"> a. Sputtering 20 nm Cr/50 nm Au b. Photolithography c. Etching Au in aqua regia ($\text{HNO}_3:\text{HCl}:\text{H}_2\text{O} = 1:2:5$) d. Etching Cr in a commercial etchant e. Stripping photoresist
6.	<p>VO_x Deposition and Patterning</p> <ol style="list-style-type: none"> a. Sol preparation and aging it for 24 h b. Depositing VO_x by spin coating the prepared sol c. Annealing at 250°C for 20 min d. Depositing 0.1 μm SiN_x by PECVD for VO_x passivation e. Photolithography f. Etching SiN_x by RIE g. Etching VO_x by RIE h. Stripping PR

7.	Structural Layer Deposition a. Depositing 0.2 μm SiN_x by PECVD
8.	Absorber Layer Deposition and Patterning a. Sputtering 10 nm NiCr b. Photolithography c. Etching NiCr by inverse sputtering d. Stripping PR
9.	Structural Layer Patterning a. Photolithography b. Etching SiN_x by RIE
10.	Dicing The Wafer Into Dies
11.	Suspension of Pixels a. Suspending the pixels by etching PI in O_2 plasma

APPENDIX B

DETAILS OF 384x288 MICROBOLOMETER ARRAY FABRICATION STEPS

1.	Mirror Layer Formation <ol style="list-style-type: none"> a. Sputtering 20 nm Ti/80 nm Au b. Photolithography c. Etching Au in aqua regia (HNO₃:HCl:H₂O = 1:2:5) d. Etching Ti in H₂O₂:HF:H₂O = 1:1:400 e. Stripping photoresist (PR)
2.	Sacrificial Layer Deposition and Patterning <ol style="list-style-type: none"> a. Deposition of 2 μm a-Si by PECVD b. Photolithography c. Opening of contact regions in a-Si by DRIE d. Stripping PR e. BHF treatment for removing SiO₂
3.	Structural Layer Deposition and Patterning <ol style="list-style-type: none"> a. Depositing 0.2 μm SiN_x by PECVD b. Photolithography c. Etching SiN_x by RIE d. Stripping PR
4.	Metal Arm Formation <ol style="list-style-type: none"> a. Sputtering 50 nm Ti b. Photolithography c. Etching Ti in NH₃ (aq):H₂O₂ = 1:8 d. Stripping PR
5.	Electrode Formation <ol style="list-style-type: none"> a. Sputtering 20 nm Cr/50 nm Au b. Photolithography c. Etching Au in aqua regia (HNO₃:HCl:H₂O = 1:2:5) d. Etching Cr in a commercial etchant e. Stripping photoresist
6.	VO_x Deposition and Patterning <ol style="list-style-type: none"> a. Sol preparation and aging it for 24 h b. Depositing VO_x by spin coating the prepared sol c. Annealing at 250°C for 20 min d. Depositing 0.1 μm SiN_x by PECVD for VO_x passivation e. Photolithography f. Etching SiN_x by RIE g. Etching VO_x by RIE h. Stripping PR
7.	Structural Layer Deposition <ol style="list-style-type: none"> a. Depositing 0.2 μm SiN_x by PECVD

8.	Absorber Layer Deposition and Patterning
	<ul style="list-style-type: none"> a. Sputtering 10 nm NiCr b. Photolithography c. Etching NiCr by inverse sputtering d. Stripping PR
9.	Structural Layer Patterning
	<ul style="list-style-type: none"> c. Photolithography d. Etching SiN_x by RIE
10.	Dicing The Wafer Into Dies
11.	Suspension of Pixels
	<ul style="list-style-type: none"> a. Suspending the pixels by etching a-Si with XeF₂
12.	Stripping PR in O₂ plasma

CURRICULUM VITAE

PERSONAL INFORMATION

Surname, Name : Dervişoğlu, Özgecan
Nationality : Turkish (TC)
Date and Place of Birth: 9 February 2013, Ordu
Phone : +90 532 700 59 41
Email : ozgecan_dervisoglu@yahoo.com

EDUCATION

2007 - Ph.D., Micro and Nanotechnology Graduate Program, METU
2004 – 2007 M.Sc., Department of Chemical Engineering, METU
2000 – 2004 B.Sc., Department of Chemical Engineering, METU
1999 – 2000 School of Foreign Languages (English), METU
1996 – 1999 Özel Arı Fen Lisesi

WORK EXPERIENCE

Dec 2006 – Apr 2008 TÜBİTAK - Basic Sciences Research Group, Scientific Programs
Assistant Expert
Summer 2003 Kayaş Kapsül Fabrikası, Intern Engineering Student
Summer 2002 Ankara Şeker Fabrikası, Intern Engineering Student

FOREIGN LANGUAGES

Advanced English

PUBLICATIONS

1. Ö. Dervişoğlu Ö., I. Aşar I., İ. Eroğlu, C. Özgen, G. Ö. Çakal, “Inferential Control of Boric Acid Production System,” *Proceedings of 3rd International Boron Symposium*, pp.245-252, 2006.
2. Ö. Dervişoğlu, I. Aşar, G. Çakal, İ. Eroğlu, C. Özgen, “Borik Asit Üretim Sisteminin Algısal Yöntem ile Denetlenmesi,” *UKMK 8*, pp. 300-305, 2008

HOBBIES

trekking, movies, biography books, astronomy and space sciences